AN EXPLORATION OF POTENTIAL PATHWAYS TOWARD EMERGING ELECTRONIC DEVICES WITH FERROELECTRIC MATERIALS

A Dissertation
Presented to
The Academic Faculty

By

Chia-Sheng Hsu

In Partial Fulfillment
of the Requirements for the Degree
Doctor of Philosophy in the
School of Electrical and Computer Engineering

Georgia Institute of Technology

December 2021

AN EXPLORATION OF POTENTIAL PATHWAYS TOWARD EMERGING ELECTRONIC DEVICES WITH FERROELECTRIC MATERIALS

Approved by:

Dr. Azad Naeemi, Advisor
School of Electrical and Computer Engineering
Georgia Institute of Technology

Dr. Jeffrey Davis
School of Electrical and Computer Engineering
Georgia Institute of Technology

Dr. Zhigang Jiang
School of Physics
Georgia Institute of Technology

Dr. Shimeng Yu
School of Electrical and Computer Engineering
Georgia Institute of Technology

Dr. Asif Khan
School of Electrical and Computer Engineering
Georgia Institute of Technology

Date Approved: October 7, 2021

The pain passes, but the beauty remains.

Pierre-Auguste Renoir

Dedicated to the future. May it be brighter than today.

ACKNOWLEDGEMENTS

First of all, I would like to thank my caring advisor Professor Azad Naeemi for giving me such a precious research opportunity in my field of interest and for guiding me academically and spiritually along this PhD training journey toward a professional career path. It is an honor and a pleasure to be part of Prof. Naeemi's group as large research degree of freedom, open-mindedness, eagerness to learn and optimism are well combined to nurture novel ideas, however small they are. From my perspective, all the invaluable lessons I learned from him in both professional work and personal life will be memorable.

I would like to express my sincere gratitude to Dr. Sou-Chi Chang, Dr. Dmitri Nikonov together with Dr. Ian Young. With considerable experience of research, their team at *Intel* has always provided insightful discussions and constructive feedback on the important details and formidable obstacles in my research, which brings our teamwork into many fruitful results.

I would also like to acknowledge Prof. Jeffrey Davis from School of Electrical and Computer Engineering and Prof. Zhigang Jiang from School of Physics for continuing being my committee members as I believe their expertise and professional experiences can further improve and complement my research works. Special thanks are given to Profs. Asif Khan and Shimeng Yu from School of Electrical and Computer Engineering for serving on my defense committee with their expertise and outstanding contributions in my research area.

With all the kind technical helps, discussions and life experiences during these past years, my PhD journey was further brightened up thanks to all the current and former group members, Dr. Sou-Chi Chang, Prof. Chenyun Pan, Prof. Sourav Dutta, Prof. Nickvash Kani, Dr. Rouhollah Mousavi, Dr. Ramy Nashed, Dr. Divya Prasad, Victor Huang, Dr. Yu-Ching Liao, Mohammad Adnaan, Piyush Kumar, Samantha Lubaba Noor, and Siri Narla.

I'm also grateful to Dr. Tien-Ming Chuang at Institute of Physics, Academia Sinica, Profs. Shang-Da Yang, Chung-Chin Lu, and Yi-Wen Liu at Department of Electrical Engineering, National Tsing Hua University for their teaching and guidance at the early stage in my research career.

My deepest gratitude goes to my dear family, my father, my mother, my brother and late grandfather and grandmother, for their unconditional love and supports from my home country Taiwan even if I could not keep them company very often during these years. Last but not least, I would leave the rest of the credit to myself for devoting efforts to the investigation and development of emerging devices and the contribution to the research community with the courage to go through each daunting grind. I really appreciate all the ups and downs I faced along the way. Without them, the important research contributions could not be made, and this thesis would not be completed.

Moreover, thanks to all the funding agencies, the research works are financially supported by Semiconductor Research Corporation (SRC) NRI under Grant 2664.001, National Science Foundation ECCS-CAREER under Grant 1254315, and Intel Corporation through SRC MSR-INTEL TASK 2835.001.

TABLE OF CONTENTS

LIST OF TABLES

LIST OF FIGURES

CHAPTER 1
INTRODUCTION

1.1 CMOS Transistor Scaling

Over the past decades, the modern society has gradually evolved into a global village, in which people are more interconnected thanks to the rapid propagation of information via the Internet. In addition, smart electronic devices, such as smart phones and tablets, become ubiquitous these days. Such information revolution can be attributed to the dramatic improvement on computing performance and storage capacities in hardware devices. As a consequence, the realization of machine learning and artificial intelligence has been made possible. Moreover, with a huge amount of data being processed on a daily basis, cloud services, remote servers and workstations are also gaining in popularity.

None of these technological advances could have happened without the silicon-based technologies, especially the metal-oxide-semiconductor field-effect transistor (MOSFET) as the building block (Fig. 1.1(a)) responsible for computing power (logics) and mass storage (memories). As a result, the accelerating demand for computing power and storage capacity in microchips has made the semiconductor industry undergo a revolutionary growth in consumer markets. The trend in constant miniaturization of CMOS (complementary metal oxide semiconductor) transistors dates back to 1965, when an observation by Gordon Moore predicted that "*the number of electronic components per integrated circuit would double every year for the following ten years*" [1]. Ten years later, the forecast for the time period in which the number of components per chip would double was revised to "every two years" [2]. Since the proposal, Moore's Law has gradually become a guiding principle and continues to revolutionize the semiconductor industry for over a half century [3]. With such phenomenal scaling, the exponential increase in

the computing power of microchips has enabled more and more innovative devices and applications that are quipped with faster circuits with not only lower power dissipation but also a reduction in the cost. Nowadays, the transistor density per unit area in a microprocessor is a thousand times more compared to what was possible 20 years ago [4], as shown in Fig. 1.1(b). For example, a density of several hundred million transistors per square millimeter can be achieved with the state-of-the-art 5-nanometer lithography process [5]. While the Moore's trend is expected to continue for the next 10 years, the fabrication process has been confronted with technological limits when the transistor size is scaled down to the nanometer regime, and therefore, active research in the field of the beyond-CMOS technology is underway in pursuit of low-power logic and non-volatile memory devices.

In the early decades of scaling, the area occupied by a CMOS transistor on microchips was reduced by half in each new technology generation for device performance improvement without significantly sacrificing the fabrication cost (and thus product prices). As the lateral dimension of the device was scaled down by a factor of 0.7 in each technology node, the device performance benefits from the corresponding adjustments to the channel length ($0.7 \times L_{\text{gate}}$), the oxide thickness ($0.7 \times T_{\text{ox}}$), the supply voltage ($0.7 \times V_{\text{DD}}$), and the doping concentration ($N_{\text{d}}/0.7$) [6]. However, in recent years, further CMOS transistor miniaturization has become limited by physical, power, and technological challenges as the transistor size shrinks to the nanometer regime [7].

1.1.1 Physical limits

Historically, the process node driven by Moore's law was named after the physical gate length of a transistor [9]. However, as the channel length shrinks, various short-channel effects (SCE) start to degrade the performance of transistors. In particular, the prominent phenomenon known as drain-induced barrier lowing (DIBL) could significantly reduce the performance and reliability of transistors. As a three-terminal

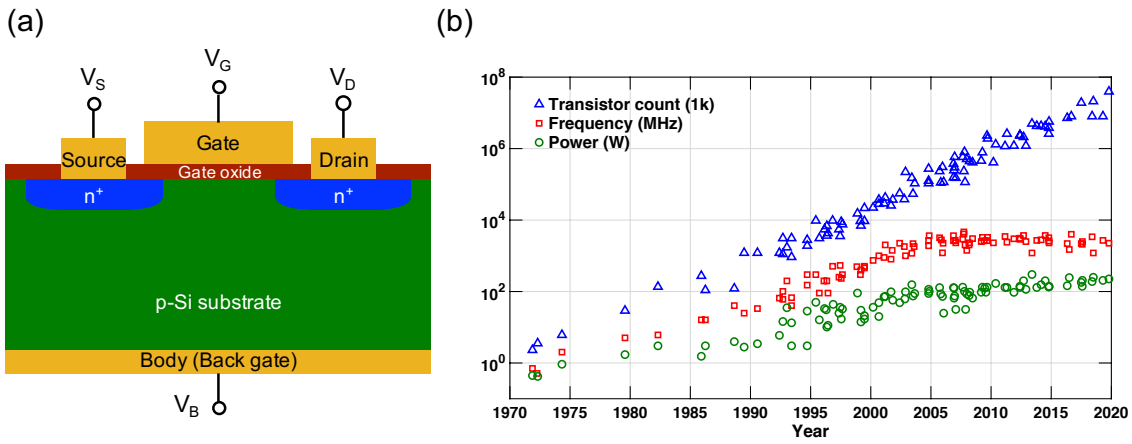

Figure 1.1: (a) The schematic of a conventional planar n-type MOSFET (NMOS), the building block and foundation of today's cutting-edge technologies. (b) Transistor counts for microprocessors under Moore's law and the corresponding frequency and power evolution in the past decades, adapted from the raw data in [4] (courtesy of [8]).

switch, the gate of a CMOS transistor controls the energy barrier between the drain and the source. When a gate voltage is applied to turn on the transistor, the barrier height is reduced through the electrostatic field and most of electrons can be injected thermionically from the source to the drain, leading to the current through the channel. On the other hand, when a device is off, the barrier height is so large that very few electrons can cross the barrier, and thus there is almost no current flow. However, in short-channel devices, as the channel of a CMOS transistor is reduced for a higher switching speed, the energy barrier may be further reduced by the voltage across the drain and the source, which potentially causes the current flow even if the transistor is intended to be off. The DIBL effect in short channel transistors is illustrated in Fig. 1.2. The direct consequence of DIBL is the decrease of the threshold voltage and thus the increase of subthreshold leakage currents.

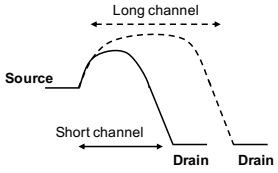

Figure 1.2: The illustration of the DIBL mechanism.

DIBL can be alleviated by increasing the channel doping concentration, which is also scaled down with the transistor size [6]. However, in heavily doped channels, side

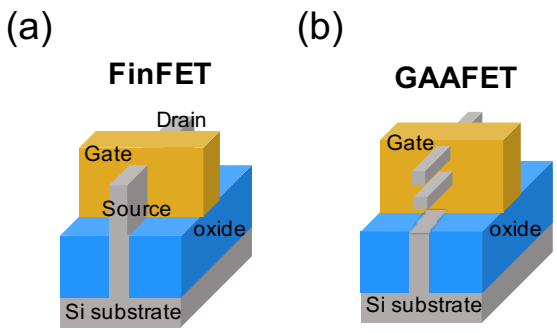

Figure 1.3: (a) Schematic FinFET device structure. (b) Schematic GAAFET device structure.

effects such as carrier mobility degradation due to surface scattering and gate-induced drain leakage (GIDL) due to band-to-band tunneling through the overlap region of the gate and the drain will have a negative impact on the performance and reliability of the CMOS device [10–12].

Furthermore, to enhance the driving current of a transistor, the gate capacitance is increased by reducing the gate oxide thickness. However, as the thickness of the SiO_2 layer gets thinner and thinner (below $\sim 2\,\mathrm{nm}$), higher leakage arises through the transistor gate due to direct quantum-mechanical tunneling. Therefore, high-κ dielectric materials, such as hafnium oxide and more recently aluminum oxide, were introduced to replace the SiO_2 oxide to maintain a large gate capacitance without increasing the gate leakage current. In addition, three-dimensional non-planar structures such as FinFETs [13] and gate-all-around FETs (GAAFETs) [14–16] with an enlarged surface area of the gate were proposed due to better electrical control of the transistor channel to mitigate the leakage current and other SCE in conventional planar MOS transistor structures, as shown in Fig. 1.3.

Nowadays, the channel length, shrunk to tens of nanometers, has approached the fundamental physical limit below which the performance would not benefit from further downscaling. Therefore, aiming to increase the transistor density by reducing the contacted metal pitch in the circuit layout instead, the state-of-the-art CMOS technology nodes no longer match any physical lengths.

1.1.2 Power limits

In integrated circuits (ICs), the power dissipation comes from both dynamic (active or switching) power dissipation and static (leakage) power dissipation [17, 18]. The former is the power required to switch the devices, while the latter results from leakage currents of the non-switching devices. With the clock frequency f, the dynamic power can be estimated as $C_{\mathrm{L}}V_{\mathrm{DD}}^2\alpha f$, where C_{L} is the effective load, V_{DD} is the supply voltage, and α, called the activity factor, is the fraction of the devices switching in each clock cycle [18]. Therefore, as V_{DD} decreases in each technology generation, f could be increased, roughly inversely proportional to the gate length, without significantly increasing the overall power consumption [6, 18]. However, the supply voltage in the scaling roadmap had gradually come to a stop at around $1\,\mathrm{V}$ as the gate length approaches about $30\,\mathrm{nm}$ in the recent technology generations [18, 19]. As a result, the operating clock frequency stopped increasing and almost remained constant at around $3.5\,\mathrm{GHz}$ to prevent the dynamic power density from increasing drastically [19]. Moreover, the threshold voltage V_{th} has to be scaled down to ensure a large enough ON current [6]. Figure 1.4(a) shows V_{DD} and V_{th} scaling down with the transistor gate length. The consequence of the decreasing threshold voltage is the increasing subthreshold leakage current, which leads to the increase of the static power density, as shown in Fig. 1.4(b). Figure. 1.4 also shows that as the device dimension is reduced below a certain size, the static power will eventually surpass the dynamic one, which means a microchip will dissipate a significant amount of energy even in the stand-by mode.

Despite all the efforts to reduce the power consumption, there still exists a fundamental limit of the switching power for CMOS transistors. Quantitatively, the subthreshold swing S in the unit of $\mathrm{V/decade}$ is the gate voltage required to increase the drain-source current I ten-fold in the subthreshold region,

$$S \coloneqq \frac{\partial V_{\mathrm{g}}}{\partial \log_{10} I} = \frac{\partial V_{\mathrm{g}}}{\partial \phi_{\mathrm{s}}} \frac{\partial \phi_{\mathrm{s}}}{\partial \log_{10} I}, \tag{1.1}$$

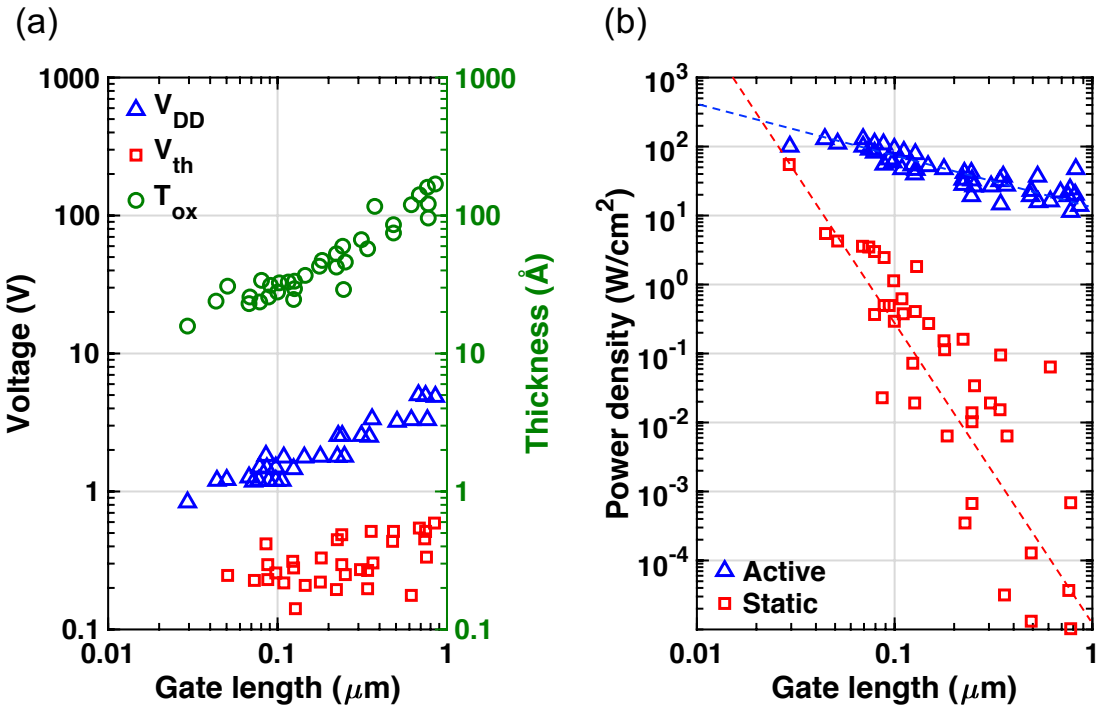

Figure 1.4: (a) V_{DD} and V_{th} scaling down with the transistor gate length. The reduced gate oxide thickness T_{ox} is also shown. (b) The increase of dynamic and static power density with the reduced device dimension, adapted from [18].

where V_g is the applied gate voltage and ϕ_{s} is the internal surface potential [20]. The schematic circuit diagram is shown in Fig. 1.5(a). From the capacitive voltage divider, the body factor m is given by

$$m = \frac{\partial V_{\mathrm{g}}}{\partial \phi_{\mathrm{s}}} = 1 + \frac{C_{\mathrm{s}}}{C_{\mathrm{ox}}}, \tag{1.2}$$

where C_{s} is the channel capacitance and C_{ox} is the gate oxide capacitance. In the subthreshold region, the drain current $I_D \propto \exp\left(\frac{q\phi_{\mathrm{s}}}{k_{\mathrm{B}}T}\right)$ at temperature T, where k_{B} is the Boltzmann constant and q is the elementary charge. The subthreshold swing can be calculated accordingly,

$$S = \frac{\partial V_{\mathrm{g}}}{\partial \log_{10} I} = m \frac{\partial \phi_{\mathrm{s}}}{\partial \log_{10} I} = m \frac{k_{\mathrm{B}}T}{q} \ln 10. \tag{1.3}$$

Thus, at room temperature (RT), $S \geq 60\,\mathrm{mV/decade}$ for conventional insulators ($m \geq 1$). Such a switching power limit of transistors is called the "Boltzmann Tyranny".

1.1.3 Fabrication limits

Besides the device structure limitations, the critical dimension (CD) of the lithography process in typical CMOS fabrication also poses difficulty to the device feature dimension. CD, the finest possible resolution of a lithography system, can be roughly estimated by the Rayleigh criterion given as

$$CD = k_1 \frac{\lambda}{NA}, \tag{1.4}$$

where k_1 (with a physical limit of k_1 = 0.25) is a lithography coefficient that depends on many factors related to the chip manufacturing process, λ is the wavelength of the light used, and NA is the numerical aperture of the focusing optics, defining how much light can be collected [21]. Therefore, a smaller critical dimension can be achieved by using a combination of a shorter light wavelength and a larger numerical aperture while pushing k_1 as close as possible to the physical limit. In advanced CMOS patterning, multiple photolithography enhancement techniques are applied to achieve a higher feature density. For example, computer-aided optical proximity correction (OPC) is commonly used to compensate for image errors due to light diffraction or process effects. Utilizing the fact that light passing through a transparent media will undergo a phase change as a function of its optical thickness, phase shift masks (PSMs) are extensively applied to improve image resolution in photolithography [22, 23]. In addition, 193-nm ultraviolet (UV) immersion lithography is widely used to increase the resolution by a factor equal to the refractive index of the liquid medium between the final lens and the wafer surface. For future CMOS technology below $\sim 7\,\mathrm{nm}$, extreme ultraviolet (EUV) lithography ($\lambda \sim 13.5\,\mathrm{nm}$) may be required, however, at the expense of the high cost and low throughput [24, 25].

1.2 Emerging Devices Beyond CMOS

In the relentless pursuit of Moore's law, device scaling down to the nanometer regime has gradually reached a bottleneck caused by the aforementioned limitations, especially power

dissipation in microchips, have become a more and more challenging concern. Therefore, several emerging technologies beyond CMOS that explore various materials, novel device structures/functions, and alternative state variables have been proposed to further sustain the downscaling of ICs while reducing the cost in future decades.

As a conventional state variable, the electron charge is still used to represent digital bits with a capacitor charged and discharged. Tunnel field-effect transistors (TFETs), for instance, can potentially reach a subthreshold swing lower than the fundamental limit ($60\,\mathrm{mV/dec}$) [26]. With the electric polarization as the state variable, ferroelectrics (FEs) have provided multiple attractive options for non-volatile beyond-CMOS devices because such materials exhibit the nonvolatile electric polarization that can be directly switched by applying an electric field [27]. At first, ferroelectric random access memories (FeRAMs) were proposed as part of memory components, where a dielectric capacitor is replaced by a FE capacitor in a 1-transistor-1-capacitor (1T1C) cell configuration like a dynamic random-access memory (DRAM) [28–30]. The advantage of using a FE capacitor lies in its nonvolatility, and thus such a bit storage component does not require energy to refresh periodically. Other benefits of FeRAMs include faster write performance [31, 32], a much greater maximum read/write endurance and longer data retention time [32]. However, FeRAMs suffer from lower storage densities and higher cost.

In FE materials such as perovskites and organic poly(vinylidene fluoride) (PVDF) homopolymer, ferroelectricity can still survive in ultra-thin ferroelectric layers of a few nanometers [33–39], in which electronic transport is mainly dominated by quantum-mechanical tunneling. Therefore, ferroelectric tunnel junctions (FTJs), a device composed of an ultra-thin FE layer sandwiched between two different metallic electrodes, are proposed because giant tunneling electoresistance (TER) resulting from the opposite polarization states can possibly be a few orders of magnitude larger than the tunneling magnetoresistance (TMR) in magnetic tunnel junctions (MTJs) [38, 40–45].

Despite the potential applications of FE materials in emerging nonvolatile memory

devices, the use of conventional perovskites is limited by the material scalability and the lack of CMOS process compatibility. Recently, the discovery of the ferroelectricity in doped HfO_2 oxides reignited the research interest in ferroelectric-based transistors, also known as ferroelectric field-effect transistors (FeFETs), since such materials may overcome the aforementioned major limitations of the perovskite FEs [46–48]. A FeFET device structure is shown in Fig. 1.5(b). In addition, HfO_2 films doped with silicon (Si:HfO_2) were shown to exhibit ferroelectric properties in a wide temperature range between -100°C and 200°C [49]. A potential of 10-year data retention at 150°C was also demonstrated for the Si:HfO_2-based ferroelectric transistors [49]. Therefore, FE nonvolatile memories based on doped HfO_2 have been under intensive research investigation in recent years.

In the past decade, negative capacitance field-effect transistors (NCFETs) were proposed as potential emerging low-power logic devices by stabilizing the inherently metastable negative capacitance (NC) state of ferroelectric materials with a series capacitance [20]. Till today, NC-related research and debate are still ongoing in the hope of achieving low-power logic devices that can overcome the fundamental Boltzmann limit in the current CMOS transistors.

Alternatively, spintronics, which utilizes the electron spin as a computational state variable, is another promising beyond-CMOS option [50]. In most proposed spintronic devices, logic "1" and "0" are typically stored in the two ground states of a bi-stable nano-magnet with an energy barrier in between the states. The energy barrier inherently associated with the nano-magnet can be used to retain the magnetization state, thus enabling non-volatility. To write the data, physical phenomena including traditional spin-transfer torque (STT) [51], spin-orbit torque (SOT) [52, 53] and the magnetoelectric (ME) effect have been utilized [54]. Information read-out is generally achieved using the giant magnetoresistance (GMR) or tunnel magnetoresistance (TMR) in an MTJ [55]. Within the spintronic logic family, potential candidates like all spin logic (ASL) and spin wave logic are also well explored [56]. Interestingly enough, multiferroic materials such

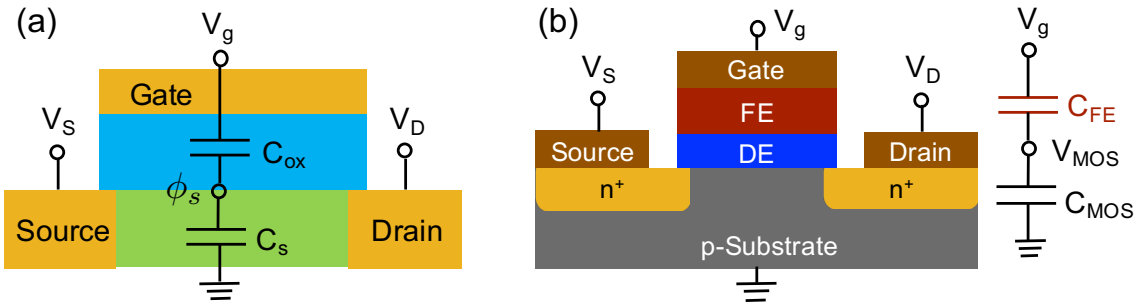

Figure 1.5: (a) A schematic circuit diagram of the gate stack in CMOS transistors. (b) A schematic n-type FE-based field effect transistors with the corresponding circuit diagram.

as bismuth ferrite $BiFeO_3$ (BFO) bridge the gap between the fields of ferroelectricity and spintronics through the ME effect, where magnetization can be switched with the applied electric field [54]. Therefore, taking advantage of the coupling of the ferroelectric and antiferromagnetic orders in the multiferroic material and the interface exchange coupling between the multiferroic layer and an adjacent ferromagnet layer, an antiferromagnet/ferromagnet heterojunction offers a new path to achieve low power and voltage-controlled spintronic devices [57, 58], which will be a topic of discussion in this thesis. Regarding other promising beyond-CMOS devices, a comprehensive overview can be found in [59–62] and the references therein.

1.2.1 Ferroelectrics

Ferroelectricity, which was discovered back in the 1920s [63], is a property of certain materials whose electric polarization can be reversed by the application of an external voltage. In recent decades, ferroelectric (FE) materials have attracted more and more research attention because of (i) the ability to switch their polarization by an externally applied voltage and (ii) spontaneous polarization under zero bias. Therefore, it is essential to not only investigate the fundamental physical mechanisms but also analyze the prospective ferroelectric-based applications at the device and circuit levels.

The main theoretical approaches that can well describe ferroelectric properties include *ab initio* (first-principles) calculations and phenomenological Landau theory [64].

First-principles calculations use an effective Hamiltonian to describe a quantum mechanical system and are able to solve important physical quantities at the atomic level. The work proposed here focuses on the latter approach, which models the system with order parameters and thermodynamic free energy.

The Landau theory was proposed to formulate the general theory of second-order phase transitions [64]. Based on the Landau theory of phase transitions, phenomenological models have been successfully applied to describe the ferroelectric properties since the first application by Ginzburg and Devonshire in the 1940s [65, 66]. In the Landau-Ginzburg-Devonshire (LGD) approach, the thermodynamic potential is generally expressed as a polynomial expansion in terms of the order parameter under a mean-field formulation. Without considering the elastic contribution, the single domain expression of Gibbs free energy is as follows,

$$\begin{aligned} G(\mathbf{P}) =& \alpha_1\left(P_1^2+P_2^2+P_3^2\right)+\alpha_{11}\left(P_1^4+P_2^4+P_3^4\right)+\alpha_{12}\left(P_1^2P_2^2+P_2^2P_3^2+P_1^2P_3^2\right) \\ &+\alpha_{111}\left(P_1^6+P_2^6+P_3^6\right)+\alpha_{112}\left[P_1^4\left(P_2^2+P_3^2\right)+P_2^4\left(P_1^2+P_3^2\right)+P_3^4\left(P_1^2+P_2^2\right)\right] \\ &+\alpha_{123}\left(P_1^2P_2^2P_3^2\right)+G_0, \end{aligned} \tag{1.5}$$

where the three-dimensional polarization vector $\mathbf{P} = (P_1, P_2, P_3)$ is the order parameter, and G_0 is the reference potential in the paraelectric state [67]. $\{\alpha_{ijk}\}$ are Landau expansion coefficients, which can be determined from first principles calculations based on experiments. $\alpha_1 = \alpha_0(T - T_c)$ at temperature T, where α_0 is a positive T-independent constant and T_c is the transition temperature. The four possible solutions of $\mathbf{P}$ correspond to different crystal structures as listed in Table 1.1.

Based on the thermodynamic potential, the energy landscape of ferroelectrics below T_c can be described by a double-well potential, as shown in Fig. 1.6(a). From the energy point of view, there exist two stable spontaneous polarization states, which can be reversed by an externally applied electric field. As shown in Fig. 1.6(a), the application of an electric field

Table 1.1: Polarization states and the corresponding structures [68]

Structures	**P**
Cubic	$P_1^2 = P_2^2 = P_3^2 = 0$
Tetragonal	$P_1^2 = P_2^2 = 0,\ P_3^2 \neq 0$
Orthorhombic	$P_1^2 = P_2^2 \neq 0,\ P_3^2 = 0$
Rhombohedral	$P_1^2 = P_2^2 = P_3^2 \neq 0$

lowers one of the energy minima, and thus the polarization is switched to the favorable state in order to minimize the total energy of the system. The polarization switching dynamics of ferroelectrics was first formulated with the Landau-Khalatnikov (LK) equation in a single domain approximation [69]. Similar to the dielectrics, the electric displacement field of FEs (Q_{FE}) with the total out-of-plane polarization P can be derived as

$$\begin{aligned} Q_{\text{FE}} &= \epsilon_0 E_{\text{FE}} + P \\ &= \epsilon_0 E_{\text{FE}} + (P_{\text{FE}} + P_{\text{d}}) \\ &= \epsilon_0 E_{\text{FE}} + (P_{\text{FE}} + \chi \epsilon_0 E_{\text{FE}}) \\ &= \epsilon_0 (1 + \chi) E_{\text{FE}} + P_{\text{FE}} \\ &= \epsilon_0 \kappa E_{\text{FE}} + P_{\text{FE}}, \end{aligned} \tag{1.6}$$

where ϵ_0 is the vacuum permittivity and E_{FE} is the electric field applied to the FE materials. Here for a more accurate description of the FE polarization, P is decomposed into two terms: one is the out-of-plane polarization P_{FE} that accounts for the nonlinear FE response described by Eq. (1.5), and the other is P_{d} that describes the linear dielectric response before polarization reversal. In Eq. (1.6), κ is called the background dielectric constant with an electric susceptibility χ associated with the linear response of FEs [70]. In the LK equation, the switching rate of P_{FE} is described by the Gibbs free energy decrease with respect to polarization, and the equilibrium state is reached when the total free energy is minimized. More detailed formalism will be given in the next few chapters.

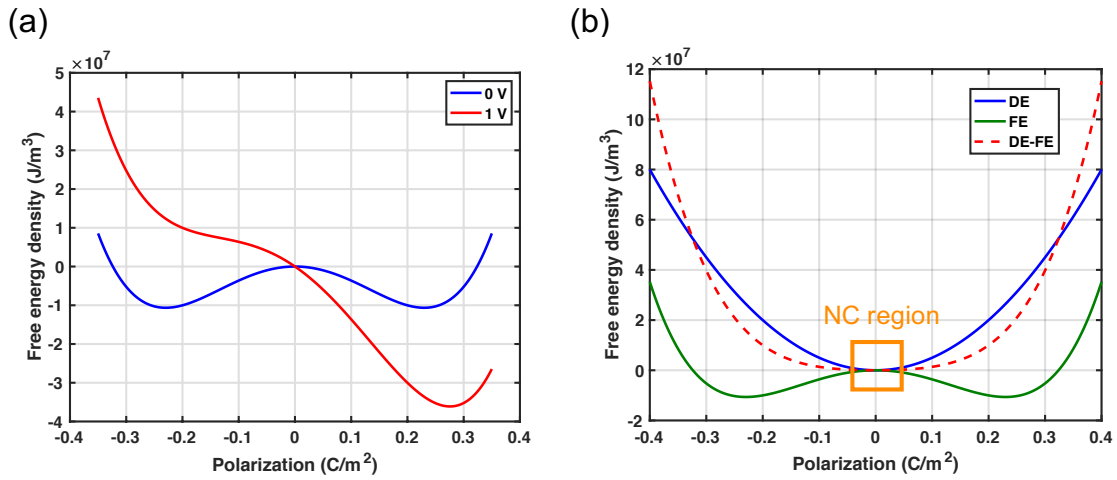

Figure 1.6: (a) Energy profiles of FE materials under an applied voltage. (b) The energy profiles of the FE layer and the DE layer in an FE-DE stack, where the NC region was proposed to be stabilized by the DE layer in the stack system during FE polarization reversal.

Traditionally, the classically studied FE materials include $BaTiO_3$ (BTO), $PbTiO_3$ (PTO), $PbZr_{1-x}Ti_xO_3$ (PZT) and $SrTiO_3$ (STO), which belong to perovskite complex oxides with a chemical formula of ABO_3, where B is a transition metal element [71]. Take BTO for example. Above T_c, the FE materials are in the paraelectric phase with Ti^{4+} in the center of the cubic cell as shown in Fig. 1.7(a). Below T_c, the unit cell of BTO is tetragonally distorted with lattice constants of $a = 3.994\,\text{Å}$ and $c = 4.038\,\text{Å}$ [72], and therefore, the central ion Ti^{4+} is not at the center of the symmetry of the unit cell. Such off-centering of the central ion (Ti^{4+} in BTO) in the non-centrosymmetric crystal structure leads to a spontaneous dipole moment (or electric polarization) under zero bias. In this case, BTO is in the ferroelectric phase with the spontaneous polarization $P_s = q\delta/(ca^2) \sim 0.3\,\text{C/m}^2$, where q is the elementary charge and δ is the displacement of the central ion off the center (typically on the order of picometers) [38]. With an applied voltage larger than the coercive voltage (V_c), the central ion displacement is further pushed away from the center, depending on the direction of the applied field, as shown in Fig. 1.7(b). The off-centering displacement of the central ion in the two opposite directions corresponds to the two different minima of the ferroelectric energy landscape shown in Fig. 1.6(a). Moreover, the existence of

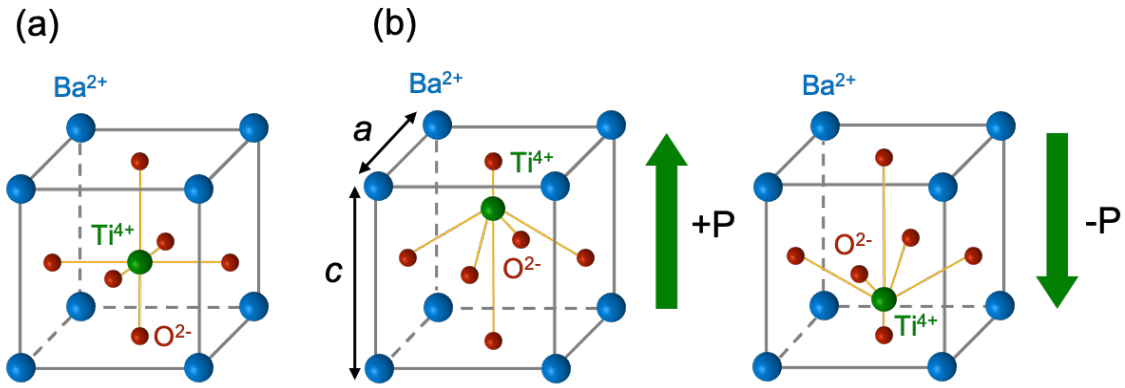

Figure 1.7: (a) Crystal structure of $BaTiO_3$ in paraelectric phase above T_c, where there is no spontaneous polarization under zero bias. (b) Crystal structure of $BaTiO_3$ in ferroelectric phase below T_c, where there exist two spontaneous polarization states under zero bias, adapted from [74].

two stable polarization states under zero bias results in the hysteresis loop in the FE materials [38, 73].

In addition, perovskite bismuth ferrite $BiFeO_3$, the only single-phase multiferroic known so far that exhibits both ferroelectric and antiferromagnetic properties at room temperature [57, 75, 76], has been extensively studied because of its unique property to rotate the ferromagnetic order with an external electric field. Other than the inorganic compounds, organic poly(vinylidene fluoride) with trifluoroethylene (PVDF-TrFE) ultra-thin films are also found to demonstrate ferroelectricity [43, 77, 78].

Most perovskite FEs can be categorized into two types according to their phase transition behaviors based on the Landau theory. For the first-order type materials such as BTO and PTO, the Landau coefficients of an FE satisfy $\alpha_1 < 0$, $\alpha_{11} < 0$ and $\alpha_{111} > 0$ [67, 79]; on the other hand, α_{11} is positive for materials like $PbZr_{0.48}Ti_{0.52}O_3$, which have second-order phase transitions [79]. When a paraelectric phase of FEs is cooled down below the ferroelectric transition temperature, particular domain patterns form due to the change in the crystal structure [80]. For example, a cubic lattice system can be stretched to a tetragonal one, where the spontaneous polarization can be along [100], [010], [001] directions of the cubic paraelectric phase. The stability of the domain structures depends on

FE materials as well as the fabrication conditions, such as contact properties and substrate constraints. The domain structures are best described by the multi-domain phase field approach, which takes various energy contributions into account [80].

Until very recently, HfO_2-based FE films as thin as $10\,\mathrm{nm}$ were reported to be compatible with the complementary metal-oxide-semiconductor (CMOS) technology [46, 81]. As a result, $Hf_{1-x}Zr_xO_2$ (HZO) is currently the most promising candidate for the achievement of ferroelectric field-effect transistors (FeFETs) as non-volatile memories (NVMs) and negative capacitance field-effect transistors (NCFETs) as ultra-low power logic devices because of its scalability and compatibility with the CMOS technology. HfO_2 itself, as mentioned in Sec. 1.1.1, is commonly used as a high-κ dielectric to address the leakage problem as the conventional SiO_2 oxide is extremely scaled down with Moore's law. It was experimentally found that SiO_2 oxide doped with Zr or Si shows the properties of ferroelectricity [82–84]. In particular, the doping percentage of Zr changes the crystal structure phases of HZO films and thus controls their electrical characteristics [84]. Without Zr doping, HfO_2 is a conventional high-κ dielectric. With a small amount of Zr doping ($x < 0.5$), HZO is in the ferroelectric phase. As the the Zr doping percentage increases, HZO gradually shows more pronounced anti-ferroelectric behaviors.

So far, several potential ferroelectric-based electronic devices have been proposed and intensively investigated both experimentally and theoretically. The most basic yet important electronic component is ferroelectric capacitors. A ferroelectric capacitor is simply composed of a ferroelectric film sandwiched between two conducting electrodes. The stack heterostrucure is shown in Fig. 1.8. The fundamental characteristics of FE capacitors include remanent polarization (P_r) and coercive field (E_c). Conventionally, the semi-empirical Kolmogorov-Avrami-Ishibashi (KAI) model can successfully describe the polarization switching dynamics under a constant voltage pulse [85–88]. Attributing the polarization switching dynamics to domain nucleation and wall propagation in the FE materials, the KAI model describes the amount of switched polarization ΔP as a function

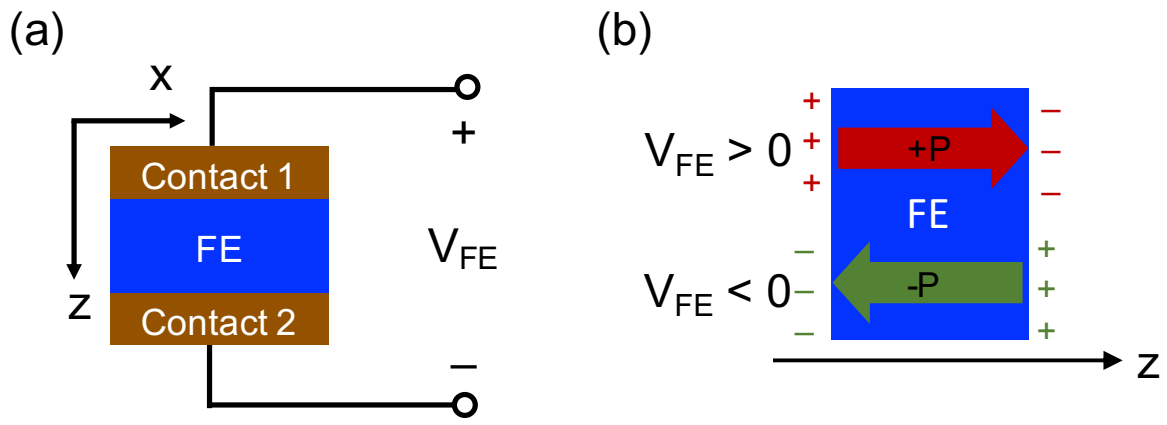

Figure 1.8: (a) A schematic diagram of a ferroelectric capacitor. (b) The operation of voltage-controlled polarization state switching.

of time t,

$$\Delta P(t) = 2P_r\{1 - \exp\left[-(t/t_0)^n\right]\}, \tag{1.7}$$

where $\Delta P/(2P_r)$ is the polarization switching rate, t_0 is the characteristic switching time, and its exponent n indicates the film dimensionality for the domain growth. Generally, $n = 3$ for FE bulks whereas $n = 2$ for FE thin films. However, for complex domain growth dimensionality, non-integer n was also reported [89–91]. In nonepitaxial FE films such as polycrystalline Pb(Zr,Ti)O_3 commonly used in FeRAMs, a domain cannot propagate indefinitely due to pinning caused by numerous defects. In contrast to the KAI model, nucleation-limited-switching (NLS) model and its variations were proposed to describe the domain-switching kinetics and relaxation using the domain nucleation and growth/propagation distribution resulting from defects [92–94].

Remanent polarization (P_r) in ferroelectrics is ideally non-volatile, and thus enables devices to retain their stored information even when switched off. Sub-micrometer thick ferroelectric thin films are commercially used in ferroelectric random access memories (FeRAMs) with the advantages of low-power consumption, fast write speed and good cycle endurance [43]. However, current FeRAMs require information rewriting after readout (destructive readout), and their density is limited to the gigabit regime [43, 95]. In

contrast to FeRAMs, an ultra-thin FE layer is sandwiched between two different electrodes as a ferroelectric tunnel junction (FTJ). The ultra-thin FE with a thickness of a few nanometers ensures that electronic conduction is enhanced through quantum tunneling. In addition, because of the asymmetric contact properties (screening lengths or interface effect), the energy barrier for the tunneling effect can be modulated by the polarization in opposite directions, which leads to high and low resistance states. Inherent from the voltage-controlled spontaneous polarization, FTJs feature high speed program/erase in nanoseconds and low power consumption [96]. As two-terminal devices, FTJs with giant tunnel electroresistance (TER) potentially have the advantages of high density and non-destructive readout in crossbar memory arrays. In addition to binary NVMs, FTJs are also a prospective candidate to achieve neuromorphic circuits due to their memristive properties [43]. So far, experiments have demonstrated FTJs with a large ON/OFF current ratio up to 10^7 at room temperature [38, 39, 42, 45, 96, 97]. For FTJs to be further adopted in memory applications, the reliability issues (such as switching endurance and data retention) that are caused by the charged defects and the depolarization field still need intensive investigation from the technological perspective [96]. In general, FTJs, in which information is stored as ferroelectric polarization, may lay the foundations for nonvolatile data storage and neuromorphic hardware devices with large ON/OFF current ratios [43, 96].

As the pursuit of Moore's law faces more and more challenges, researchers have been attempting to develop novel electronic devices that not only consume less power but allow high operating speeds as well. From fundamental thermodynamics mentioned in Sec. 1.1.2, the subthreshold swing is limited to $60\,\mathrm{mV/decade}$ at room temperature for conventional CMOS transistors. About a decade ago, it was theoretically proposed that the inherent negative capacitance (NC) characteristic of a ferroelectric could be used to overcome such physical limit [20]. The double-well energy landscape of FE materials implies that the electric polarization undergoes a thermodynamically unstable NC region when switching

from one state to the other. Based on Eq. (1.5) and Table 1.1, the capacitance of a single domain FE with the tetragonal structure near polarization reversal ($P \rightarrow 0$) can be expressed as

$$C_{\text{FE}}(P_3) = \left(\frac{\partial^2 G}{\partial P_3^2}\right)^{-1} \approx \frac{1}{2\alpha} = \frac{1}{2\alpha_0(T - T_c)}. \tag{1.8}$$

When $T > T_c$, the FE is in the paraelectric phase and $C_{\text{FE}} > 0$, whereas when $T < T_c$, $C_{\text{FE}} < 0$, which corresponds to the negative curvature of the FE energy profile.

When another normal capacitor is in series with the FE capacitor, the unstable energy maximum of FE becomes the minimum point of the system's total energy, as illustrated in Fig. 1.6(b). The stabilization of the unstable NC region directly leads to a voltage amplification at the internal node compared to the applied voltage. In an NC field-effect transistor (NCFET), an FE layer is deposited at the gate, forming metal-ferroelectric-(metal)-insulator-semiconductor (MF(M)IS) structures [98]. According to the NC effect, when an external gate voltage is applied, the NC region of the FE layer (with a negative C_{ox} in Fig. 1.5) can be stabilized by the insulator and CMOS capacitance. Hence, m in Eq. 1.2 can be smaller than 1, which results in a subthreshold slope S smaller than the thermodynamic limit of $60\,\text{mV/decade}$.

Following the theoretically proposed NC effect, lots of experimental and theoretical efforts have also been dedicated to the realization of NCFETs. On the one hand, experimentalists have tried to characterize the NC effect inside FE materials [99]. Small signal measurements show that the total capacitance of a DE/FE bilayer or superlattice heterostructure is found to be larger than the DE capacitor, which verifies the single domain approximation [99–103]. However, such enhancement was not found in multi-domain HZO capacitors externally connected to a DE capacitor [104]. The effect of the metal interlayer on FE polarization is still being investigated. In transient RC measurements, a V_{FE} drop is observed during the pulse switching when the FE capacitor is in series with a rather large resistor [105, 106]. This finding demonstrates that the FE experiences a transient NC, where V_{FE} decreases during capacitor charging; hence, the corresponding differential

capacitance is negative. Although the voltage drop observed in the experiments can be attributed to the mismatch between the switching rates of FE free charge and polarization at a pulse voltage, the single domain LK model fails to describe the measured polarization and V_{FE} transient responses [105, 107]. Researchers also find that the experimental measurements can be described by the KAI model and Preisach-Miller model, which are the conventional approaches based on the multi-domain nature of FEs. As such, the transient NC effect may include both single and multi-domain dynamics [99]. With a ramp voltage applied to FE and DE series combinations, a differential voltage amplification on the DE capacitor is also observed [99, 108]. Besides, NCFETs have also been fabricated to examine the subthreshold swing, ON current, drain-induced barrier lowering (DIBL), and output conductance [99, 109]. Although a steep slope was observed, there is hysteresis during the voltage sweep, which is undesirable for logic devices [110–113]. The frequency operation range of NCFETs is also an issue due to the relatively slow response time of FE domain switching [114]. Experimental research is still underway for the achievement of hysteresis-free ultra-low power NCFETs [113, 115, 116]. On the other hand, theoretical works are needed to not only explore the device parameters but elucidate physical mechanisms underlying FE properties. In addition, simulations combined with SPICE simulators also serve to facilitate performance analyses of the NC effect on logic devices at the circuit level [117, 118].

As mentioned earlier, FeFETs based on doped HfO_2 are considered a promising candidate for beyond-CMOS nonvolatile memory devices. However, for the possible realization of FeFETs, there are still various reliability concerns. In particular, the mobility degradation, threshold voltage (V_{th}) instability and other reliability issues such as negative and positive bias temperature instability and enhanced stress-induced leakage current are attributed to the high density of intrinsic HfO_2 defects. The main origin of traps in HfO_2 dielectrics are believed to be oxygen vacancies and oxygen interstitial atoms. These intrinsic defects can serve as electron and/or hole traps, and thus have a strong impact

on the behavior of the high-k CMOS logic transistors.

In the literature, the impact of charge trapping on the performance of HfO_2-based FeFETs have been experimentally demonstrated to induce a V_{th} shift in the opposite direction to that caused by the ferroelectric switching for the same polarity of the gate voltage [49, 119]. For example, electrons trapped within the gate dielectric at positive gate voltage result in a positive shift of the drain current-gate voltage (I_{D}-V_{G}) characteristic. On the other hand, the positive FE polarization induced by a positive gate voltage leads to a negative I_{D}-V_{G} shift. Therefore, a superposition of the two mechanisms will result in the undesirable reduction of the memory window for FeFET devices. In addition, parasitic charge trapping effects were also argued to cause the endurance and retention degradation of HfO_2-based FeFETs. As a result, the trapping dynamics and its interplay with the ferroelectric switching has to be studied both experimentally and theoretically for the purpose of nonvolatile FeFET realization.

1.2.2 Magnetoelectric multiferroics

In addition to FE-based electronic devices, spintronic devices are also considered a promising candidate for beyond-CMOS logic and memory applications due to the potential for ultra-low energy switching and nonvolatility. Among proposed low-power and magnetic-field free devices, magnetoelectric devices can alleviate the problem of a high threshold current and the accompanying joule-heating effect during and even after magnet switching. Conventionally, in an MTJ, either an extra spin current or a careful control of the voltage pulse width has to be applied for the magnetic moment of a ferromagnet to switch $180°$. Multiferroic materials that have at least two of the ferroic properties, including ferroelectricity, ferromagnetism, and ferroelasticity, can successfully switch the magnetic moment of the adjacent ferromagnet by $180°$ when a reverse electric field is applied, as experimentally demonstrated in the case of $BiFeO_3$ (BFO).

In general, bulk BFO has a rhombohedral distorted perovskite structure and belongs

to the space symmetry group R3c, whereas the crystal structure and the space group in a thin film BFO may vary from tetragonal to orthorhombic depending on a compressive or tensile strain [120, 121]. Possessing ferroelectricity, G-type antiferromagnetism, and weak magnetization, multiferroic BFO has both the Curie temperature $T_c \sim 1103\,\mathrm{K}$ and the Neel temperature $T_N \sim 643\,\mathrm{K}$ well above room temperature, making BFO a promising candidate for room-temperature device applications [122]. The ferroelectricity of BFO originates from the displacement of Bi^{3+} ions under an applied electric field, and the saturation polarization in BFO can be as large as $90\,\mu\mathrm{C/cm^2}$ along [001] in a thin film structure. Note that the weak magnetism in BFO is observed only in thin-film structures with thicknesses below approximately $200\,\mathrm{nm}$, where the exact critical thickness depends on the substrate strain [123]. Furthermore, the spin cycloid dominates the magnetic structure in the bulk single-crystalline BFO, which results in the net magnetic moment to be zero.

One of the as-grown domain configurations of BFO was experimentally found to show a stripe pattern with 71° domain walls. When an out-of-plane voltage is applied to such a BFO film, both polarization states switch in two steps: 71° switching in the in-plane direction followed by an out-of-plane 109° switching, resulting in an overall 180° switching. Interesting enough, the polarization stays on the same crystal plane during the 180° reversal, which was argued to be attributed to the elastic constraints from the rhombohedral crystal structure of BFO [57]. Taking advantage of the coupling of the ferroelectric and antiferromagnetic orders in BFO and the interface exchange coupling between BFO and an adjacent ferromagnetic CoFe layer, several experiments have demonstrated voltage-controlled 180° switching of the magnetic order in CoFe [57, 124, 125]. To evaluate the potential performance of the voltage-controlled BFO/CoFe heterojunction device in memory or logic devices, it is crucial to develop a unified simulation framework for the study of the transient response, switching time, and the switching probability of the magnetic order in the CoFe layer. In such a physical model,

one of the key elements for the deterministic magnetic order switching is the theoretical description of the unique two-step switching process in BFO under an out-of-plane applied field, which will be one of the research topics in this thesis.

1.3 Thesis Overview

Although a considerable amount of research effort has been put into a thorough understanding of ferroelectric and multiferroic materials both theoretically and experimentally, their fundamental physical behaviors and mechanisms have not yet been completely understood. Therefore, it is critical to perform comprehensive simulations and analyses with the aid of more experimental measurements to develop a deep understanding of the main physical phenomena for the design and optimization of the devices and circuits these materials may enable. From the physics point of view, experimentally calibrated first principles calculations and phenomenological approaches are needed for a better understanding of the fundamental physics underlying these two kinds of materials. From the device point of view, SPICE compact models are of great importance in performance analyses and benchmarking of emerging devices, which facilitate the evaluation and implementation of these beyond-CMOS devices in large circuits. Overall, this thesis is primarily dedicated to (i) the research exploration of emerging devices using ferroelectricity (or electric polarization), especially on the deep physical understanding of the FE materials and the associated NC properties, and (ii) the switching mechanisms of voltage-controlled antiferromagnet/ferromagnet heterojunctions involving the ME effect for the purpose of their potential applications in low-power digital logic circuits or nonvolatile memory arrays in the beyond-CMOS era.

In this chapter, a comprehensive overview of technological advances driven by CMOS scaling is given to highlight the motivation behind this thesis. Before we dive into the details of each chapter, the background knowledge for both ferroelectrics and multiferroics that will be covered in this thesis is also presented to give readers a better understanding

of the developed simulation frameworks. The rest of this thesis is organized as follows. Chapter 2 presents a circuit-compatible SPICE module of FE materials based on the single domain LGD theory and its application to the analyses of NCFETs at the device and circuit levels. In Chapter 3, a three-dimensional phase-field framework is implemented by solving the time-dependent Ginzburg-Landau (TDGL) equation and Poisson's equation self-consistently using the SPICE simulator. Calibrated with experimental measurements, the simulation results provide important physical insights into the multi-domain FE. In Chapter 4, a theoretical study is performed on the hysteresis-free charge-boost effect observed experimentally in metal-ferroelectric-insulator-metal (MFIM) capacitors. For the observed hysteresis-free charge enhancement in MFIM, the simulations with the dielectric leakage and interfacial trapped charges provide a physical picture for a better understanding of the underlying mechanisms, which may be physically different from the alleged NC stabilization and capacitance matching. In Chapter 5, physics-based formalism is developed to capture the two-step FE polarization switching process in a unified modeling framework to better understand the fundamental physics of the switching mechanisms of the antiferromagnet/ferromagnet heterojunction by taking $BiFeO_3$/CoFe heterojunction as an example. The models are calibrated with experimental results and demonstrate that the switching of the ferromagnet in the antiferromagnet/ferromagnet heterojunction is caused by the rotation of the Neel vector in the antiferromagnet instead of being driven by the unidirectional exchange bias at the interface as was previously speculated. Lastly in Chapter 6, the conclusions of the thesis works are presented and the future directions of the research on emerging devices based on ferroelectricity are pointed out as well. Ultimately, the works involved in this thesis are aimed at potentially paving the way for the development of beyond-CMOS devices based on FE and multiferroic materials.

CHAPTER 2

SINGLE DOMAIN PHENOMENOLOGICAL APPROACH

2.1 Overview

As mentioned in Chapter 1, intensive research on negative capacitance field-effect transistors (NCFETs) is underway because NCFETs have been regarded as one of the promising beyond-CMOS devices with a potential to continue Moore's law. Although there have been device simulations on the performance of NCFETs in the literature [98, 126–129], the overall analysis at the circuit level still needs further investigation [128, 130–132]. In addition to the performances of NCFET-based circuits, we bring up three key aspects of NCFET characteristics that have not been widely discussed yet. First, proper circuit initialization in SPICE simulations has not been discussed adequately. Second, the impact of the NC effect on the internal gate voltages of NCFETs when they are in the off-state has not been investigated. This is fundamentally important because as will be shown in the later sections, the negative (or beyond-VDD) voltage induced on the internal node suppresses the leakage current of the transistors in the off-state. Third, the physical parameter of internal FE resistivity (or viscosity coefficient) ρ plays an important role in the dynamic switching of the ferroelectric. Because of a wide range of ρ values observed in different experiments [109, 133], it is important to understand the impact of ρ on the circuit-level performance so that the NCFET-based logic gates can be better designed [107].

In this work, we perform circuit simulations and analyses of NCFET-based logic gates and interconnects, with the above-mentioned key points carefully investigated. We start by emphasizing the importance of initial conditions for FE-based device simulations. We then discuss the impact of the NC effect on the off-currents of NCFETs and the performances of NCFET NANDs based on their activity factor, α. Threshold voltage adjustment is proposed

to improve the potential performance of the devices in high α operation. In addition, we study the influence of internal resistivity in NCFETs on the circuit-level performance. Last, we explore the interconnect application by optimizing the numbers and sizes of repeaters in interconnects using NCFETs and compare their performance with their CMOS counterparts. Based on compact SPICE component modules, our modeling approach can be extended to investigate design aspects of larger scale circuits.

2.2 The Circuit Model for Ferroelectric Capacitors

From the perspective of Gibbs free energy minimization, the single domain Landau-Khalatnikov (LK) equation approximately relates the FE polarization and the electric field inside the FE [69]:

$$\rho \frac{\partial \mathbf{P}}{\partial t} = -\frac{\partial G}{\partial \mathbf{P}}, \tag{2.1}$$

where $\mathbf{P}$ is the electric polarization, ρ is the internal resistivity (or viscosity coefficient), G is the Gibbs free energy density defined in Eq. 1.5. With an electric field applied to a tetragonal FE material in the out-of-plane direction (z), $\mathbf{P} \approx (0, 0, P)$, and the corresponding thermodynamic potential reduces to

$$G = \alpha_1 P^2 + \alpha_{11} P^4 + \alpha_{111} P^6 - E_{FE} P. \tag{2.2}$$

Therefore, the voltage-charge relationship under an electric field $E_{FE} = V_{FE}/t_{FE}$ can be expressed as

$$V_{FE} = t_{FE} \left(\rho \frac{\mathrm{d}P}{\mathrm{d}t} + 2\alpha_1 P + 4\alpha_{11} P^3 + 6\alpha_{111} P^5 \right), \tag{2.3}$$

where V_{FE} is the voltage across the FE capacitor, t_{FE} is the FE thickness, and $\{\alpha_1,$ $\alpha_{11},$ $\alpha_{111}\}$ are Landau expansion coefficients [64, 69, 118]. According to Eq. 2.3, a SPICE circuit model can be developed with the FE modeled as a resistor in series with a capacitor [117]. The capacitor describes the nonlinear relationship between the

```
V(res) <+ r*I(res);
V(fb) <+ tFE*( 4*beta*pow(V(q)/A,3) + 6*gamma*pow(V(q)/A,5) );
V(q) <+ gain*(V(cap) - V(fb));
I(cap) <+ ddt(V(q));
```

Figure 2.1: A Verilog-A module of single domain FE capacitors, where `q` is the dummy node for charge, `r` $= \rho t_{\text{FE}}/A$ is the internal resistance, and `gain` $= A/(2\alpha)/t_{\text{FE}}$ is the feedback gain. The internal resistor branch, internal capacitor branch, and feedback branch are represented by `res`, `cap` and `fb`, respectively.

polarization and the applied voltage, while the resistor represents the internal impedance corresponding to the charge mobility. Fig. 2.1 shows the Verilog-A behavioral module of FE capacitors. The baseline CMOS transistors used in this work are the 16 nm technology node high-performance (HP) model from Predictive Technology Model (PTM) [134]. For NCFETs, an FE film is stacked on the metal gate of the baseline CMOS transistor. The parameters used in this work are taken from [107], which fit the experimental measurement of $Hf_{0.7}Zr_{0.3}O_2$ (HZO) capacitors in [133]. Without the leakage path, this circuit configuration is equivalent to the NCFET structure without an internal metal layer in between the FE and the transistor gate oxide [135]. In reality, the polarization of the FE layer can be non-uniform due to potential variations in the transistor channel when an intermediate metallic layer is absent. This possible non-uniformity has been ignored in this work. Under such circuit setup, the self-consistent transient responses are simulated by HSPICE simulators.

2.3 SPICE Simulation

2.3.1 NCFET-based circuit initialization and internal gate voltage amplification

We start by emphasizing the importance of circuit initialization for FE-based devices in an inverter. As explained in [135], the zero initial polarization ($Q_F(t = 0) = 0$) is a stable state when the input gate voltage $V_G = 0$ V. We perform our simulations with this condition at $t = 0$ assuming voltages at all nodes including power supply nodes are zero. This means the circuit has been off for a long time and all capacitors have been discharged.

With a small delay, the supply voltage is turned on without any changes in the input voltage, which has two effects. First, the internal node of the p-FET becomes negative due to the voltage amplification produced by the FE (Figure 2.2(b, bottom)), and the polarization of the FE is shifted accordingly (Figure 2.2(d)). Second, as the drain voltage of the n-FET rises to VDD, the internal node of the n-FET also becomes negative. However, this negative voltage is smaller than that of the p-FET because this amplification happens only through the gate-to-drain capacitance. In the case of p-FET, source, channel and drain all transition to VDD; therefore, the induced negative voltage is far greater.

Once the input voltage is switched to VDD, the internal node of the n-FET goes considerably above VDD. On the other hand, the internal voltage of the p-FET goes slightly above VDD. This small increase beyond VDD is again due to the fact that the drain voltage of the p-FET has now switched low. At VDD $= 0.4$ V, the internal gate voltage is 0.65 V (-0.3 V) when the n-type (p-type) NCFET is in the on-state. In the off-state, the internal voltages are -65 mV and 0.48 V for n-FET and p-FET, respectively. As will be seen later, the relatively small negative (beyond-VDD) voltage induced on the internal node of the n-FET (p-FET) has a considerable impact on suppressing the leakage current.

The importance of the proper initialization is demonstrated in Figure 2.2(b, top). When the supply voltage is always on, the gate-to-source capacitance of the p-FET is pre-charged by VDD, which will make the conditions for n-FET and p-FET asymmetrical. When the input voltage transitions to VDD, the internal voltages of the n-FET and p-FET rise above VDD almost equally and when the input transitions back to zero, the internal voltages will both switch back to nearly zero. This way, the FE layer improves the on-current of the n-FET while it suppresses the leakage current in the p-FET.

Note that even when initialization is done properly in simulations (Figure 2.2(b, bottom), (d)), the n-FET and p-FET responses are not completely symmetrical because of different gate-drain parasitic capacitances associated with n- and p-FET. In practice, the asymmetry between n- and p-type NCFETs may also arise from different growth and stress

(a)

Parameter	Value
t_{FE} (nm)	10
α (m/F)	-4×10^8
β ($m^5/F/C^2$)	3.7×10^9
γ ($m^9/F/C^4$)	1.1×10^9
L (nm)	16
W_p [1](nm)	180

[1] PMOS gate width.

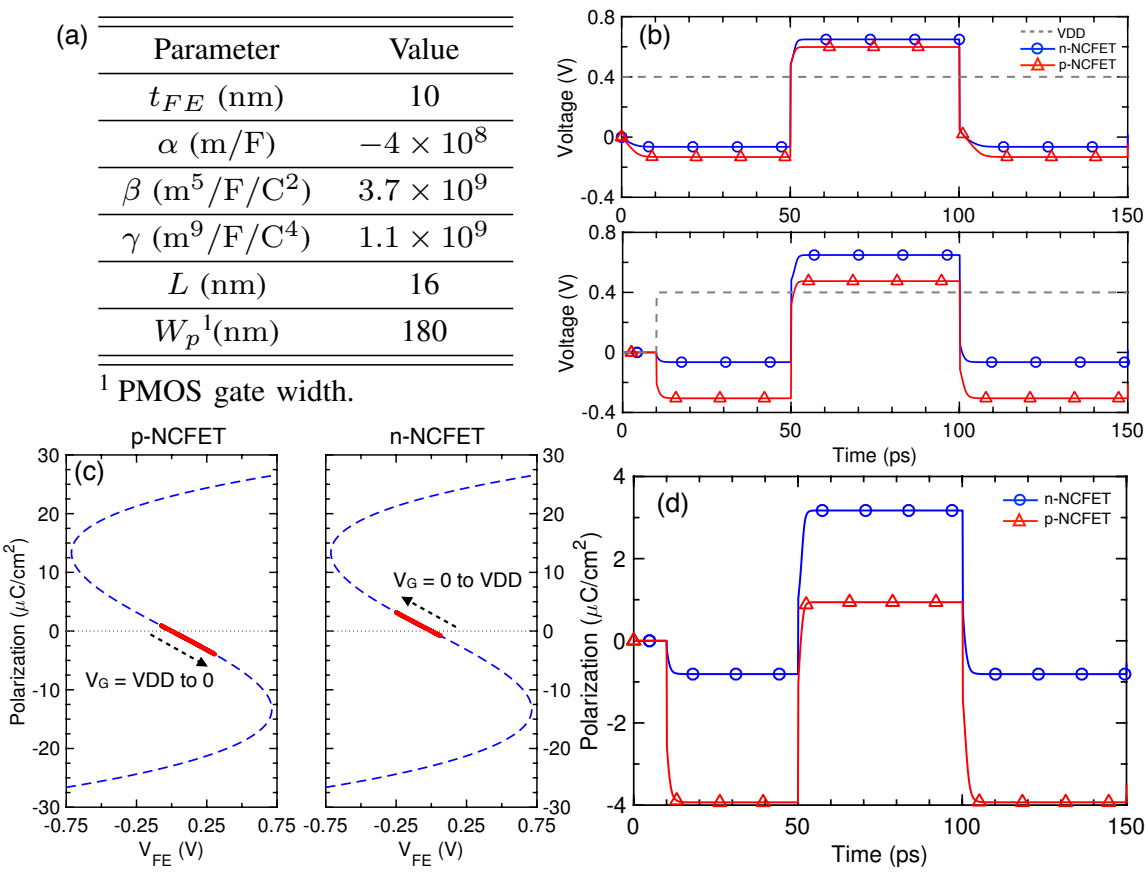

Figure 2.2: (a) Parameters used in this work. (The PMOS area is fixed in NAND analysis.) (b) Transient responses of internal gate voltage of n- and p-type NCFETs with $VDD(t = 0) = 0.4$ V (top) and $VDD(t = 0) = 0$ V (bottom). (c) Corresponding polarization dynamic change in the hysteresis curve during voltage step-up. (d) Transient responses of polarization for n- and p-type NCFETs with $VDD(t = 0) = 0$ V.

conditions.

2.3.2 Design trend for complex logic gate

To further investigate FE-based complex logic gates, we first consider 2-input NANDs driving fan-out of 4 (FO4) inverters with the energy-delay product (EDP) as the figure of merit. Here, the driven inverters are composed of the same type of devices. In other words, CMOS NANDs and NCFET NANDs drive CMOS and NCFET inverters, respectively. For NAND gates, the on currents of the p- and n-type devices are matched by adjusting the size of n-FET. The EDP is calculated in the worst-case scenario where the input pattern

is such that only one p-FET is turned on. Figure 2.3 shows that, at the activity factor $\alpha = 2\%$, the baseline HP CMOS NAND has the best EDP when operated at around 0.5 V, whereas the NCFET NAND can have the optimal EDP when operated at a lower VDD. The improvements in terms of EDP and optimal operating voltage for NCFET NAND are mainly due to the internal voltage amplification effect mentioned in section 2.3.1. Note that the larger internal resistivity ρ causes NCFETs to have an extra delay (hence larger EDP). The impacts of key design parameters are discussed below.

Activity Factor

As shown in Figure 2.4(a), NCFET NANDs can achieve lower EDP than CMOS NANDs when operated at low α. This indicates that the leakage current is significantly suppressed by the negative capacitance which induces negative (or beyond-VDD) gate voltages on the devices when they are off. However, the performance of NCFET NANDs gradually becomes worse than that of CMOS NANDs as α increases beyond a certain point. This is because larger load capacitances of NCFETs lead to larger switching energy that dominates the total energy when α is high. The problem of EDP degradation for NCFET NANDs at high α can be alleviated by lowering the threshold voltage of both types of transistors at the cost of slightly larger EDP at low α. Figure 2.4(a) also shows that, by properly designing the devices, the EDP of NCFET NANDs may be better than that of conventional CMOS NANDs for a wide range of α. Once the threshold voltage is lowered, the optimal VDD is also reduced. Note that the optimal trade-off between large on current and low leakage power in such engineering depends on the specific application and workload.

Impact of Viscosity Coefficient

Due to the wide range of reported values for ρ, here we vary its value from $0\ \Omega\mathrm{m}$ to $0.02\ \Omega\mathrm{m}$ and study the EDP of NAND gates with various numbers of inputs. In Figure 2.4(b), it can be seen that the extra FE polarization switching delay introduced by a larger ρ remains

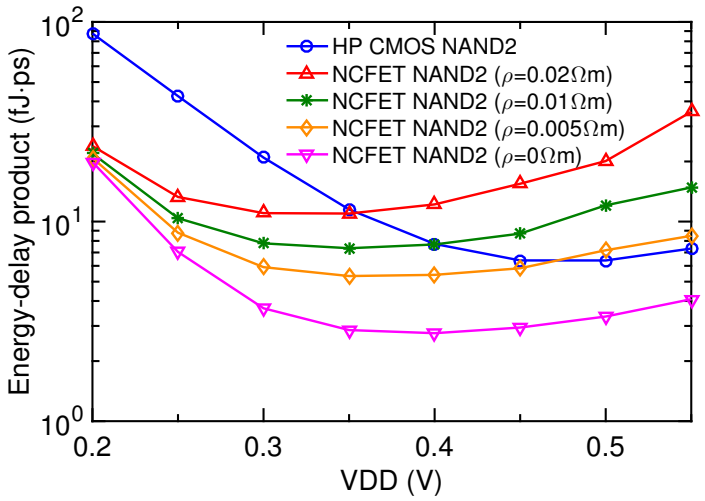

Figure 2.3: The energy-delay product of 2-input HP CMOS NAND and NCFET NAND with nonzero internal resistivity at $\alpha = 2\%$ of 2 GHz clock frequency at various VDDs.

constant as the number of inputs increases for NCFET NANDs. In other words, the FE layers in the switching devices switch in parallel and the relative penalty imposed by a larger ρ decreases as the number of inputs increases. For instance, the relative penalty for $\rho = 0.02\ \Omega\mathrm{m}$ (compared to $\rho = 0\ \Omega\mathrm{m}$) is reduced from 342% to 265% as the number of inputs increases from 2 to 5. This result indicates that the disadvantage of NCFET NANDs due to large FE internal resistance can be alleviated for large numbers of inputs; hence, it is more desirable to use complex logic gates for NCFET-based circuit applications if ρ is large.

2.3.3 Repeater insertion analysis

For NCFET inverters to have symmetric rise and fall delays, the size aspect ratio is set as 2.5 for supply voltage $VDD = 0.4\ \mathrm{V}$. The total wire length, resistance and capacitance per unit length of the interconnect are assumed to be $L_w = 500\ \mu\mathrm{m}$, $r_w = 1 \times 10^8\ \Omega/\mathrm{m}$ and $c_w = 1 \times 10^{-10}\ \mathrm{F/m}$, respectively. Operated at the activity factor $\alpha = 10\%$, the circuits are driven at $VDD = 0.5\ \mathrm{V}$ and $VDD = 0.4\ \mathrm{V}$ for HP CMOS and NCFET interconnects, respectively.

We first explore the optimal number of repeaters N and NMOS gate width W_n for

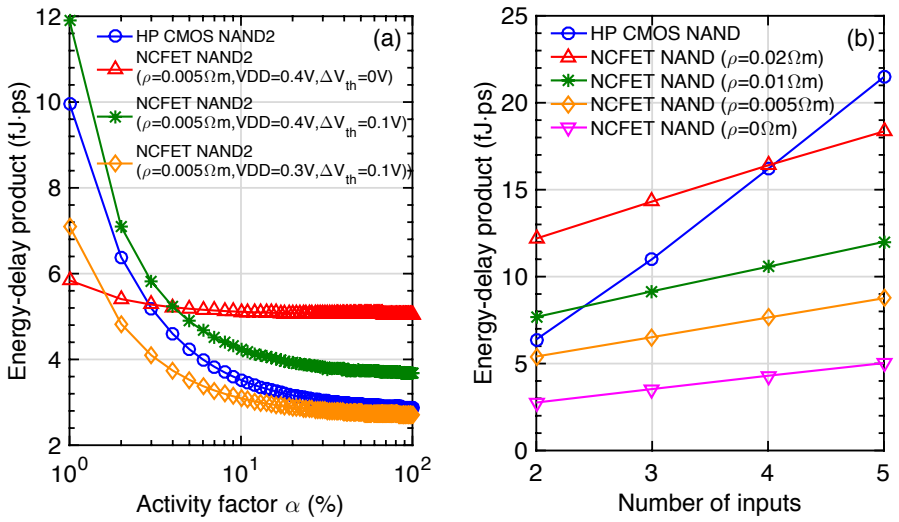

Figure 2.4: (a) The EDP trend of 2-input HP CMOS NAND and NCFET NAND at various activity factors α. ΔV_{th} represents the threshold voltage reduction for both types of transistors. (b) The EDP trend of HP CMOS NAND and NCFET NAND with different numbers of inputs at $\alpha = 2\%$. VDDs for HP CMOS NAND and NCFET NAND are 0.5 V and 0.4 V, respectively.

both HP CMOS and NCFET interconnects. Figure 2.5(a) shows the EDP surface at all combinations of N and W_n for the NCFET interconnect with $\rho = 0.01\ \Omega\mathrm{m}$. We find that the optimal number of repeaters (N^*) gradually decreases as ρ increases, as shown in Figure 2.5(b). The optimal gate width (W_n^*) does not change much with ρ. These results are consistent with the analytical models in [136]. For conventional CMOS interconnects, the minimal EDP is at $(N^*, W_n^*) = (9, 180\ \mathrm{nm})$. Figure 2.5(c) shows the EDP advantage of NCFET interconnects compared to CMOS. Optimal numbers of repeaters N^* exist for CMOS and NCFET interconnects at W_n^* to have a minimal EDP for a variety of ρ. The EDP of an NCFET interconnect can benefit from the NC effect even if the internal resistivity of the FE causes an extra delay in the circuit, as demonstrated in Figure 2.5(d). This is especially the case when sub-optimal numbers of repeaters are used to avoid too many vias and excessive via blockage. When the NCFET interconnect is operated at higher VDD (0.5 V), the EDP advantage of the NC effect is reduced with the benefit of smaller delay.

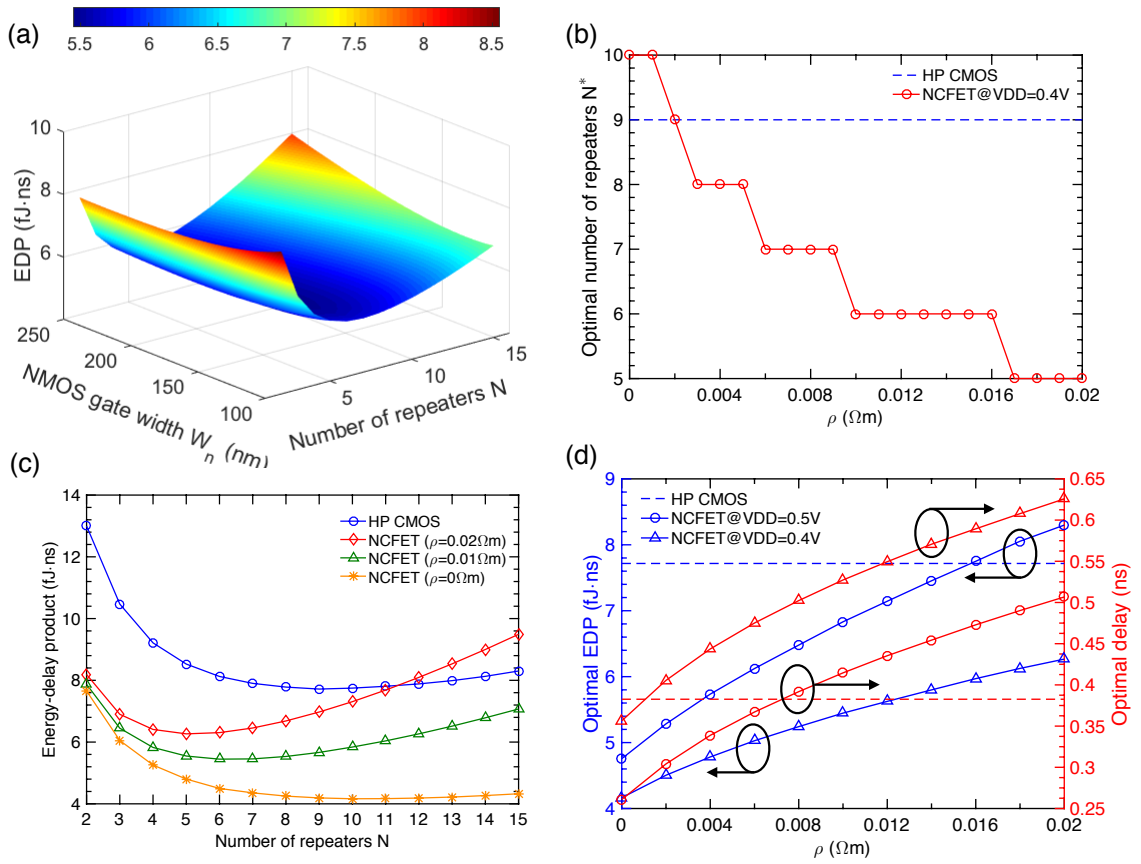

Figure 2.5: (a) Energy-delay product as a function of N and W_n for the NCFET interconnect with $\rho = 0.01\ \Omega\mathrm{m}$. The minimal EDP is at $N^* = 6$ and $W_n^* = 165\ \mathrm{nm}$. (b) Optimal number of repeaters N^* of NCFET interconnects versus internal resistivity ρ. (c) Comparison of EDP of CMOS and NCFET interconnects versus the number of repeaters for a variety of ρ at W_n^*. (d) Optimal energy-delay product (EDP^*) and propagation delay ($Delay^*$) of CMOS and NCFET interconnects. Solid lines are for NCFETs whereas HP CMOS is represented by dash lines. Circle and triangle markers denote NCFETs at $VDD = 0.5\ \mathrm{V}$ and $0.4\ \mathrm{V}$, respectively.

2.4 Summary

In summary, we present a comprehensive performance analysis of internally resistive NCFETs at the circuit level, including NANDs and repeaters in long interconnects. We discuss key aspects of NCFET characteristics that are fundamentally important for FE-based circuit designs and simulations, such as the proper circuit initialization, the negative capacitance (NC) effect on leakage currents, and the impact of the FE viscosity coefficient. To properly initialize NCFET-based circuits, the supply voltage needs to be

turned on during the simulations. Our analysis shows that the NC effect suppresses the leakage current of NCFETs when they are off. Therefore, lowering the threshold voltage of the transistors is proposed to balance the performances of NCFET-based devices at a wide range of activity factors. We also find that a large viscosity coefficient has a smaller impact on NCFET NANDs with larger fan-ins because the FE layers in various NCFETs switch in parallel. A similar trend is observed for repeaters when the RC delay of the wire is dominant compared to the switching time of FE layers. Moreover, we observe optimal numbers and sizes of repeaters that minimize the EDP, where up to 46% of EDP improvement can be achieved compared to the interconnects using conventional CMOS devices. The NCFET is implemented in SPICE, with FE dynamics described by the Landau-Khalatnikov equation. Our analysis with the SPICE circuit model provides useful insights into the effects of key NCFET parameters for advanced low-power circuit design.

CHAPTER 3
MULTI-DOMAIN PHASE FIELD FRAMEWORK

3.1 Overview

Since the discovery back in the 1920s [63], FE materials have attracted significant research attention because of (i) the possibility to switch their polarization by an externally applied voltage and (ii) spontaneous polarization under zero bias. These unique properties make ferroelectrics promising materials for emerging nanoelectronic devices. One of the most fundamental yet important applications of FE materials is in ferroelectric capacitors, which consist of an FE layer sandwiched between two conducting metal contacts. Such a device structure is believed to have many prospective applications in both high density non-volatile memories and neuromorphic computing, including FE random access memories (FeRAMs), FE tunnel junctions (FTJs), and FE field-effect transistors (FeFETs) [20, 43, 118].

In recent decades, the relentless pursuit of Moore's law comes to a bottleneck due to the fact that as the device dimensions shrink, the power density in circuits becomes a challenging concern [137]. Based on Boltzmann statistics, the minimum voltage required for conventional CMOS transistors to achieve a tenfold increase in the channel current is larger than 60 mV/decade at room temperature, as derived in Chapter 1.1.2. To overcome this thermodynamic limit, [20] proposed to stabilize the transient nature of NC by replacing the conventional gate oxide with FE materials, which in theory may lead to an internal voltage boost due to the double-well energy profile of the FE. Since then, a considerable amount of research effort has been put into a thorough understanding of both transient and stabilized NC effects [101–103, 105, 138, 139]. In particular, recently discovered doped hafnium FE materials are intensively studied due to the CMOS process

compatibility [46–48].

Transient negative capacitance was experimentally observed during polarization switching in an R-FE capacitor (RFEC) circuit [105, 138]. Such transient NC was considered to be a direct indication of the negative capacitance region during polarization switching from one state to the other. To further characterize switching dynamics of an HZO capacitor, the transient responses of the voltage across an FE (V_{FE}) layer were well measured experimentally with various pulse amplitudes in an RFEC circuit [133]. With the single domain Landau-Khalatnikov theory, the transient NC and its link to the curvature of the free energy profile are explained by the mismatched switching rates of the polarization charge and the free charge provided by the external circuit [107]. From a multi-domain perspective, physics-based phase field models highlighted the importance of spatially-distributed FE grains and domain interaction in pulse switching dynamics [114, 116, 140]. Moreover, macroscopic transient NC trends in pulse switching experiments can be described by the Preisach model and the delayed responses of FE domains [141]. Alternatively, the observed voltage drop was explained with conventional domain-mediated FE switching mechanisms based on the Kolmogorov-Avrami-Ishibashi (KAI) theory of domain nucleation and growth [88, 142].

Despite all theoretical efforts to explain the experimental measurements of FE switching kinetics, quantitative frameworks that explore the voltage-dependent dynamic responses of ferroelectrics and the physical understanding of domain interaction based on experiments are still elusive. Therefore, it is critical to establish a physics-based theoretical model that can be calibrated with experimental measurements for the purpose of studying the multi-domain nature of ferroelectrics. To elucidate how microscopic domain interaction can change the macroscopic transient NC behaviors, in this work, we adopt a three-dimensional (3D) multi-domain phase field approach that can describe measured domain switching dynamics with well-calibrated parameters. In addition, current FE circuit models in the literature are developed only in either 1 or 2 dimensional space, and the

effect of domain interaction is not considered in those models [117, 138, 143]. For the first time, we develop a physics-based circuit-compatible SPICE model that self-consistently performs 3D phase field simulations to further investigate multi-domain FE characteristics in an RFEC circuit. With this approach, we model the polarization switching under different voltage pulses and the corresponding transient NC behaviors. By analyzing the effects of domain interaction on the free energy profile, it is shown that the free energy curvature strongly depends on the applied voltage. This finding implies that the depolarization-driven charge-boost realized in an FE/DE stack [139] needs to be designed under a specific voltage or frequency. Moreover, we show that the effect of domain interaction cannot be simply viewed as local effective electric field based on the fact that the gradient free energy significantly affects the total free energy landscape. By further calibrating the transient V_{FE} with experiments, we obtain dynamic domain viscosity responses in the pulse measurements.

Overall, this chapter is organized as follows. In Sec. 3.2, a general phase field formalism is presented to describe the polarization switching dynamics of multi-domain FEs. Based on the phase field formulations described in Sec. 3.2, a circuit compatible model is developed and implemented with the SPICE simulator in Sec. 3.3. In Sec. 3.4, the simulations results demonstrate the impact of depolarization on the as-grown domain patterns, which is in agreement with the experimental findings. Furthermore, with the parameters calibrated from the measurements, our analyses reveal the effects of domain interaction on HZO switching dynamics and the free energy profile. In Sec. 3.5, we conclude this work by highlighting the multi-domain nature of HZO polarization switching and the importance of the SPICE implementation.

3.2 Theoretical Formalism

Based on Landau's phenomenological theory, the Landau-Khalatnikov (LK) equation approximately relates the FE polarization and the voltage across the FE in a single

domain manner. However, the LK equation, as a single domain approximation, does not consider other critical factors such as the domain wall interaction and elastic properties in FE capacitors. In order to capture the multi-domain nature of FE materials, we adopt a comprehensive phase field framework that takes all the energy contributions into account. Under this framework, the order parameter is a 3-dimensional polarization vector field $\mathbf{P}(\mathbf{r},t) = (P_1, P_2, P_3)$ as a function of space $\mathbf{r} = (x_1, x_2, x_3)$ and time t. The temporal evolution of $\mathbf{P}$ is described by the time-dependent Ginzburg-Landau (TDGL) equation [64–66, 80],

$$\begin{aligned}\frac{\partial P_i(\mathbf{r},t)}{\partial t} &= -L\frac{\delta F(P_i,\nabla P_i)}{\delta P_i(\mathbf{r},t)} + \eta_i(\mathbf{r},t) \\ &= -L\left[\frac{\partial(f_{\mathrm{L}} + f_{\text{elec}} + f_{\text{elas}})}{\partial P_i} - \nabla\cdot\frac{\partial f_{\mathrm{G}}}{\partial \nabla P_i}\right] + \eta_i,\ i = 1,2,3,\end{aligned} \tag{3.1}$$

where $L = 1/\rho$ is called the kinetic coefficient. The total free energy functional F includes the bulk Landau free energy f_{L}, the electric free energy f_{elec}, the elastic free energy f_{elas}, and the domain wall free energy f_{G} over the film volume V: $F(P_i,\nabla P_i) = \int f_{\mathrm{L}}(P_i) + f_{\text{elec}}(P_i) + f_{\text{elas}}(P_i) + f_{\mathrm{G}}(\nabla P_i)\,\mathrm{d}V$. $\boldsymbol{\eta}$ is the thermal fluctuation that satisfies the following conditions [144, 145],

$$\begin{aligned}&\langle \eta_i(\mathbf{r},t)\rangle = 0 \\ &\langle \eta_i(\mathbf{r},t)\eta_j(\mathbf{r}',t')\rangle = 2k_{\mathrm{B}}TL\delta_{ij}\delta(\mathbf{r}-\mathbf{r}')\delta(t-t'),\end{aligned} \tag{3.2}$$

where k_{B} is the Boltzmann constant, T is temperature, δ_{ij} is the Kronecker delta and δ is the Dirac delta function. To numerically incorporate the thermal effect, one first derives the expression for the thermal field $\mathbf{E}^{th}$:

$$\begin{aligned}\left\langle E_i^{th}(\mathbf{r},t)E_j^{th}(\mathbf{r}',t')\right\rangle &= \left\langle \frac{\eta_i(\mathbf{r},t)}{L}\frac{\eta_j(\mathbf{r}',t')}{L}\right\rangle = \frac{1}{L^2}\left\langle \eta_i(\mathbf{r},t)\eta_j(\mathbf{r}',t')\right\rangle \\ &= \frac{1}{L^2}2k_BTL\delta_{ij}\delta(\mathbf{r}-\mathbf{r}')\delta(t-t') = \frac{2k_BT}{L}\delta_{ij}\delta(\mathbf{r}-\mathbf{r}')\delta(t-t').\end{aligned} \tag{3.3}$$

In the numerical simulation, $\mathbf{E}_{th}$ is related with a standard Wiener process $W(\mathbf{r},t)$. W is independent of spatial positions and time points, and has Gaussian increments; thus,

$$\begin{aligned} \mathrm{d}W(\mathbf{r},t) &= \mathrm{d}W(\mathbf{r})\,\mathrm{d}W(t) = [W(\mathbf{r}+\mathrm{d}\mathbf{r}) - W(\mathbf{r})][W(t+\mathrm{d}t) - W(t)] \\ &= \sqrt{\mathrm{d}V}\sqrt{\mathrm{d}t}\mathcal{N}(0,1), \end{aligned} \tag{3.4}$$

where $\mathcal{N}(0,1)$ represents the standard normal distribution with zero mean and unit variance, and $\mathrm{d}V$ and $\mathrm{d}t$ are the numerical unit cell volume and time step, respectively. Accordingly, the thermal field can be derived as follows,

$$\begin{aligned} &E_i^{th}(\mathbf{r},t)\,\mathrm{d}V\,\mathrm{d}t = \nu\,\mathrm{d}W(\mathbf{r},t) = \nu\sqrt{\mathrm{d}V}\sqrt{\mathrm{d}t}\mathcal{N}(0,1) = \sqrt{\frac{2k_{\mathrm{B}}T}{L}}\sqrt{\mathrm{d}V}\sqrt{\mathrm{d}t}\mathcal{N}(0,1) \\ &\Rightarrow \boxed{E_i^{th}(\mathbf{r},t) = \sqrt{\frac{2k_{\mathrm{B}}T}{L\,\mathrm{d}V\,\mathrm{d}t}}\mathcal{N}(0,1),} \end{aligned} \tag{3.5}$$

where $\nu = \sqrt{\frac{2k_{\mathrm{B}}T}{L}}$ is the standard deviation of the random thermal field.

The Landau free energy density can be expanded as

$$\begin{aligned} f_{\mathrm{L}} = {} & \alpha_1\big(P_1^2+P_2^2+P_3^2\big) + \alpha_{11}\big(P_1^4+P_2^4+P_3^4\big) + \alpha_{12}\big(P_1^2P_2^2+P_2^2P_3^2+P_1^2P_3^2\big) \\ & + \alpha_{111}\big(P_1^6+P_2^6+P_3^6\big) + \alpha_{112}\big[P_1^4\big(P_2^2+P_3^2\big) + P_2^4\big(P_1^2+P_3^2\big) + P_3^4\big(P_1^2+P_2^2\big)\big] \\ & + \alpha_{123}\big(P_1^2P_2^2P_3^2\big), \end{aligned} \tag{3.6}$$

where $\{\alpha_i\}$, $\{\alpha_{ij}\}$ and $\{\alpha_{ijk}\}$ are Landau expansion coefficients [144, 146]. In FE tetragonal phase, $\alpha_1 < 0$ and $\mathbf{P} \approx (0,0,P)$, with P aligned in the out-of-plane direction.

The domain wall energy results from the gradients of the polarization fields and thus

can be expressed as

$$\begin{aligned} f_{\mathrm{G}}(P_{i,j}) =& \frac{1}{2}G_{11}\left(P_{1,1}^2 + P_{2,2}^2 + P_{3,3}^2\right) \\ &+ \frac{1}{2}G_{44}\left[2P_{1,2}^2 + 2P_{2,1}^2 + 2P_{2,3}^2 + 2P_{3,2}^2 + 2P_{1,3}^2 + 2P_{3,1}^2\right] \\ =& \frac{1}{2}G_{11}\left(P_{1,1}^2 + P_{2,2}^2 + P_{3,3}^2 + P_{1,2}^2 + P_{2,1}^2 + P_{2,3}^2 + P_{3,2}^2 + P_{1,3}^2 + P_{3,1}^2\right), \end{aligned} \tag{3.7}$$

where $P_{i,j} = \frac{\partial P_i}{\partial x_j}$ is the spatial derivative of $\mathbf{P}$, $\{G_{ij}\}$ are the gradient coefficients, and the second equality comes from $G_{44} = G_{11}/2$ [80, 147, 148]. Hence, the polarization gradient term in Eq. 3.1 can be simplified as

$$\begin{aligned} \nabla \cdot \frac{\partial f_{\mathrm{G}}}{\partial \nabla P_i} &= \left(\frac{\partial}{\partial x_1}, \frac{\partial}{\partial x_2}, \frac{\partial}{\partial x_3}\right) \cdot \left(\frac{\partial f_{\mathrm{G}}}{\partial P_{i,1}}, \frac{\partial f_{\mathrm{G}}}{\partial P_{i,2}}, \frac{\partial f_{\mathrm{G}}}{\partial P_{i,3}}\right) \\ &= \frac{\partial}{\partial x_1}\left(\frac{\partial f_{\mathrm{G}}}{\partial P_{i,1}}\right) + \frac{\partial}{\partial x_2}\left(\frac{\partial f_{\mathrm{G}}}{\partial P_{i,2}}\right) + \frac{\partial}{\partial x_3}\left(\frac{\partial f_{\mathrm{G}}}{\partial P_{i,3}}\right) \\ &= G_{11}(P_{i,11} + P_{i,22} + P_{i,33}) = G_{11}\nabla^2 P_i. \end{aligned} \tag{3.8}$$

Therefore, plugging Eq. 3.8 into Eq. 3.1 yields

$$\boxed{\frac{\partial P_i(\mathbf{r}, t)}{\partial t} = -L\frac{\partial(f_{\mathrm{L}} + f_{\text{elec}} + f_{\text{elas}})}{\partial P_i} + LG_{11}\nabla^2 P_i + \eta_i,\ i = 1, 2, 3.} \tag{3.9}$$

The electric energy density can be calculated given the electric field and polarization [149],

$$f_{\text{elec}} = -\frac{1}{2}E_i(\epsilon_0 \kappa E_i + P_i), \tag{3.10}$$

where ϵ_0 is the vacuum permittivity, $\mathbf{E}$ is the total electric field in the FE, κ is the background dielectric constant that accounts for non-ferroelectric switching charges, and $\mathbf{P}$ is the ferroelectric-contributed polarization that can be obtained from the TDGL equation [70, 150]. The electric displacement field $D_i = \epsilon_0 \kappa E_i + P_i$ satisfies the electrostatic equation $D_{i,i} = 0$ if there are no space charges inside the film [149]. By

replacing $\mathbf{E}$ with the potential gradient $-\nabla\phi$, we obtain the Poisson's equation,

$$\epsilon_0\kappa(\phi_{,11} + \phi_{,22} + \phi_{,33}) = (P_{1,1} + P_{2,2} + P_{3,3}), \tag{3.11}$$

which is subject to the out-of-plane boundary conditions (BCs):

$$\begin{aligned} \phi(z = 0) &= V_{\text{FE}}, \\ \phi(z = t_{\text{FE}}) &= 0. \end{aligned} \tag{3.12}$$

Note that the in-plane boundary conditions are assumed to be periodic due to the fact that metal contacts are patterned on a continuous FE thin film in experiments. The electric field obtained this way is the total field inside the FE film, and the difference between the applied field and total field is the depolarization field, which results from the incomplete charge compensation at the film surfaces. The Poisson's equation 3.11 can be solved with the Fourier transform method in order to reduce the computational cost. By taking Fourier transform of both sides of Eq. 3.11, one obtains

$$\begin{aligned} &-(k_x^2 + k_y^2 + k_z^2)\hat{\phi} = \frac{1}{\epsilon}\mathcal{F}\{P_{1,1} + P_{2,2} + P_{3,3}\} \\ &\Rightarrow \hat{\phi} = \frac{-1}{\epsilon k^2}\mathcal{F}\{P_{1,1} + P_{2,2} + P_{3,3}\} \\ &\Rightarrow \phi = \mathcal{F}^{-1}\left\{\hat{\phi}\right\};\ \mathbf{E}_{\text{FE}} = -\nabla\phi, \end{aligned} \tag{3.13}$$

where $\mathbf{k} = (k_x, k_y, k_z)$ is the wave vector in three-dimensional space, $k = |\mathbf{k}|$, $\epsilon = \epsilon_0\kappa$, and $\hat{\phi}$ is the Fourier transform of the potential ϕ. Part of the source code for the Fourier-spectral method implemented with MATLAB® can be found in Appendix A.

The change in crystal structures from cubic to tetragonal phases generates polarization $\mathbf{P}$, and the corresponding spontaneous strain ϵ_{ij}^0 is defined under the stress-free

condition [144]. The stress-free condition is given by the thermodynamic relation:

$$\sigma_{ij} = \frac{\partial f_{\text{elas}}}{\partial \epsilon_{ij}} = 0, \tag{3.14}$$

where σ_{ij} is the stress field and ϵ_{ij} is the total strain of the crystal compared to the parent paraelectric phase. Therefore, ϵ^0_{ij} can be calculated as follows,

$$\begin{aligned}
&\epsilon^0_{11} = Q_{11}P_1^2 + Q_{12}\big(P_2^2 + P_3^2\big),\ \epsilon^0_{13} = Q_{44}P_1P_3,\\
&\epsilon^0_{22} = Q_{11}P_2^2 + Q_{12}\big(P_3^2 + P_1^2\big),\ \epsilon^0_{23} = Q_{44}P_2P_3,\\
&\epsilon^0_{33} = Q_{11}P_3^2 + Q_{12}\big(P_1^2 + P_2^2\big),\ \epsilon^0_{12} = Q_{44}P_1P_2,
\end{aligned} \tag{3.15}$$

where $\{Q_{ij}\}$ are the electrostrictive coefficients. The elastic energy can be calculated with the expression [147, 148]

$$f_{\text{elas}} = \frac{1}{2}c_{ijkl}e_{ij}e_{kl}, \tag{3.16}$$

where c_{ijkl} is a fourth-rank stiffness tensor. For isotropic materials, c_{ijkl} can be written as

$$C = \begin{pmatrix}
c_{11} & c_{12} & c_{12} & & & \\
c_{12} & c_{11} & c_{12} & & \mathbf{0} & \\
c_{12} & c_{12} & c_{11} & & & \\
 & & & c_{44} & 0 & 0 \\
 & \mathbf{0} & & 0 & c_{44} & 0 \\
 & & & 0 & 0 & c_{44}
\end{pmatrix}, \tag{3.17}$$

which contains three nonzero elements, c_{11}, c_{12} and c_{44}. The elastic energy density can

then be simplified as

$$\begin{aligned} f_{\text{elas}} =& \frac{1}{2} c_{11}\left(e_{11}^2 + e_{22}^2 + e_{33}^2\right) \\ &+ c_{12}(e_{11}e_{22} + e_{22}e_{33} + e_{11}e_{33}) \\ &+ 2c_{44}\left(e_{12}^2 + e_{23}^2 + e_{13}^2\right). \end{aligned} \tag{3.18}$$

The relation between the elastic strain e_{ij} and the total strain ϵ_{ij} is $e_{ij} = \epsilon_{ij} - \epsilon_{ij}^0$. The in-plane strains ϵ_{11} and ϵ_{22} are equal to the film-substrate lattice misfit strain μ_{m}, and ϵ_{12} is assumed to be 0. The out-of-plane components ϵ_{i3} can be obtained with the equation $c_{i3kl}\epsilon_{kl} = 0$ [148]. Therefore, ϵ_{13} and ϵ_{23} are 0, and $\epsilon_{33} = -c_{12}(2\mu_{\text{m}})/c_{11}$.

With all the energy contributions included, the governing TDGL equation can be numerically solved by semi-implicit Fourier-spectral method with periodic BCs in the in-plane directions and zero BCs in the out-of-plane direction [151].

3.3 Circuit-compatible SPICE Implementation

In this section, we develop equivalent circuits of the TDGL equation and Poisson's equation so as to solve for the polarization and potential distributions self-consistently with the SPICE simulator.

3.3.1 TDGL equation

The mathematical form of (3.1) is similar to the voltage-current relationship of a unit capacitor $(C = 1)$ [152]. In other words,

$$\frac{\mathrm{d}V(P_i)}{\mathrm{d}t} = I(V(P_1), V(P_2), V(P_3), V_{FE}) \Leftrightarrow C\frac{\mathrm{d}V}{\mathrm{d}t} = I, \tag{3.19}$$

where $V(P_i),\ i = 1, 2, 3$ is the voltage representation of the polarization in the SPICE simulator, and I is a voltage-controlled current source as a function of polarization and FE voltage. It is noteworthy that the gradient energy contributions on the right hand side of

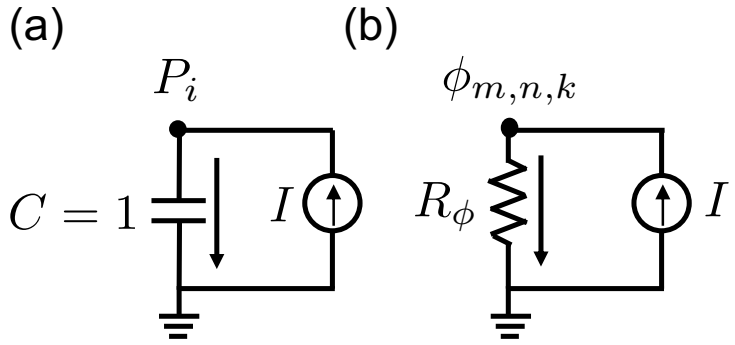

Figure 3.1: The SPICE equivalent circuit diagrams of (a) the TDGL equation, where $i = 1, 2, 3$ and (b) the Poisson's equation.

(3.1) can be simplified as

$$\begin{aligned}\nabla \cdot \frac{\partial f_{\mathrm{G}}}{\partial \nabla P_i} &= \left(\frac{\partial}{\partial x}, \frac{\partial}{\partial y}, \frac{\partial}{\partial z}\right) \cdot \left(\frac{\partial f_{\mathrm{G}}}{\partial P_{i,1}}, \frac{\partial f_{\mathrm{G}}}{\partial P_{i,2}}, \frac{\partial f_{\mathrm{G}}}{\partial P_{i,3}}\right) \\ &= \frac{\partial}{\partial x}\left(\frac{\partial f_{\mathrm{G}}}{\partial P_{i,1}}\right) + \frac{\partial}{\partial y}\left(\frac{\partial f_{\mathrm{G}}}{\partial P_{i,2}}\right) + \frac{\partial}{\partial z}\left(\frac{\partial f_{\mathrm{G}}}{\partial P_{i,3}}\right) \\ &= G_{11}(P_{i,11} + P_{i,22} + P_{i,33}) = G_{11}\nabla^2 P_i.\end{aligned} \tag{3.20}$$

With the finite difference discretization, the Laplacian of a variable can be expressed as

$$\begin{aligned}\nabla^2 P_i = &\frac{P_i(m+1,n,k) + P_i(m-1,n,k) - 2P_i(m,n,k)}{dx^2} \\ &+ \frac{P_i(m,n+1,k) + P_i(m,n-1,k) - 2P_i(m,n,k)}{dy^2} \\ &+ \frac{P_i(m,n,k+1) + P_i(m,n,k-1) - 2P_i(m,n,k)}{dz^2},\end{aligned} \tag{3.21}$$

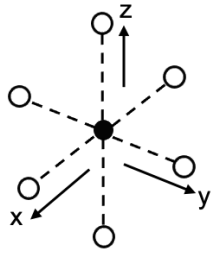

Figure 3.2: Finite difference coordinates

where $\{dx, dy, dz\}$ are the numerical grid spacing and $\{m, n, k\}$ are discrete indices in each dimension.

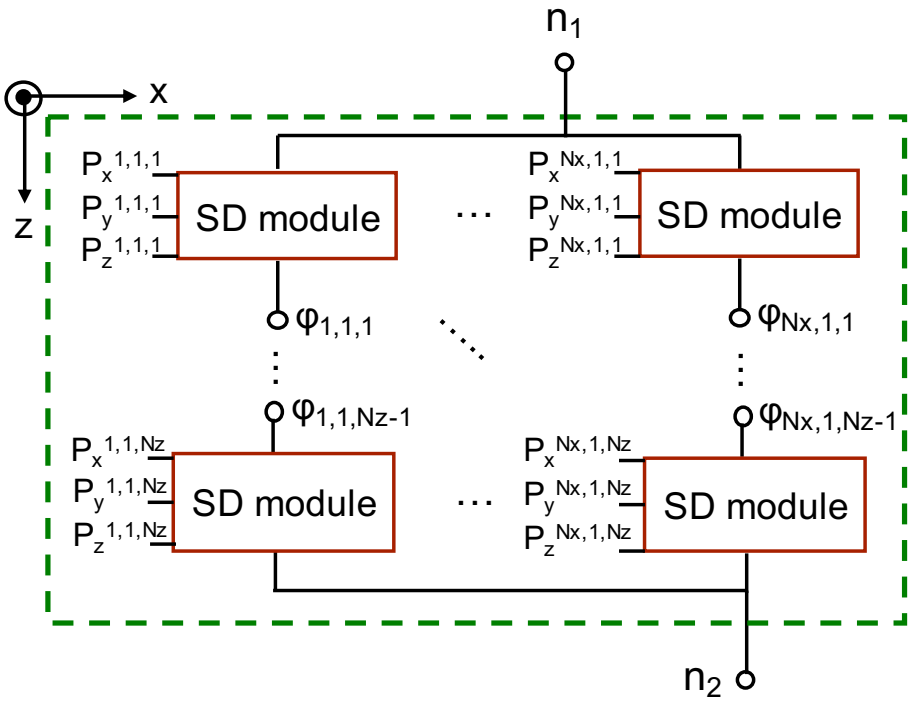

Figure 3.3: The SPICE implementation of a multi-domain FE thin film with single domain (SD) circuit modules connected in the 3D space, where $\varphi_{x,y,z}$ is the potential at each voltage node and $\{n_1, n_2\}$ are the two terminals of the FE capacitor.

3.3.2 Poisson's equation

To obtain the multi-domain potential profile and the corresponding local electric field, we discretize (3.11) as

$$\begin{aligned}\nabla^2\phi =& \frac{\phi_{m+1,n,k} + \phi_{m-1,n,k} - 2\phi_{m,n,k}}{dx^2} \\ &+ \frac{\phi_{m,n+1,k} + \phi_{m,n-1,k} - 2\phi_{m,n,k}}{dy^2} \\ &+ \frac{\phi_{m,n,k+1} + \phi_{m,n,k-1} - 2\phi_{m,n,k}}{dz^2} = g(\mathbf{P}),\end{aligned} \tag{3.22}$$

where $g(\mathbf{P}) = (P_{1,1} + P_{2,2} + P_{3,3})/(\epsilon_0\kappa)$. By rearranging (3.22), one obtains

$$\begin{aligned}\frac{\phi_{m,n,k}}{R_\phi} &= -g(\mathbf{P}) + \frac{\phi_{m+1,n,k} + \phi_{m-1,n,k}}{dx^2} \\ &\quad + \frac{\phi_{m,n+1,k} + \phi_{m,n-1,k}}{dy^2} + \frac{\phi_{m,n,k+1} + \phi_{m,n,k-1}}{dz^2} \\ &= I(\mathbf{P}, \phi_{nn}),\end{aligned} \tag{3.23}$$

where $R_\phi = 1/(2/dx^2 + 2/dy^2 + 2/dz^2)$ and ϕ_{nn} represents the potentials of the nearest neighboring cells. Equation (3.23) can be viewed as the voltage-current relationship of a constant resistor R_ϕ with the right hand side being a voltage-controlled current source.

If the finite screening lengths of the metal contacts are considered, the potential boundary conditions will depend on the out-of-plane polarization as follows in order to account for the depolarization effect [45]:

$$\begin{aligned}V(z = 0) &= V_{\text{FE}} - \frac{\sigma_s \lambda_1}{\epsilon_1 \epsilon_0} \\ V(z = t_{\text{FE}}) &= 0 + \frac{\sigma_s \lambda_2}{\epsilon_2 \epsilon_0},\end{aligned} \tag{3.24}$$

where $\sigma_s = \frac{P_z t_{\text{FE}}}{t_{\text{FE}} + \lambda_1/\epsilon_1 + \lambda_2/\epsilon_2}$ is the screening charge density due to out-of-plane polarization, and $\lambda_{1,2}$ and $\epsilon_{1,2}$ are the screening lengths and relative dielectric constants of contacts $\{1,2\}$, respectively. The equivalent circuit diagrams of (3.1) and (3.11) are summarized in Fig. 3.1. Note that it is important to distinguish the total free charge density and polarization in an RFEC circuit [107]. In Fig. 3.4, the current flowing through the FE capacitor I_R can be calculated as

$$I_R = \frac{\mathrm{d}Q_{\text{FE}}}{\mathrm{d}t} = \frac{\mathrm{d}}{\mathrm{d}t}\left(\epsilon_0\kappa\frac{V_{\text{FE}}}{t_{\text{FE}}} + P_z\right)A, \tag{3.25}$$

where Q_{FE} is the total free charge, A is the capacitor cross-sectional area and P_z is the average polarization in the out-of-plane direction. Note that it is more convenient to implement the contact module with Verilog-A based on (3.25). It is noteworthy that the measured charge is the total free charge Q_{FE} instead of polarization charge according to

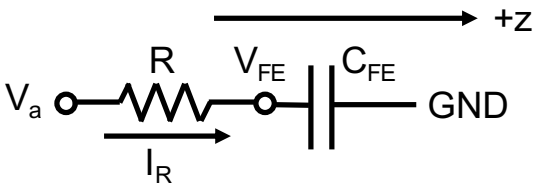

Figure 3.4: The RFEC circuit diagram used in [133] and this work.

(3.25).

3.4 Results and Discussion

Based on the phase field formalism, we solve the TDGL equation (3.1) and Poisson's equation (3.11) for polarization charge and potential distributions to investigate the pulse switching dynamics of multi-domain HZO capacitors in an RFEC circuit. In this work, the baseline experimental measurements are extracted from [133], which demonstrated the transient responses of a TiN/$Hf_{0.7}Zr_{0.3}O_2$/TiN capacitor under various pulse amplitudes. The parameters used in this work are summarized in Table 4.1.

3.4.1 SPICE model initialization and validation

In our simulations, the FE film is discretized into $10 \times 10 \times 10$ rectangular cells with the grid size being $1\,\mathrm{nm}$ in each dimension. For further analyses, we first obtain the steady state multi-domain polarization distributions and potential profile under zero bias with polarization initialized with a zero-mean normal distribution. A negative voltage pulse is applied to the steady-state domain state to obtain the initial conditions for the pulse measurements.

To validate the numerical accuracy of the proposed SPICE model, we also solve the TDGL equation (3.1) and Poisson's equation (3.11) in MATLAB® using the semi-implicit Fourier-spectral method [151]. Fig. 3.5 shows the simulated transient responses from the SPICE simulator compared to those from the Fourier-spectral method with the same numerical settings and boundary conditions. For simplicity, the parasitic capacitance

Table 3.1: Parameters Used For HZO in This Work

Parameter	Value
$(\lambda/\epsilon)_{1,2}$ (Å)	0.06, 0.06
κ	35
t_{FE} (nm)	10 [133]
α_1 (m/F)	-4×10^8 [107]
α_{11} ($\text{m}^5\text{C}^{-2}/\text{F}$)	3.7×10^9 [107]
α_{111} ($\text{m}^9\text{C}^{-4}/\text{F}$)	1.1×10^9 [107]
G_{11} (m^3/F)	*dynamic*
L $(\Omega\text{m})^{-1}$	2×10^{-4} or *dynamic*
R (Ω)	20k [133]
Area (m^2)	7×10^{-9} [133]

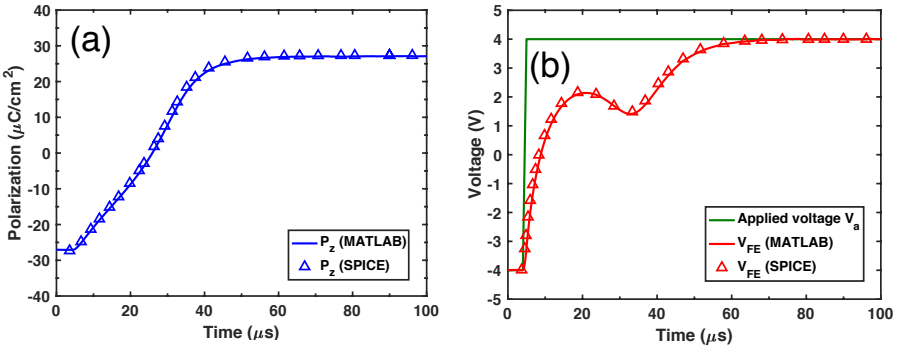

Figure 3.5: The comparisons between the semi-implicit Fourier-spectral method and SPICE circuit simulations of (a) P_{z} and (b) V_{FE} with $G_{11} = 1 \times 10^{-9}\,(\text{m}^3/\text{F})$ at a pulse amplitude of $4\,\text{V}$.

parallel to the FE capacitor is assumed to be small enough to be ignored in the RFEC circuit [138]. In addition to the advantage of circuit compatibility, the proposed SPICE model for one FE capacitor is also more than twice faster than the MATLAB® implementation as long as the parameters do not have time/spatial variations. Nevertheless, further optimizations for the model to be compact are still needed to simulate real logic and memory circuits once more complex switching mechanisms such as grain distributions are considered.

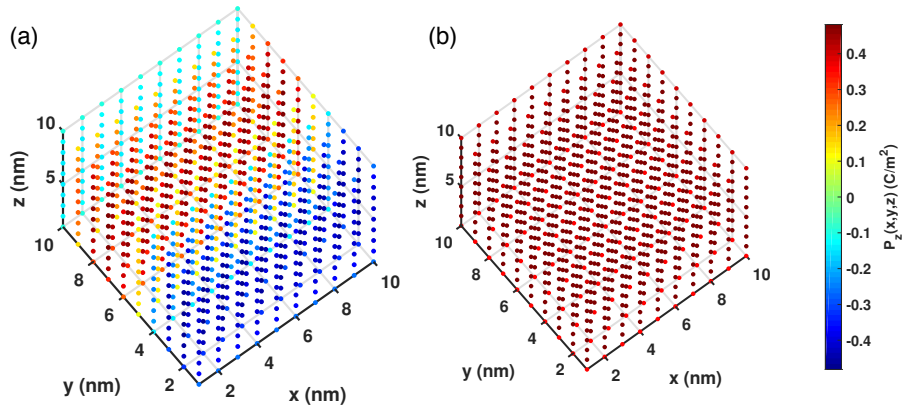

Figure 3.6: The domain structures of PTO (a) with and (b) without the depolarization field. The depolarization effect is controlled by contact screening lengths $\lambda_{1,2} = 0.73, 0.8$ Å for (a) and $\lambda_{1,2} = 0, 0$ Å for (b). All the other phase field parameters are taken from [67, 148].

3.4.2 Domain structures

For the FE domain structure simulation, we consider a metal-FE-metal (MFM) heterostructure grown epitaxially on a cubic substrate. When the device is cooled down to room temperature, the FE film undergoes a cubic to tetragonal phase transition. The spatial distributions of polarization vector field describe the ferroelectric domain pattern. Based on the experimental observations, the stripe domain period is comparable to the film thickness [33, 153, 154]. Hence, we choose one cube with edges equal to film thickness as the domain of interest in our simulation for simplicity. The simulation starts from normally distributed $\mathbf{P}$ with zero mean and standard deviation of 0.005. Fig. 3.6 shows the equilibrium domain structures of PTO under zero voltage with and without the depolarization field. The film with larger contact screening lengths tends to form stripe patterns because the overall polarization is reduced by a larger depolarization field. On the other hand, the film without the depolarization field ends up in mono-domain states, and thus the polarization is enhanced. Such depolarization effect on the domain structures is consistent with both experimental and simulation conclusions [33, 149, 153]. The

successful prediction of domain patterns allows us to extend this framework to the study of polarization switching mechanisms, including pulse switching and hysteresis dynamics.

3.4.3 Effects of G_{11} on the transient responses

From the experimental measurements in [133], the charge in the steady state is found to be suppressed at smaller pulse amplitudes. With our model, we find that the measured saturation free charges at various pulse amplitudes do not match those predicted by the phase field approach with a constant G_{11}. As a result, we propose that the gradient coefficient G_{11} (and hence domain interaction) depends on the applied voltage. To verify this argument, we first examine how G_{11} affects the transient behaviors at a pulse amplitude of $4\,\mathrm{V}$. In Fig. 3.7(a), the saturation charge decreases significantly as G_{11} increases, which indicates that stronger domain interaction tends to suppress polarization switching. Moreover, the experimental measurements in [133] also show that the transient voltage drop disappears as the pulse voltage decreases. This finding is also captured by increasing G_{11}. As shown in Fig. 3.7(b), V_{FE} dynamics acts like a normal dielectric capacitor and the voltage drop is no longer to be seen as domain interaction gets stronger (or larger G_{11}). Next, we extract the G_{11} value for each pulse amplitude based on the saturation total free charge measured in [133]. Fig. 3.9(a) shows the extracted G_{11} at each pulse amplitude based on the experimentally measured FE free charge in the steady state. With extracted G_{11}, Fig. 3.7(c) and (d) show the transient responses of Q_{FE} and V_{FE} at various pulse amplitudes, which are qualitatively consistent with the experimental observations. Therefore, these simulation results imply that domain interaction of the HZO thin film is weaker under a larger voltage, which may be attributed to the breaking of spatial domain coupling under a large electric field. It is also noteworthy that in this framework, we find that the effect of G_{11} is mainly on the average polarization rather than the spatial variations because of the relatively uniform initial domain state. In reality, the polarization spatial variations would be induced by the inevitable defects inside the FE films, which play an important role in the domain wall

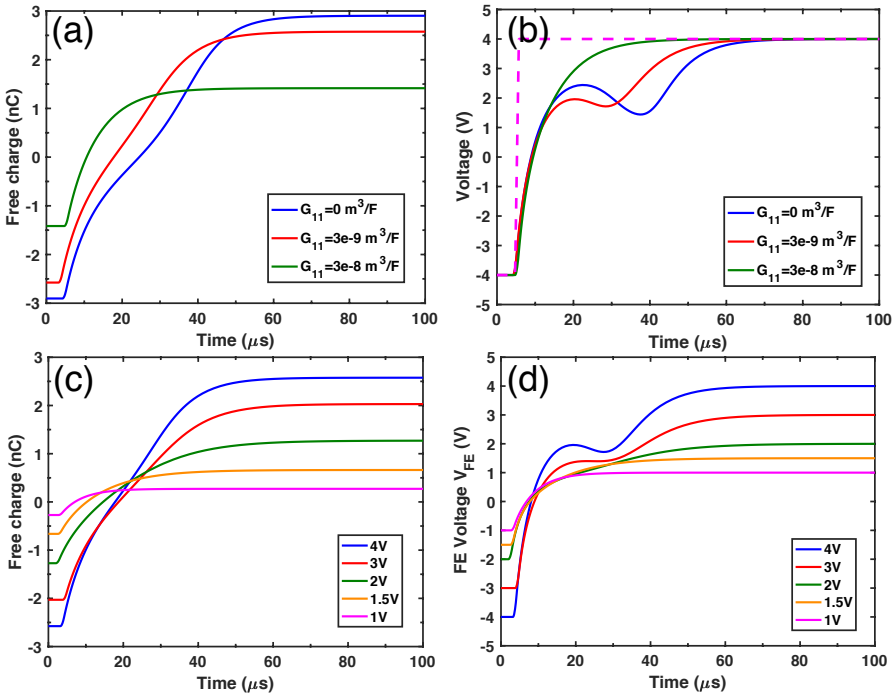

Figure 3.7: The SPICE simulations of (a) charge switching dynamics and (b) V_{FE} transient responses with various G_{11} values under a voltage pulse of $4\,\text{V}$ (dashed line). (c) and (d) show transient responses of Q_{FE} and V_{FE} with G_{11} correction under various pulse amplitudes.

boundaries and thus polarization switching behaviors [155]. Therefore, further theoretical studies of domain interaction mechanisms may rely on more experimental investigations of domain formation and domain wall characteristics of Zr-doped HfO_2 thin films.

3.4.4 Effects of G_{11} on the free energy curvature

Now that we have shown G_{11} is dependent on the applied voltage, we investigate the effects of domain interaction on the transient response in terms of the free energy dynamics. Fig. 3.8(a)–(c) show the free energy dynamics when polarization switches from the negative state to the positive state under a pulse of $4\,\text{V}$ with increasing G_{11}. Without domain interaction ($G_{11} = 0\,\text{m}^3/\text{F}$), the bulk free energy exhibits a negative capacitance region (negative curvature) during polarization switching. With a nonzero G_{11}, the gradient free energy due to FE domain interaction shows a quadratic shape, and thus turns the negative curvature of the bulk free energy into a positive one as G_{11} increases. Note

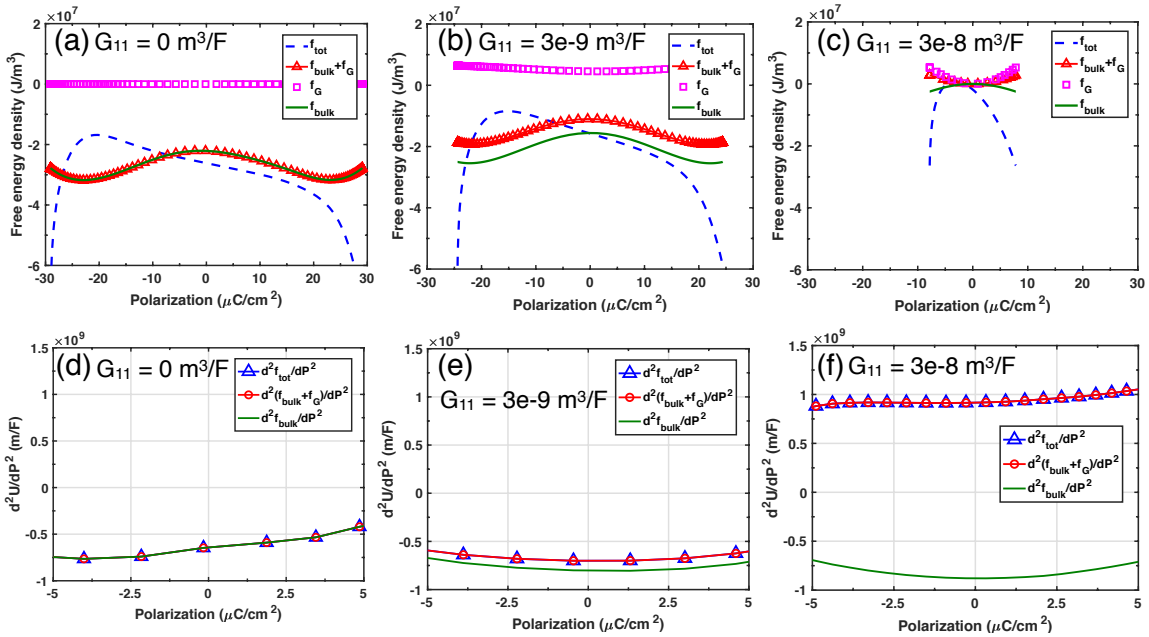

Figure 3.8: Top row: Free energy density versus polarization as polarization is switched from $-30\,\mu\mathrm{C/cm^2}$ to $+30\,\mu\mathrm{C/cm^2}$ at various G_{11} values. Bottom Row: The second derivative of free energy with respect to polarization versus polarization as polarization is switched from $-30\,\mu\mathrm{C/cm^2}$ to $+30\,\mu\mathrm{C/cm^2}$ (because of the interest in the curvatures of the curves in the top row around $P = 0\,\mu\mathrm{C/cm^2}$, the bottom plots show the polarization range of $-5\,\mu\mathrm{C/cm^2}$ to $+5\,\mu\mathrm{C/cm^2}$). The total free energy ($f_{\mathrm{tot}} = f_{\mathrm{bulk}} + f_{\mathrm{G}} + f_{\mathrm{elec}}$) is initially increased by the applied electric field to overcome the energy barrier and then drops as the polarization switches to the positive stable state, as shown in the blue dashed lines in (a), (b) and (c).

that the extracted gradient free energy as a function of polarization is consistent with the parabolic shape obtained from the first-principles calculations [156]. The corresponding free energy curvatures $\left(\frac{\partial^2 U}{\partial P_z^2}\right)$ near zero polarization are plotted in Fig. 3.8(d)–(f). The positive curvature of the total free energy with a larger G_{11} explains how stronger domain interaction can suppress the transient NC. Since G_{11} is voltage-dependent, the energy profile at various voltages depends on how FE domains interact.

The voltage-dependence of the free energy curvature implies that FE capacitance can only be matched with a constant DE capacitance for charge-boost at a specific voltage based on the fact that the total free energy curvature is directly related to the FE capacitance [105, 107]. Moreover, in Fig. 3.7(c) and (d), we use a constant G_{11} to simulate the switching

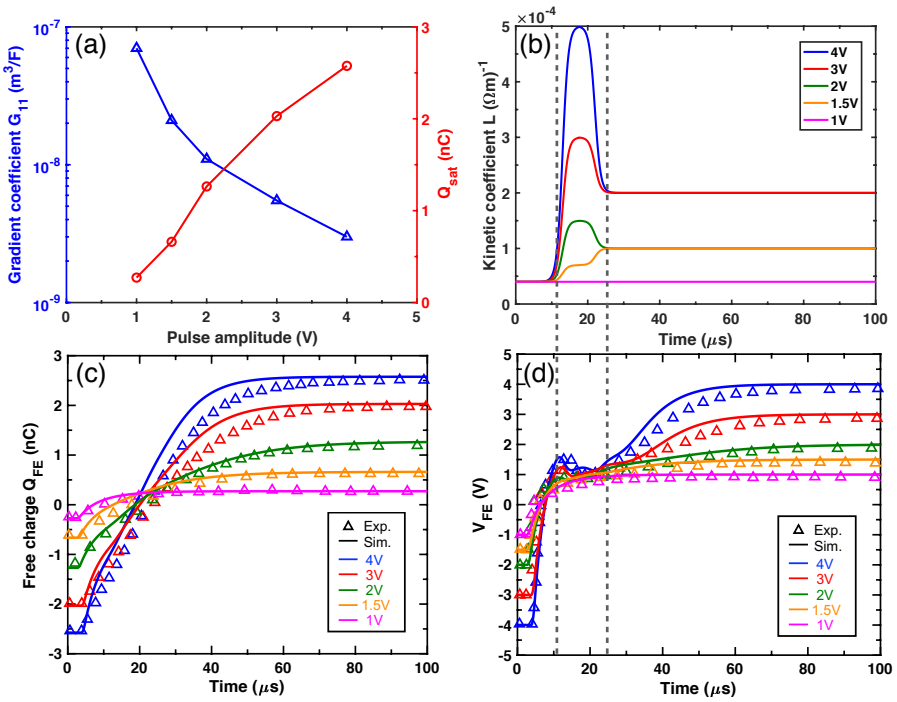

Figure 3.9: (a) The extracted G_{11} values and the corresponding saturation free charge Q_{sat} at various pulse amplitudes according to the experimental measurements in [133]. (b) Kinetic coefficient dynamics during polarization switching at various pulse amplitudes. (c) The SPICE simulations of free charge switching dynamics at various pulse amplitudes compared with experiments in [133]. (d) The SPICE simulations of V_{FE} transient responses at various pulse amplitudes compared with experiments in [133].

dynamics at a given applied pulse due to the short rise time of the pulse. In reality, G_{11} varies when the applied voltage switches from low to high. This indicates that the frequency of the applied pulse affects the FE-DE capacitance matching as well.

Note that the electric free energy has a mathematical form as in (3.10) and therefore does not affect the energy curvature, as can be seen in Fig. 3.8(d)–(f), which demonstrate that $\frac{\mathrm{d}^2 f_{\text{tot}}}{\mathrm{d}P_z^2} = \frac{\mathrm{d}^2 (f_{\text{bulk}} + f_{\text{G}})}{\mathrm{d}P_z^2}$ (or equivalently, $\frac{\mathrm{d}^2 f_{\text{elec}}}{\mathrm{d}P_z^2} = 0$). As a result, our simulations also show that the gradient energy contribution $G_{11}\nabla^2 P_i$ cannot be simply treated as an effective interaction electric field because the existence of gradient free energy changes the curvature of the total free energy landscape [140].

3.4.5 Dynamic kinetic coefficient

With extracted G_{11} and a constant kinetic coefficient L, the measured saturation polarization can be well captured by the phase field framework. However, the voltage responses during the transient NC are not consistent with experiments. Therefore, we adopt a dynamic L to further characterize the domain viscosity variations during polarization switching. Fig. 3.9(b) shows the transient kinetic coefficient L at various pulse amplitudes. When V_{FE} is below the coercive voltage, the constant L represents the inherent dielectric response. The larger L in the time interval between the gray dashed lines indicates that the polarization switching speeds up due to the unstable nature of the NC region. As the FE capacitance goes back to a positive value, L decreases and the transient V_{FE} recovers to a normal dielectric response. For smaller pulse amplitudes, the energy curvature is positive during polarization switching due to stronger domain interaction. Therefore, the transient responses of the FE are similar to DE responses without a voltage drop. Compared with measurements in [133], the simulation results of total free charge Q_{FE} and FE voltage V_{FE} with various pulse amplitudes are shown in Fig. 3.9(c)–(d). Note that the time interval where L increases may depend on the external circuit components because the increase in L indicates the occurrence of polarization reversal.

Although our simulations show reasonable trends of the measured transient responses, there are some discrepancies between the simulations and experiments, which may result from the elastic free energy. Because HZO materials are not classical perovskites, the crystal structures and the related elastic contributions to the total free energy need further experimental investigations, which is beyond the scope of this thesis. Further simulations that include broad distributions of bulk Landau parameters show an insignificant impact on the transient responses and confirm the dominant effects of the gradient coefficient (see Sec. 3.4.7 for details). However, the gradient and kinetic coefficients may also have spatial distributions due to the multi-domain nature of HZO [116, 138].

3.4.6 Comparison with the Preisach-based approach

In a previous work [141], a Preisach model combined with the delayed responses of FE domains was used to describe the macroscopic transient NC trends in pulse switching experiments. Such a Preisach-based approach simulates the polarization switching with the assumption that each domain cell has a different switching threshold voltage and responds instantaneously. The FE switching delay is modeled using Merz's law, which states that FE polarization switching has a characteristic time depending on the activation field and the applied field [157]. Based on Merz's law, when the external field is larger than the activation field of the domain cell, the delay time constant decreases exponentially. The smaller delay under a larger external field is qualitatively consistent with the increasing kinetic coefficient as the pulse amplitude increases, as shown in Fig. 3.9(b).

The advantage of the Preisach-based approach as a circuit-compatible model is that it well captures ferroelectric switching characteristics in a more computation efficient manner. However, for ultra-scaled devices that contain few grains, the Preisach-based approach may not be suitable because it is based on the parameter distribution of a large domain ensemble [82, 158]. Moreover, the Preisach model approximates the ferroelectric switching dynamics well when the domains only have up and down orientations [159]. In this work, we choose a phenomenological approach for a deeper understanding of microscopic switching mechanisms from the perspective of the thermodynamic free energy. In contrast to the Preisach-based approach, such a thermodynamic phase-field model is not only effective in incorporating free energy contributions but also useful for the studies of domain structures and the ferroelectric-paraelectric phase transitions. In addition, the proposed way of solving TDGL and Poisson's equation in the SPICE simulator can be applied to other physics-based partial differential equations of a similar form.

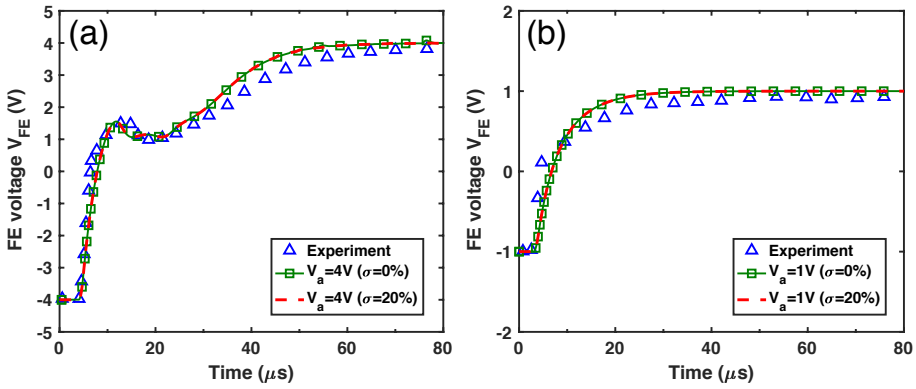

Figure 3.10: (a) The voltage transient responses under a $4\,\mathrm{V}$ voltage pulse with $\sigma = 0\%$ and $\sigma = 20\%$. (b) The voltage transient responses under a $1\,\mathrm{V}$ voltage pulse with $\sigma = 0\%$ and $\sigma = 20\%$. All the other parameters are the same as those in the main text. The experimental data are extracted from [133].

3.4.7 The distributions of phenomenological parameters

In this work, the spatial distributions of phenomenological parameters are neglected for the purpose of studying the domain interaction in HZO capacitors based on the experimental measurements [133]. In reality, the phenomenological parameters for multi-domain ferroelectric HZO capacitors may have spatial distributions, which were assumed to be Gaussian distributions for each cell of the multi-domain FE film [138]. Besides the simulations in the main text, we also perform the transient simulations with Gaussian-distributed bulk Landau parameters, $\{\alpha_1, \alpha_{11}, \alpha_{111}\}$. In [138], the mean ($\mu$) is the single domain value and the corresponding standard deviation (σ) is around 10% of the mean value. To validate the analyses, a relatively broad spatial distribution with a standard deviation of 20% is used here, as listed in Table 3.2. Fig. 3.10 shows the transient negative capacitance (NC) responses with and without spatially-distributed bulk parameters at different pulse amplitudes. It is found that the broad distributions of Landau parameters have an insignificant impact on the transient NC behaviors under the domain interaction effect, which highlights the important role domain interaction plays in the ferroelectric dynamic responses. Furthermore, it is noteworthy that the switching responses

Table 3.2: Gaussian Distributions of Bulk Landau Parameters

	α_1 (m/F)	α_{11} (m^5C^{-2}/F)	α_{111} (m^9C^{-4}/F)
μ	-4×10^8 [107]	3.7×10^9 [107]	1.1×10^9 [107]
σ	8×10^7	7.4×10^8	2.2×10^8

may also be affected by the nucleation process or grain structures [83, 160, 161]. Thus, the circuit-compatibility and computing efficiency would depend on how these polycrystalline effects are implemented.

3.5 Summary

In this chapter, the multi-domain nature of FE polarization switching dynamics in a metal-ferroelectric-metal (MFM) capacitor is explored through a physics-based phase field approach, where the three-dimensional time-dependent Ginzburg-Landau (TDGL) equation and Poisson's equation are self-consistently solved with the SPICE simulator. Systematically calibrated based on the experimental measurements, the model well captures transient negative capacitance (NC) in pulse switching dynamics of an RFEC circuit, with domain interaction and viscosity being the key parameters. We find that FE domain interaction depends on the applied voltage and plays an important role in the dynamic responses of polarization switching and the transient NC effect. Therefore, the influence of pulse amplitudes on voltage transient behaviors can be attributed to the fact that the FE free energy profile strongly depends on how the domains interact. By studying how domain interaction affects the total free energy curvature, we show that the effect of domain interaction cannot be viewed as an effective electric field. More importantly, as the domain interaction becomes stronger and stronger, the negative curvature of free energy around zero polarization turns positive. Therefore, the voltage-dependent domain interaction indicates that FE-DE capacitance matching can only be achieved at a specific voltage and frequency. Furthermore, the dynamic nature of FE domain viscosity dynamics

at a voltage pulse is explored based on the experimental measurements. For the first time, a physics-based circuit-compatible SPICE model for multi-domain phase field simulations is established to reveal the impact of domain interaction on the NC effect and microscopic domain evolution. The findings of this study may have important implications for the charge boost induced by stabilization of negative capacitance in an FE/dielectric (DE) stack since the so-called capacitance matching needs to be designed at a specific operation voltage or frequency. Overall, this work explores the physical roles that phenomenological parameters play in microscopic switching mechanisms for multi-domain HZO capacitors, and the proposed circuit model shows the potential for the analyses of HfO_2-based ferroelectrics at device and circuit levels.

CHAPTER 4
HYSTERESIS-FREE NEGATIVE CAPACITANCE EFFECT IN METAL-FERROELECTRIC-INSULATOR-METAL CAPACITORS

4.1 Overview

As the relentless pursuit of device miniaturization goes into the nanometer regime, Moore's law has gradually come to a bottleneck due to the fact that the power dissipation in microchips becomes a more and more challenging concern [137, 162]. Recently, a stack structure consisting of an FE layer and a DE layer was proposed to achieve voltage amplification in a DE layer [20]. The physical concept behind this approach is that the metastable negative capacitance (NC) state arising from the double-well energy profile of the FE can be stabilized by the DE layer in terms of the total free energy of the system. Such a proposal may provide a potential way to significantly improve the subthreshold swing of conventional complementary metal-oxide-semiconductor (CMOS) transistors at room temperature [118, 139].

Ferroelectrics are materials that exhibit the properties: (i) the electric polarization can be reversed by an externally applied voltage and (ii) the remanent polarization remains nonvolatile under zero bias. These unique properties have made ferroelectrics promising materials for voltage-controlled nonvolatile memory devices [73, 163]. In the past decade since the proposal of using NC for low-power logic devices, FE-based capacitors, including MFM, MFIM and metal-ferroelectric-metal-insulator-metal (MFMIM), have been intensively investigated experimentally and theoretically in search of the evidence for the transient and steady-state NC effects [101, 102, 105–107, 116, 138, 164–166]. In particular, recently discovered doped hafnium oxides are widely used as the FE layer due to the high scalability and CMOS process compatibility [46–48].

With an MFM capacitor connected in series with a large resistor, the transient NC behaviors have been observed in various FE materials, including perovskite $Pb(Zr_{0.2}Ti_{0.8})O_3$ and various doped hafnium oxides [105, 133, 138]. The physical origin of the observed transient NC lies in the mismatch between the switching rates of free charges and bound charges (FE polarization) in the resistor-capacitor circuit [107]. To further seek the evidence of static NC stabilization, FE-DE stacks are the key devices to be investigated according to the NC theory. Among MFIM, MFMIM and FE-DE superlattices, MFIM capacitors are of great importance because of the structure similarity to the ferroelectric field effect transistors (FeFETs). For MFIM stacks, it is unlikely to directly measure the internal DE voltage amplification, which was theoretically proposed to be achieved by the steady-state NC stabilization. Therefore, a considerable amount of experimental efforts have been focused on the evidence of capacitance enhancement in an MFIM capacitor compared to the associated standalone DE capacitor [99]. Such a capacitance enhancement is referred to as the charge boost effect.

In recent research progress, it was experimentally observed that the charge boost effect and hysteresis-free static "S-shaped curve" could be achieved in MFIM with short pulse measurements [106, 116]. On one hand, the charge boost may indicate that the MFIM capacitor has a larger capacitance than the associated DE capacitor, which was allegedly caused by the NC stabilization. On the other hand, the observed hysteresis-free FE switching (S-curve), which is predicted by the Landau phenomenological formalism, is a required characteristic for the logic applications. However, the physical mechanisms for these observations are still not clear. For example, Liu *et al.* have recently proposed an alternative perspective on such experimental observations [167]. Therefore, it is of great importance to further explore the underlying physical mechanisms for such prospective experimental evidence of NC stabilization.

In this work, we establish a physical model for MFM and MFIM capacitors by introducing the inevitable DE leakage and trapped charges at the FE-DE interface. We

show that the experimentally measured hysteresis loop of MFM capacitors can be well described by the Landau formalism with the proposed physical mechanisms included. The charge boost and hysteresis behaviors observed in the pulse measurements are found to be directly influenced by the FE intrinsic domain viscosity and DE leakage, respectively. The kinetic coefficients extracted from the charge responses are found to be linked to the well-known Merz's law [168] in the NC region. Our simulation results suggest that the experimentally observed hysteresis-free capacitance enhancement of MFIM may be caused not by the NC stabilization and capacitance matching but by the material properties of the heterostructure. Furthermore, the possible cause of the experimentally observed residual charges may be explained by the trapped charges existing at the FE-DE interface.

Overall, this chapter is organized as follows. In Sec. 4.2, the theoretical approach is presented to describe the switching characteristics of MFM and MFIM capacitors, with the DE leakage and trapped charge mechanisms included. In Sec. 4.3, based on the physical model, the FE material parameters can be well extracted using the hysteresis measurements. More importantly, the experimentally observed charge boost and hysteresis-free static S-curve are well captured, and a physical picture for such phenomena is provided and discussed in detail. In Sec. 4.4, we conclude this work by highlighting the underlying mechanisms for experimental observations.

4.2 Theoretical Formalism

To describe the electrical properties of MFIM bilayer stacks measured in the experiments, Kirchhoff's law is applied for the schematic circuit diagram shown in Fig. 4.1. The total current I_{R} flowing through the series resistor is thus expressed as

$$I_{\mathrm{R}} = A\frac{\partial Q_{\mathrm{f}}}{\partial t} = \frac{V_{\mathrm{in}} - V_{\mathrm{out}}}{R}, \tag{4.1}$$

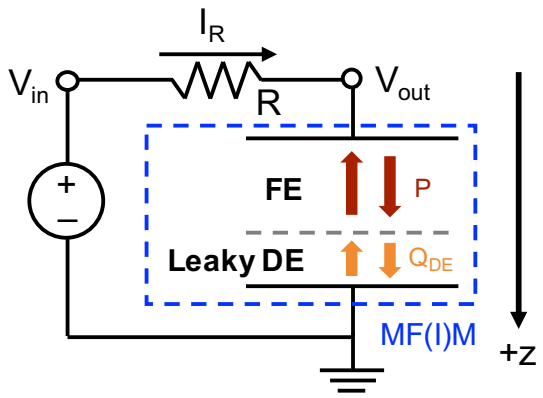

Figure 4.1: The schematic diagram of a resistor-capacitor circuit for the study of switching dynamics in the experimental measurements. The positive axis is defined as the z direction toward ground.

where Q_{f} is the free charge density, R is the series resistance and A is the capacitor area. In addition, the following conditions have to be satisfied by assuming the electric displacement field is continuous at the material boundaries:

$$I_{\mathrm{R}} = I_{\mathrm{FE}} = I_{\mathrm{DE}} + I_{\mathrm{L}}, \tag{4.2}$$

where I_{L} represents the DE leakage current, and I_{FE} and I_{DE} are the displacement current of the FE and the DE layers, respectively. Instead of the conventional DC leakage current, I_{L} here describes the transient DE leakage due to the voltage across the DE layer, as will be detailed later.

In the FE layer, the displacement charge density Q_{FE} can be written as

$$Q_{\mathrm{FE}} = \epsilon_0 \kappa E_{\mathrm{FE}} + P, \tag{4.3}$$

where ϵ_0 is the vacuum dielectric constant, κ is the background dielectric constant of the FE material [70], E_{FE} is the electric field across the FE oxide, and P is the average FE

polarization. The dynamics of P is governed by the Landau-Khalatnikov (LK) equation,

$$\frac{\partial P}{\partial t} = -L\big(2\alpha_1 P + 4\alpha_{11}P^3 + 6\alpha_{111}P^5 - E_{\text{FE}}\big), \tag{4.4}$$

where $\{\alpha_1, \alpha_{11}, \alpha_{111}\}$ are thermodynamic expansion coefficients for the bulk FE free energy, and L is the kinetic coefficient, which is inversely proportional to domain viscosity [64–66, 107, 118]. Note that with the kinetic coefficient that can capture the multi-domain nature of the FE, Eq. (4.4) is used as an approximation that describes the macroscopic polarization dynamics without considering the polarization gradient and the corresponding domain interactions in polycrystalline films [166, 169]. In general, the leakage of a HfO_2-based FE may depend on the doping element, the doping ratio as well as the electrode materials [138, 170]. Previous experimental studies have found that the leakage of $Hf_{0.5}Zr_{0.5}O_2$ (HZO) capacitors with WN metal contacts does not significantly increase until the FE thickness is scaled down to $4\,\text{nm}$ and below [170]. Moreover, further analyses based on the experimental measurements in Refs. [138] and [116] also show that the leakage of the $11.3\,\text{nm}$ FE HZO is negligible for the MFM and MFIM capacitors in this study. As a result, the free charge density Q_{f} is equal to the FE displacement charge density Q_{FE}.

It was experimentally reported that the trapped charges may exist at the FE-DE interface through the DE leakage, which plays an important role in the electrical properties and DE breakdown of MFIM capacitors [171]. In this regard, we introduce DE leakage and interfacial trapped charges into the MFM and MFIM systems. According to the experiments on ultrathin Al_2O_3 (AO) dielectrics [172], the DE leakage approximated as field-assisted tunneling can be generally expressed as

$$I_{\text{L}} = \text{sgn}(E_{\text{DE}})\alpha E_{\text{DE}}^2 \exp\left(-\beta/|E_{\text{DE}}|\right) \cdot A, \tag{4.5}$$

where E_{DE} is the electric field across the DE oxide, α and β are physical parameters

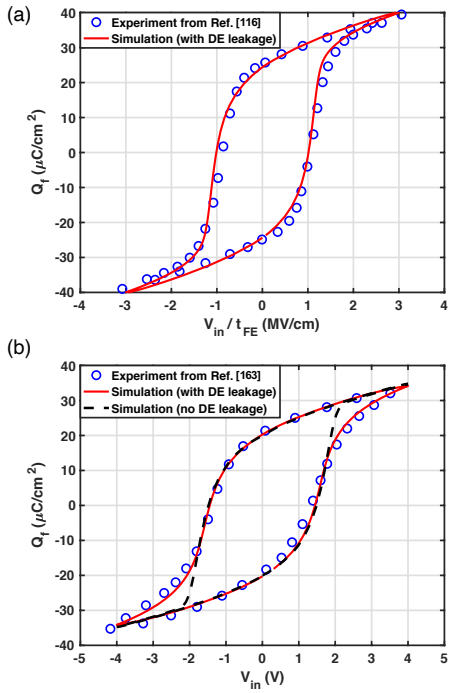

Figure 4.2: (a) The simulated hysteresis loop of a TiN/(11.3 nm HZO)/TiN MFM capacitor in comparison with the experimental data extracted from [116]. (b) The simulated hysteresis loop of a TiN/(10 nm HZO)/TiN MFM capacitor in comparison with the experimental data extracted from [163]. The simulation without an interfacial oxide layer and the associated DE leakage is plotted for comparison.

determined by the electron effective mass and the tunneling barrier height, and a sign function is used for the current direction. The leakage current when the DE voltage V_{DE} is below a cutoff voltage V_{c} is assumed to be negligible for simplicity, where V_{c} is set to $0.2\,\mathrm{V}$ in this work. Extracted from the experimental measurements in [116], β in Eq. (4.5) is found to be a small constant value of $3.7 \times 10^{-7}\,\mathrm{V/m}$ for all the simulations. Note that the leakage current level obtained from the experiments is much smaller than that predicted by conventional Fowler-Nordheim (FN) tunneling, where α and β are not independent of each other. The smaller transient leakage current measured in the experiments may possibly be attributed to the charges temporarily trapped in the DE layer during the tunneling process, whereas FN tunneling formalism captures a much larger leakage current in the steady state, where more charges can tunnel through the DE layer. Therefore, the transient leakage current may depend on charge trapping inside the DE layer, and may not be directly

Table 4.1: Parameters Used For MFM from [116]

Parameter	Value
Area (A) $(\mu\mathrm{m}^2)$	7000 [116]
FE thickness (t_{FE}) (nm)	11.3 [116]
α_1 (m/F)	-1.43×10^8
α_{11} $(\mathrm{m}^5\mathrm{C}^{-2}/\mathrm{F})$	1.55×10^9
α_{111} $(\mathrm{m}^9\mathrm{C}^{-4}/\mathrm{F})$	1.1×10^9
κ	10
L $\left([\Omega\mathrm{m}]^{-1}\right)$	3×10^{-3}
EOT (t_{DE}) (nm)	0.1
α $(\mathrm{A/V}^2)$	9.57×10^{-16}
Frequency (kHz)	10 [116]
Pulse amplitude (V)	3.5 [116]

described by conventional FN tunneling.

To extract the DE charge density (Q_{DE}) accumulated at the DE-metal interface, we integrate the displacement current through the DE layer with respect to time:

$$Q_{\mathrm{DE}}(t) = \frac{1}{A}\int_0^t I_{\mathrm{DE}}(\tau)\,\mathrm{d}\tau + Q_{\mathrm{DE}}(0), \tag{4.6}$$

where $Q_{\mathrm{DE}}(0)$ is the DE charges before switching. Note that $Q_{\mathrm{DE}}(0)$ is an initial condition in this framework and may vary from sample to sample depending on the experimental conditions.

At the FD-DE interface, the charge neutrality condition has to be satisfied due to the displacement field continuity in the normal direction. Therefore, the interfacial trapped charge Q_{it} can be obtained with the expression given by

$$Q_{\mathrm{FE}} + \widetilde{Q}_{\mathrm{DE}} + Q_{\mathrm{it}} = 0, \tag{4.7}$$

where $\widetilde{Q}_{\mathrm{DE}} = -Q_{\mathrm{DE}}$ is the DE charge at the FE-DE interface.

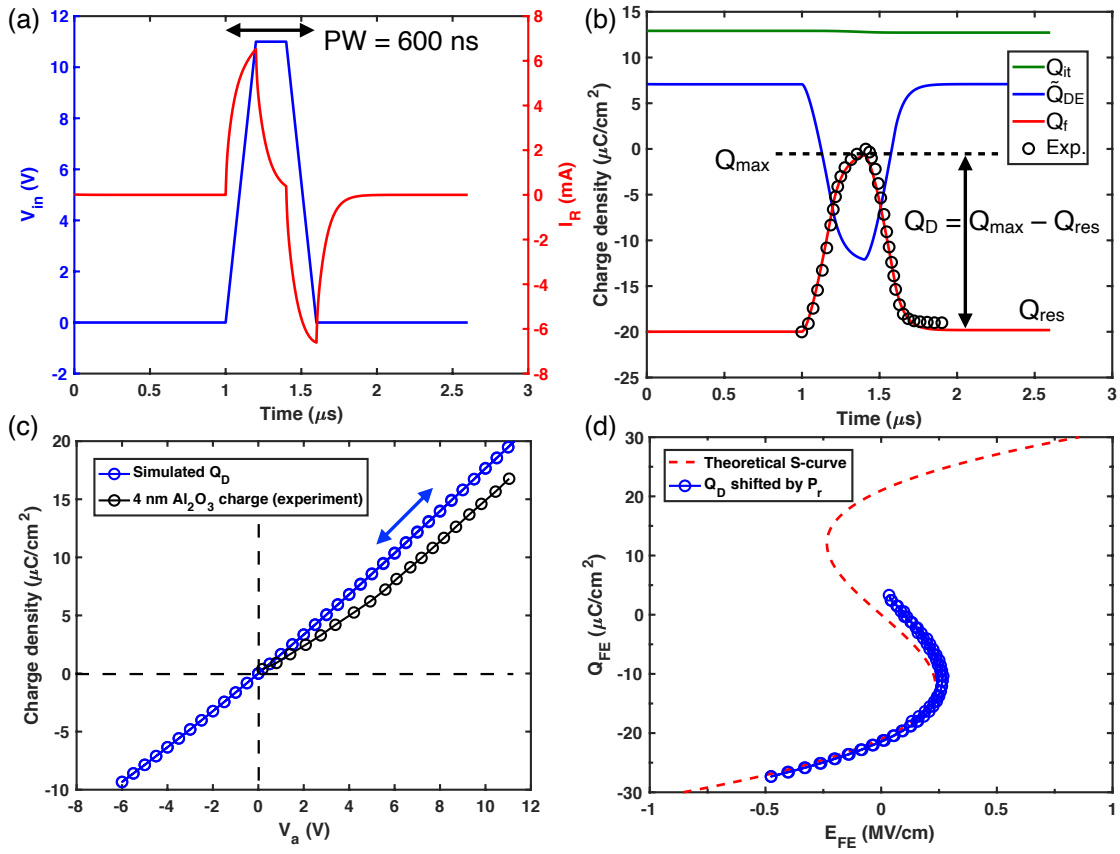

Figure 4.3: (a) The applied pulse V_{in} from [116] (left) and the simulated current flowing through the series resistor I_{R} (right). (b) Simulated transient responses of the free charge Q_{f} and the calculated DE charge Q_{DE} and trapped charge Q_{it} in comparison with the measured free charge response extracted from [116]. The definitions of Q_{max}, Q_{res} and Q_{D} in the main text are also shown. (c) The release charge Q_{D} at ascending and descending pulse trains with the amplitude V_{a}: $0\,\text{V} \rightarrow 12\,\text{V} \rightarrow -6\,\text{V} \rightarrow 0\,\text{V}$, showing the hysteresis-free charge boost compared to the charges on the associated standalone AO capacitor extracted from [116]. (d) The simulated hysteresis-free S-curve compared to the static curve predicted by the Landau formalism using the FE material parameters obtained in Sec. 4.3.1.

4.3 Results and Discussion

Based on the physical model described in Sec. 4.2, we study the transient charge responses of MFM and MFIM capacitors, including hysteresis loops and pulse switching dynamics. The underlying physics behind the recent experimental observations is discussed in detail. For convenience, the theoretical model is implemented in a circuit-compatible manner so that all the dynamic simulations can be performed accurately and self-consistently in the

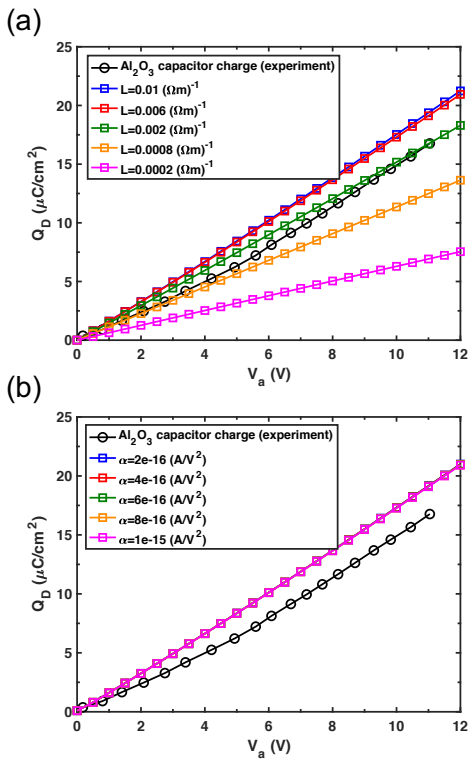

Figure 4.4: (a) The effect of L on the charge boost effect. As L increases, the release charge Q_{D} on MFIM gradually becomes larger than that on the associated standalone DE capacitor. (b) The effect of α on the charge boost, which indicates that the charge boost is not dominated by the DE leakage. The charges on AO are extracted from the measurements in [116].

SPICE simulator. The detailed implementation can be found in [166].

4.3.1 MFM capacitors

The MFIM stack structure of interest is TiN/$Hf_{0.5}Zr_{0.5}O_2$/Al_2O_3/TiN capacitors, where Zr-doped hafnium oxides (HZO) are a widely used FE material in the recent experimental measurements [73, 106, 116, 133, 165]. Before we study the MFIM capacitors, we first extract the FE parameters by simulating the hysteresis loops of TiN/HZO/TiN MFM capacitors based on the conventional polarization-voltage (P-V) measurements. As suggested by the experiments [173–176], an interfacial oxide layer is likely to form between the FE layer and the metal contacts during the fabrication process of MFM capacitors. In this regard, an ultrathin DE layer is introduced at the FE-metal interface of an MFM

capacitor. Note that the depolarization field, which is caused by the finite screening effect of the metal contacts, manifests itself with the interfacial oxide layer [177]. Based on the P-V measurement in [116], the equivalent oxide thickness (EOT) of the interfacial oxide layer is found to be around $0.1\,\mathrm{nm}$ given that the dielectric constant of SiO_2 (ϵ_{SiO_2}) is 3.9. The corresponding interfacial capacitance $C_{\mathrm{DE}} = \epsilon_0\epsilon_{SiO_2}/\mathrm{EOT} \approx 0.35\,\mathrm{F/m^2}$, which is consistent with the reported value for the HZO/TiN interface [177]. The physical thickness of the interfacial oxide layer can be estimated to be $0.9\,\mathrm{nm}$ given the relative permittivity of 36 for the tetragonal and orthorhombic phase in HfO_2 and ZrO_2 [177]. Fig. 4.2(a) shows the simulated hysteresis loop of an MFM capacitor based on the experimental P-V measurement in [116]. To further confirm the effect of an oxide layer between the FE and the metal contact, we simulate the hysteresis loop of an MFM capacitor from another measurement [73], as shown in Fig. 4.2(b). The simulation without considering the interfacial oxide layer is also plotted for comparison. Our simulations indicate that the oxide layer at the FE-metal interface may be one of the important factors that could influence the hysteresis shape of MFM. The parameters extracted based on the experimental P-V measurement in [116] are summarized in Table 4.1. The FE properties of $11.3\,\mathrm{nm}$ HZO are used for the study of MFIM capacitors.

4.3.2 MFIM capacitors

To study the TiN/HZO/AO/TiN capacitor, we apply the parameters obtained from the preceding section for $11.3\,\mathrm{nm}$ HZO. Based on the experimental setup in [116], ascending and descending pulse trains with a $600\,\mathrm{ns}$ pulse width (PW) were applied to the MFIM capacitor with $11.3\,\mathrm{nm}$ HZO and $4\,\mathrm{nm}$ AO. One of the voltage pulses and the total current flowing through the external resistor are shown in Fig. 4.3(a). Fig. 4.3(b) shows the corresponding transient free charge responses from the simulation. In the steady state before the pulse voltage is applied, the FE layer is in the negative remanent polarization (P_{r}) state, as suggested in [116]. To compensate the FE charge density, there must be

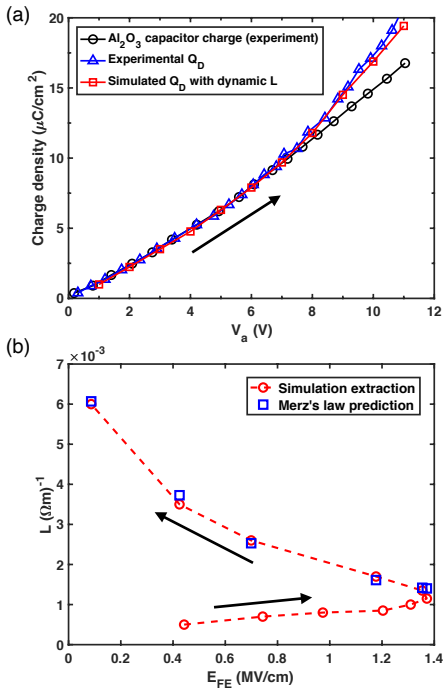

Figure 4.5: (a) The corresponding Q_{D} (red) using L extracted based on the measured charge responses (blue) in comparison with the charges on the standalone AO capacitor (black). The experimental measurements are from [116]. (b) The extracted L in the NC region compared to the Merz's law prediction with $E_0 = 0.12\,\mathrm{MV/cm}$. The turning point of E_{FE} indicates the onset of NC region. The black arrows in (a) and (b) indicate the applied voltage sweep direction.

the same amount of charges with opposite signs at the FE-DE interface. However, a dielectric material like AO cannot support a charge density as large as around $20\,\mu\mathrm{C/cm^2}$ for such a long period of time without breakdown [171, 172]. Therefore, here the initial DE charge $\widetilde{Q}_{\mathrm{DE}}(0)$ is assumed to be $7\,\mu\mathrm{C/cm^2}$ as reported in [171], and the rest of the compensating charges are from the interfacial trapped charge Q_{it} [171]. Such a large amount of trapped charges are likely to be introduced through the DE leakage to the FE-DE interface during the wake-up process after the fabrication. At a large pulse amplitude, a large amount of negative DE charges accumulated at the FE-DE interface indicate that most of the applied voltage is across the DE layer in this stack system. Thus, in such pulse measurements, the FE polarization is barely switched even if a large voltage is applied. Similar to the experiments, the release charge Q_D is defined as the difference between the

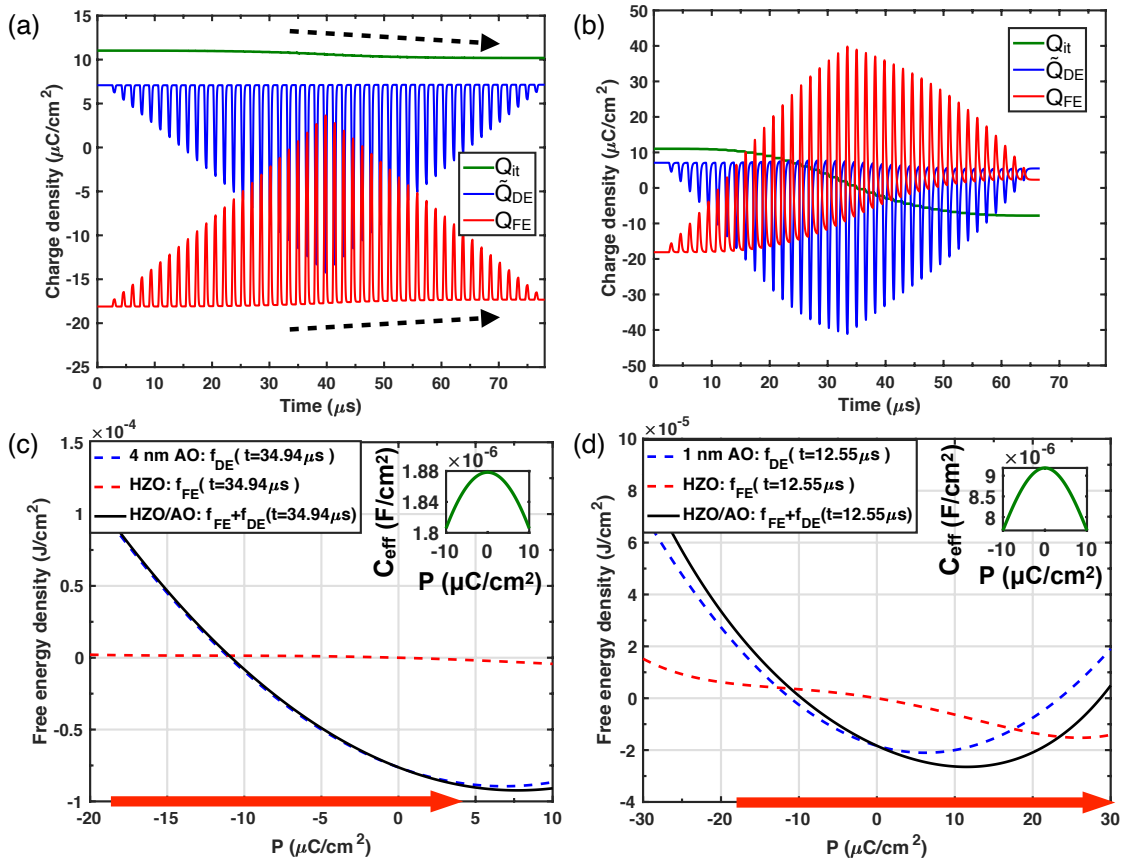

Figure 4.6: (a) Charge responses of the (11.3 nm HZO)/(4 nm AO) stack at ascending and descending pulse trains with the amplitude V_a: 0 V $\rightarrow$ 12 V $\rightarrow$ 0 V. The dashed arrows indicate the trapped charge leak and the increasing residual charges during the pulse trains. $\alpha = 2 \times 10^{-16}$ A/V^2 for the 4 nm AO stack. (b) Charge responses of the (11.3 nm HZO)/(4 nm AO) stack at ascending and descending pulse trains with V_a: 0 V $\rightarrow$ 10 V $\rightarrow$ 0 V. $\alpha = 7.57 \times 10^{-16}$ A/V^2 for the 1 nm AO stack. (c) The free energy profiles of the 11.3 nm HZO, the 4 nm AO, and the corresponding HZO/AO stack near zero polarization at $t = t_0$. The red arrow indicates the switching range of P during the simulation. (d) The free energy profiles of the 11.3 nm HZO, the 1 nm AO, and the corresponding HZO/AO stack near zero polarization at $t = t_0$. The red arrow indicates the switching range of P during the simulation.

maximum charge Q_{max} and the residual charge Q_{res} at a given pulse amplitude V_a; that is, $Q_D = Q_{\text{max}} - Q_{\text{res}}$. At a fixed kinetic coefficient $L = 6 \times 10^{-3}\,(\Omega\text{m})^{-1}$, it is found that Q_D of MFIM is enhanced without hysteresis compared to the measured charges on the associated standalone 4 nm AO capacitor, as shown in Fig. 4.3(c). From the simulation, the electric field across the FE oxide, $E_{\text{FE}} = V_{\text{FE}}/t_{\text{FE}}$, can be directly obtained, and the

theoretical static curve is derived from Eq. (4.4) in the steady state:

$$E_{\mathrm{FE}} = 2\alpha_1 P + 4\alpha_{11} P^3 + 6\alpha_{111} P^5. \tag{4.8}$$

Fig. 4.3(d) shows that an S-curve with negligible hysteresis can be achieved with the DE leakage parameter $\alpha = 2 \times 10^{-16}\,\mathrm{A/V^2}$. For the static curve, Q_D is shifted by P_{r}, which is the initial reference point and was reported as around $18\,\mu\mathrm{C/cm^2}$ [116]. Note that the S-curve obtained from the simulation does not go through the origin because L for the FE response has not been calibrated dynamically based on the polarization charge responses.

In Fig. 4.4(a), we show that the experimentally observed charge boost is mainly determined by the kinetic coefficient L. The increasing L indicates the faster FE charge responses to the applied voltage, leading to larger maximum charges Q_{max} in the same PW. Hence, the release charge Q_{D} can be enhanced with less FE domain viscosity. To further confirm this finding, we also explore the effect of DE leakage α and find that the DE leakage is not a dominant factor in the observed charge boost effect, as shown in Fig. 4.4(b).

Based on the experimentally measured free charge response from [116], the kinetic coefficient L can be numerically extracted at a given pulse amplitude. With extracted L, Fig. 4.5(a) demonstrates that the charge boost is enhanced when the applied pulse is large enough to induce the FE response, whereas a small applied pulse only results in the DE response in the FE layer and thus no charge boost is observed. As a reciprocal of the domain viscosity, L is assumed to be proportional to the domain wall mobility μ_{d} corresponding to the domain nucleation; that is, $L \propto \mu_{\mathrm{d}}$. Based on Merz's law [168], the relationship between L and nonzero E_{FE} can be derived:

$$L \propto \frac{\mu_{\mathrm{d}}|E_{\mathrm{FE}}|}{|E_{\mathrm{FE}}|} \propto \frac{1}{|E_{\mathrm{FE}}|} v_{\mathrm{d}} \propto \frac{1}{|E_{\mathrm{FE}}|}\frac{1}{t_{\mathrm{s}}} \propto \frac{1}{|E_{\mathrm{FE}}|} e^{-E_0/|E_{\mathrm{FE}}|}, \tag{4.9}$$

where v_{d} is the domain wall velocity inversely proportional to the switching characteristic time t_{s}, and E_0 is the activation field for domain switching [168]. Fig. 4.5(b) shows that

when the FE is driven into the NC region, L can be described by Merz's law, which suggests the domains are likely to be in the creep region as the electric field across the FE (E_{FE}) becomes smaller [91]. From Eq. (4.9), as $|E_{\text{FE}}|$ approaches 0^+, L is asymptotic to zero because of zero driving force for domain switching. Before FE domain switching, only the DE response is induced, and L is found to be linearly dependent on E_{FE}.

In contrast to the TiN/($11.3\,\text{nm}$ HZO)/($4\,\text{nm}$ AO)/TiN capacitor, the charge hysteresis was observed in a TiN/($11.3\,\text{nm}$ HZO)/($1\,\text{nm}$ AO)/TiN capacitor [116]. It was suggested that the appearance of such hysteresis was attributed to the capacitance mismatch between the FE and the DE layer as the DE thickness decreases based on the theory of NC stabilization. However, here we demonstrate that such hysteresis is caused by the DE leakage and the associated interfacial trapped charge dynamics instead of NC stabilization. At the pulse trains with ascending and descending amplitudes, Fig. 4.6(a) and (b) show the charge responses of the ($11.3\,\text{nm}$ HZO)/($4\,\text{nm}$ AO) stack and the ($11.3\,\text{nm}$ HZO)/($1\,\text{nm}$ AO) stack, respectively. For the ($11.3\,\text{nm}$ HZO)/($4\,\text{nm}$ AO) stack, when a large voltage is across the DE layer, DE leakage is induced and therefore, the trapped charges leak out through the DE, as can be seen from the slightly decreased Q_{it} in Fig. 4.6(a). As a result, the residual charges of Q_{f} after each pulse gradually increase in Fig. 4.6(a). For the ($11.3\,\text{nm}$ HZO)/($1\,\text{nm}$) AO stack in Fig. 4.6(b), the leakage effect becomes more evident compared to the ($11.3\,\text{nm}$ HZO)/($4\,\text{nm}$ AO) stack. The simulations indicate that the possible cause of the increasing residual charges after pulse switching experimentally observed in [116], especially at a large pulse amplitude, can be explained by the transient responses of trapped charges at the FE-DE interface. Furthermore, from Fig. 4.6(a) and (b) and Eq. (4.6), one can infer that the role of the initial DE charge $\widetilde{Q}_{\text{DE}}(0)$ plays in the transient responses is a shift in $\widetilde{Q}_{\text{DE}}$ and Q_{it} dynamics, which means that the choice of the $\widetilde{Q}_{\text{DE}}(0)$ value does not affect the conclusions drawn from the simulations.

The hysteresis behavior can be studied with the curvature of the total free energy profile of the system near polarization reversal. The Landau free energy of the FE in a unit of J/m^2

is given by

$$f_{\text{FE}} = \big(\alpha_1 P^2 + \alpha_{11} P^4 + \alpha_{111} P^6 - E_{\text{FE}} P\big) t_{\text{FE}}. \tag{4.10}$$

The Gibbs free energy of the DE layer [79] in terms of P can be derived as

$$\begin{aligned} f_{\text{DE}} &= Q_{\text{DE}}^2/(2C_{\text{DE}}) - Q_{\text{DE}} V_{\text{DE}} \\ &= (P - \Delta Q)^2/(2C_{\text{DE}}) - (P - \Delta Q) V_{\text{DE}}, \end{aligned} \tag{4.11}$$

where C_{DE} is the DE capacitance per unit area and $\Delta Q = P - Q_{\text{DE}}$ is the difference between polarization and the DE charges, which is caused by the interfacial trapped charges. Fig. 4.6(c) and (d) show the free energy profiles of the FE, the DE, and the FE-DE stacks at $t = t_0$, where t_0 is the time at which P is around $0\,\mu\text{C}/\text{cm}^2$. Note that in the presence of the trapped charges, the FE and DE energy profiles do not align at $P = 0\,\mu\text{C}/\text{cm}^2$ because the FE charges are not totally compensated by the DE charges. In the ($11.3\,\text{nm}$ HZO)/($4\,\text{nm}$ AO) stack, polarization P is switched between one of the energy minima and the energy maximum, as indicated by the red arrow in Fig. 4.6(c). In other words, P does not go to the other energy minimum state. Note that when P is around the energy maximum, the FE is driven into its NC region, where the curvature of the free energy profile (and the FE capacitance) is negative. The effective capacitance C_{eff} of the MFIM system can be obtained by calculating the curvature of the total free energy profile:

$$C_{\text{eff}} = \left(\frac{\partial^2 f_{\text{DE}}}{\partial P^2} + \frac{\partial^2 f_{\text{FE}}}{\partial P^2} \right)^{-1}. \tag{4.12}$$

From Eq. (4.12), C_{eff} is positive when the positive DE capacitance is dominant over the negative FE capacitance. With a positive C_{eff}, the NC region gets stabilized and no hysteresis is expected according to the NC theory [20, 112]. Note that ΔQ in Eq. (4.11) (and thus trapped charges) does not affect the effective capacitance.

As shown in the inset of Fig. 4.6(c), the effective capacitance of the $4\,\text{nm}$ AO stack is positive around zero polarization, indicating the FE-DE capacitance match and thus

hysteresis-free NC stabilization. For the $1\,\mathrm{nm}$ AO stack, the effective capacitance is also positive around zero polarization, as shown in the inset of Fig. 4.6(d). Therefore, based on the theory of NC stabilization, such a $1\,\mathrm{nm}$ AO stack is not expected to show hysteresis. However, consistent with the experimental findings in [116], the release charge Q_{D} of such a $1\,\mathrm{nm}$ AO stack shows clear hysteresis with the DE leakage parameter $\alpha = 7.57 \times 10^{-16}\,\mathrm{A/V^2}$ in the simulation, as shown in Fig. 4.7. Note that α of the $1\,\mathrm{nm}$ AO stack is larger than that of the $4\,\mathrm{nm}$ AO stack due to the larger leakage current in a thinner DE. In contrast to the $4\,\mathrm{nm}$ AO stack, the FE polarization of the $1\,\mathrm{nm}$ AO stack is driven into the other energy minimum state in the measurement, as indicated by the red arrow in Fig. 4.6(d). The appearance of hysteresis in the $1\,\mathrm{nm}$ AO stack can be attributed to the increasing FE charge responses due to the larger DE leakage of the thinner DE compared to the $4\,\mathrm{nm}$ AO stack. Therefore, we show that the hysteresis observed in an MFIM stack with a reduced DE thickness is caused not by the FE-DE capacitance mismatch but by the fact that the FE polarization transitions from one state to the other state with the help of DE leakage. This finding is consistent with the previous experimental observation of FE-gated Ge p-channel transistors [178]. In addition, Fig. 4.7 shows that, for the MFIM with $1\,\mathrm{nm}$ AO, the maximum release charge difference in the hysteresis $\Delta Q_{\mathrm{D}} \approx 5.2\,\mu\mathrm{C/cm^2}$ at the pulse amplitude of $7\,\mathrm{V}$, which is close to the reported value of $4.7\,\mu\mathrm{C/cm^2}$ in [116]. Note that the hysteresis direction is in a clockwise manner, which is also consistent with the experimental measurements in [116].

As a final remark, although we demonstrate the dynamics of trapped charges in response to the pulse measurements in this work, the frequency and temperature responses of the FE polarization and the corresponding trapped charges may rely on a better understanding of microscopic behaviors of HfO_2-based FE [179]. In addition, the interplay between the trapped charge dynamics and FE polarization switching also requires more experimental characterization, especially for nonvolatile memory applications [73, 180].

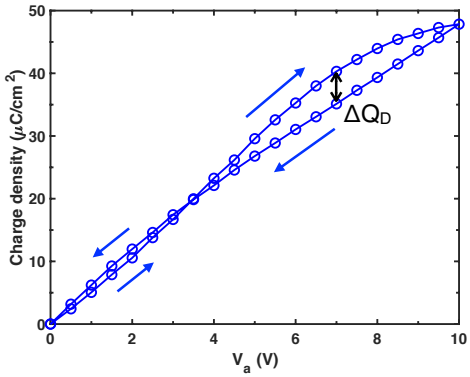

Figure 4.7: The release charge Q_{D} of the $(11.3\,\mathrm{nm}$ HZO)/$(1\,\mathrm{nm}$ AO) stack with $\alpha = 7.57 \times 10^{-16}\,\mathrm{A/V^2}$ shows clear hysteresis in a clockwise manner, as observed in [116].

4.4 Summary

The negative capacitance (NC) stabilization of a ferroelectric (FE) material can potentially provide an alternative way to further reduce the power consumption in ultra-scaled devices and thus has been of great interest in technology and science in the past decade. In this chapter, we present a physical picture for a better understanding of the hysteresis-free charge boost effect observed experimentally in metal-ferroelectric-insulator-metal (MFIM) capacitors. By introducing the dielectric (DE) leakage and interfacial trapped charges, we extract the FE parameters by capturing the measured hysteresis loops of metal-ferroelectric-metal (MFM) capacitors. Our simulations of the hysteresis loops are in strong agreement with the experimental measurements, suggesting the existence of an interfacial oxide layer at the FE-metal interface in MFM capacitors. More importantly, for MFIM stacks, we show (i) the charge boost is mainly determined by the faster FE domain responses near the polarization reversal and (ii) the charge responses would show hysteresis as long as the FE polarization is switched from one state to the other with the aid of DE leakage. In other words, the charge enhancement and hysteresis are dominated by the FE domain viscosity and DE leakage, respectively. The analyses of thermodynamic energy profiles in the presence of interfacial trapped charges indicate that the observed hysteresis in MFIM is caused by the FE polarization switching rather than the FE-DE capacitance

mismatch suggested by the theory of NC stabilization. Therefore, our simulation results show that the underlying mechanisms for the observed hysteresis-free charge enhancement in MFIM may be physically different from the alleged NC stabilization and capacitance matching. Moreover, the link between Merz's law and the phenomenological kinetic coefficient is discussed, and the possible cause of the residual charges observed after pulse switching is explained by the trapped charge dynamics at the FE-DE interface. The theoretical demonstrations presented in this work can provide important physical insights into the NC effect in MFIM capacitors and future studies of emerging low-power logic devices.

CHAPTER 5

POLARIZATION SWITCHING DYNAMICS OF MULTIFERROIC $BiFeO_3$ IN ANTIFERROMAGNET/FERROMAGNET HETEROJUNCTIONS

5.1 Overview

In addition to FE-based electronic devices, spintronic devices are also considered promising candidates for beyond CMOS logic and memory applications due to the potential for high endurance and nonvolatility [58]. Among proposed low-power and magnetic-field free devices, magnetoelectric devices can alleviate the problem of a high threshold current and the accompanying joule-heating effect during and even after magnet switching. Conventionally, in order for a magnetic tunnel junction to flip the magnetic moment of a ferromagnet by $180°$, either an extra spin current or a careful control of the voltage pulse width has to be applied for a deterministic magnet switching. Multiferroic materials that have at least two of the ferroic properties, including ferroelectricity, ferromagnetism, and ferroelasticity, can successfully switch the magnetic moment of the adjacent ferromagnet by $180°$ when a reverse electric field is applied, as experimentally demonstrated in $BiFeO_3$ (BFO).

In terms of magnetism, even if BFO is a G-type antiferromagnet, it has a weak magnetization that comes from Dzyaloshinskii-Moriya interaction (DMI) because of the tilting of the oxygen octahedron from the ideal ABO_3 perovskite structure combined with the spin-orbit coupling effect [181, 182]. This weak magnetization in BFO is observed under a large magnetic field [183] or in a thin film structure [123] because the spin cycloid is destroyed by the large magnetic field or the broken symmetry from the epitaxial constraint in a thin film [58]. In terms of ferroelectricity, the ferroelectricity of BFO mostly originates from the displacement of Bi^{3+} ions relative to the rest of the lattice under an applied

electric field. Thus, the application of a sufficiently strong applied electric field will reverse the polarization [124, 125]. During the polarization reversal, the iron ions and oxygen octahedra also rotate, which causes the weak magnetization to rotate [57]. The energy of DMI can be expressed as

$$f_{\text{DMI}} = \sum_{i=1}^{N} \sum_{j \neq i}^{nn} \mathbf{D}_{ij} \cdot (\mathbf{M}_i \times \mathbf{M}_j), \tag{5.1}$$

where $\mathbf{D}_{ij}$ is the DM vector between cells i and j, and $\mathbf{M}_i$ and $\mathbf{M}_j$ are the magnetic moments of the cells i and j, respectively. The direction of the DM vector is determined by the cross product of the displacement of the oxygen ion from the midpoint between Fe ions $(\mathbf{x})$ and the distances between two Fe ions $(\mathbf{r}_{ij})$ so that $\mathbf{D}_{ij} = V_0(\mathbf{r}_{ij} \times \mathbf{x})$, where V_0 is the microscopic constant. From a crystallographic point of view, the rotation of the oxygen octahedra is anti-phase when viewed from the rotation axis, which is also called anti-ferrodistortive axis θ of BFO [181]. Hence, the displacement of both oxygen ion, $(\mathbf{x})$ and the DM vector $\mathbf{D}_{ij}$ are staggered vectors or quasi-axial vectors, and the direction of $\mathbf{D}_{ij}$ is determined by θ [184]. One can also rewrite the energy of DMI as

$$f_{\text{DMI}} \approx \sum_{i=1}^{N} \mathbf{D}_{ij} \cdot (\mathbf{N} \times \mathbf{M}_\mathbf{c}) = \mathbf{H}_{\text{DMI}} \cdot \sum \mathbf{M}_i^{\text{AFM}} \tag{5.2}$$

by considering there are two sublattices 1 and 2, where $\mathbf{N} = (\mathbf{M}_1 - \mathbf{M}_2)/(|\mathbf{M}_1| + |\mathbf{M}_2|)$ is the Néel vector, $\mathbf{M}_\mathbf{c} = (\mathbf{M}_1 + \mathbf{M}_2)/(|\mathbf{M}_1| + |\mathbf{M}_2|)$ is the weak magnetization, and $\mathbf{H}_{\text{DMI}} = (\mathbf{D}_{ij} \times \mathbf{N})/M_s$ is the effective magnetic field of DMI since the direction of $\mathbf{M}_i \times \mathbf{M}_j$ is equal to $\mathbf{N} \times \mathbf{M}_\mathbf{c}$. Note that because of the cross-product relation between $\mathbf{D}_{ij}$, $\mathbf{N}$, and $\mathbf{M}_\mathbf{c}$, these three vectors always form a right-handed system [185].

The as-grown polarization domain configuration of $100\,\text{nm}$ BFO in pseudocubic $[001]_\text{p}$ was experimentally found to show a stripe-like pattern with 71° domain walls. When an out-of-plane voltage is applied to the BFO film, both polarization states switch in two steps: 71° switching in the in-plane (IP) direction followed by an out-of-plane (OOP)

109° switching, resulting in an overall 180° switching [57]. A schematic of such a polarization switching path is shown in Fig. 5.1. Taking advantage of the coupling of the ferroelectric and antiferromagnetic orders in BFO and the interface exchange coupling between BFO and an adjacent ferromagnetic CoFe layer, several experiments have demonstrated voltage-controlled 180° switching of the magnetic order in CoFe [57, 124, 186, 187].

Interestingly enough, the polarization stays in the same crystal plane during the 180° reversal, which was argued to be attributed to the elastic constraints from the rhombohedral crystal structure of BFO. By introducing the easy-plane energy and domain wall field into the thermodynamic potential, we successfully describe such a two-step switching process using the single-domain Landau-Khalatnikov (LK) equation. Based on the deterministic polarization switching dynamics, we develop a comprehensive modeling framework to better understand the fundamental physics of the switching mechanisms of the antiferromagnet (AFM)/ferromagnet (FM) heterojunction by taking $BiFeO_3$/CoFe heterojunctions as an example. In this work, we consider a (001)-oriented BFO thin film grown on a $DyScO_3$ substrate with a CoFe thin film on top of the BFO. Our model of the BFO/CoFe heterojunction is set up according to the following steps. First, we consider the total energy terms in BFO and CoFe. The coupling between BFO and CoFe is simulated by the interface exchange coupling. Next, the polarization dynamics and the spin dynamics of BFO after applying an electric field are solved by the LK and the Landau-Lifshitz-Gilbert (LLG) equations, respectively. The magnetic hard axis of BFO, which is parallel to the electric polarization $\mathbf{P}$, will rotate simultaneously in the micromagnetic model following the experimental observation [188]. Overall, the rotation of $\mathbf{P}$ under an electric field would rotate both the antiferromagnetic order in BFO and the magnetization in CoFe because of the intrinsic magnetoelectric coupling in BFO and the interface exchange coupling between BFO and CoFe, respectively. The model is calibrated with experimental results and demonstrate that the switching of the ferromagnet in the

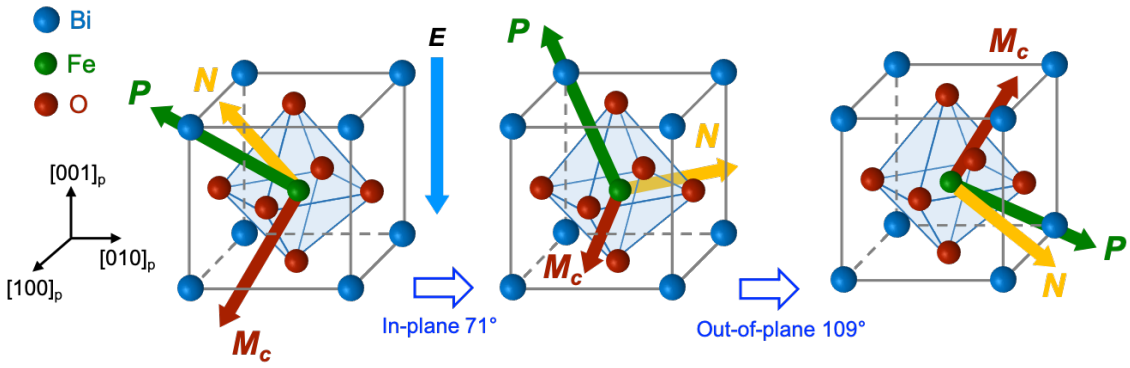

Figure 5.1: The two-step switching process of the FE polarization under an out-of-plane electric field, where $\mathbf{P}$ is the electric polarization, $\mathbf{M_c}$ is the weak magnetization and $\mathbf{N}$ is the Néel vector. The schematic is adapted from [57, 122].

antiferromagnet/ferromagnet heterojunction is caused by the rotation of the Néel vector in the antiferromagnet instead of being driven by the unidirectional exchange bias at the interface as was previously speculated. Moreover, we show that the fundamental limit of the switching time of the ferromagnet is in the subnanosecond regime. The geometric dependence and the thermal stability of the antiferromagnet/ferromagnet heterojunction are also explored. Our simulation results provide the critical metrics and guidelines for designing magnetoelectric devices.

5.2 Theoretical Formalism

Based on the fact that BFO has a perovskite pseudocubic crystal structure, the single domain LK equation is applied to describe the ferroelectric polarization switching dynamics. Recall that the LK equation has the general form given as Eq. (2.1):

$$\rho \frac{\partial \mathbf{P}}{\partial t} = -\frac{\partial f}{\partial \mathbf{P}}, \tag{5.3}$$

where $\mathbf{P}$ is the electric polarization, ρ is the internal resistivity (or viscosity coefficient), f is the thermodynamic free energy density (per unit volume). To accurately describe the deterministic switching paths of BFO under an applied out-of-plane voltage, one needs to

take all possible dominating free energy contributions into consideration.

5.2.1 Bulk free energy

The single domain bulk Landau free energy expanded up to the sixth order with $\mathbf{P} = (P_1, P_2, P_3)$ in the pseudocubic structure has the same form as shown in Eq. (3.6):

$$\begin{aligned} f_{\mathrm{L}} = {} & \alpha_1\big(P_1^2 + P_2^2 + P_3^2\big) + \alpha_{11}\big(P_1^4 + P_2^4 + P_3^4\big) + \alpha_{12}\big(P_1^2P_2^2 + P_2^2P_3^2 + P_1^2P_3^2\big) \\ & + \alpha_{111}\big(P_1^6 + P_2^6 + P_3^6\big) + \alpha_{112}\big[P_1^4\big(P_2^2 + P_3^2\big) + P_2^4\big(P_1^2 + P_3^2\big) + P_3^4\big(P_1^2 + P_2^2\big)\big] \\ & + \alpha_{123}\big(P_1^2P_2^2P_3^2\big). \end{aligned} \tag{5.4}$$

5.2.2 Electric free energy

The electric free energy introduced to the system due to the applied electric field is given as

$$f_{\text{elec}} = -\mathbf{E}_{\text{ext}} \cdot \mathbf{P}, \tag{5.5}$$

where $\mathbf{E}_{\text{ext}}$ is the externally applied field. Note that in this work, the voltage is only applied in the OOP direction and thus, f_{elec} can be simplified as $-|\mathbf{E}_{\text{ext}}|P_3$.

5.2.3 Elastic free energy

Combining first and second law of thermodynamics, a classical description of the internal energy U in a thermodynamic system is in general given by

$$\mathrm{d}U = T\,\mathrm{d}S + \sigma_{ij}\,\mathrm{d}\epsilon_{ij} + E_i\,\mathrm{d}D_i\,, \tag{5.6}$$

where T is temperature, S is entropy, σ_{ij} is a component of the second-rank stress tensor, ϵ_{ij} is the corresponding component of the strain tensor, E_i and D_i are the i_{th} components of electric field and electric displacement, respectively, and, i and j run from one to three in the 3D space. Here, the Einstein convention is used, i.e., repeated indices in a

given term imply summation over the corresponding indices. To represent experimental measurements, thermodynamic potentials are often more convenient to use rather than the internal energy [80]. To describe the strain contribution to the thermodynamics of ferroelectric phase transitions, it is usually more convenient to choose strain and polarization $\mathbf{P} = (P_1, P_2, P_3)$ as independent variables. The appropriate thermodynamic potential for this set of independent variables is then the Helmholtz free energy. Assuming isothermal, its differential form is given by

$$\mathrm{d}F = \sigma_{ij}\,\mathrm{d}\epsilon_{ij} + E_i\,\mathrm{d}P_i\,, \tag{5.7}$$

from which one can obtain the relationship between F and σ_{ij} as $\sigma_{ij} = \frac{\partial F}{\partial \epsilon_{ij}}$.

Recall from Eq. (3.18) that the elastic free energy f_{elas} can be written as

$$\begin{aligned} f_{\text{elas}} =& \frac{1}{2}c_{11}\big(e_{11}^2 + e_{22}^2 + e_{33}^2\big) \\ &+ c_{12}(e_{11}e_{22} + e_{22}e_{33} + e_{11}e_{33}) \\ &+ 2c_{44}\big(e_{12}^2 + e_{23}^2 + e_{13}^2\big). \end{aligned} \tag{5.8}$$

where c_{ij} and e_{ij} are the elastic stiffness and elastic strain defined in Chapter 3.2 [189]. For the strain components parallel to the film surface, the normal strain $\epsilon_{11} = \epsilon_{22} = \mu_{\text{m}}$, where μ_{m} is the misfit strain from the substrate. The shear strain components are assumed to be zero, $\epsilon_{12} = \epsilon_{21} = 0$. Furthermore, by plugging the above expression (Eq. (5.8)) into the stress-free surface condition, i.e., $\sigma_{i3} = \frac{\partial f_{\text{elas}}}{\partial \epsilon_{i3}} = 0$, one can derive the out-of-plane elastic strain conditions for a single domain:

$$\begin{cases} e_{13} = e_{23} = 0, \\ e_{33} = -\frac{c_{12}}{c_{11}}(e_{11} + e_{22}), \end{cases} \tag{5.9}$$

with the corresponding total stains as

$$\begin{cases} \epsilon_{13} = \epsilon_{31} = \epsilon_{13}^0 = Q_{44} P_1 P_3, \\ \epsilon_{23} = \epsilon_{32} = \epsilon_{23}^0 = Q_{44} P_2 P_3, \\ \epsilon_{33} = -2\frac{c_{12}}{c_{11}}\mu_{\mathrm{m}} + \left[\frac{c_{12}}{c_{11}} Q_{11} + \left(\frac{c_{12}}{c_{11}} + 1\right) Q_{12}\right](P_1^2 + P_2^2) + \left(2\frac{c_{12}}{c_{11}} Q_{12} + Q_{11}\right) P_3^2, \end{cases} \tag{5.10}$$

where ϵ_{ij}^0 and Q_{ij} are the stress-free strains and electrostrictive coefficients defined in Chapter 3.2 [190].

5.2.4 Polarization easy plane due to elastic constraints

The experiments from piezoresponse force microscopy (PFM) showed that when the electric field is applied along $[001]_{\mathrm{p}}$ or $[00\bar{1}]_{\mathrm{p}}$ directions, no out-of-plane $71°$ switching path was observed, which contrasts with the conventional perovskite FE such as BTO. It was also found that of the eight possible polarization directions allowed in rhombohedral BFO, only four polarization directions were observed throughout the switching process and all polarization lie in the $[011]_{\mathrm{p}}$ plane, as illustrated in Fig. 5.2. This suggests that under the elastic conditions, only two of the four rhombohedral distortion axes (those contained in the $[011]_{\mathrm{p}}$ plane) would be occupied, which prevents the expected out-of-plane $71°$ switching when applying an electric bias along the [001] direction. As a result, under the OOP electric field, the polarization domain stripe composed of $[1\bar{1}1]_{\mathrm{p}}$ and $[\bar{1}\bar{1}1]_{\mathrm{p}}$ in the as-grown BFO both undergo the two-step switching process: IP $71°$ switching followed by OOP $109°$ switching [57], leading to an overall $180°$ polarization switching. This observation indicated that elastic constraints on the thermodynamically stable polarization directions strongly influence the switching path in the anisotropically strained films. In addition, *ab initio* calculations

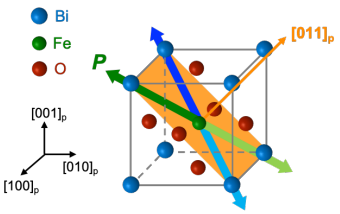

Figure 5.2: Elastic easy plane in the pseudocubic structure of the rhombohedral BFO.

revealed that the OOP 71° switching was not allowed in the two-step switching path. However, by considering only a single ferroelectric domain under the epitaxial strain of the substrate, the lowest-energy switching path occurred in a three-step sequence of 71° switches instead of the two-step process observed in the experiments.

To describe the constrained polarization directions due to the anisotropic strains, we introduce an easy-plane free energy into the energy contributions on the right hand side of Eq. (5.3) as follows:

$$f_{\text{ep}} = K_{\text{strain}}(\mathbf{P} \cdot \mathbf{u})^2, \tag{5.11}$$

where K_{strain} is the elastic strain coefficient and $\mathbf{u} = \left(0, \frac{1}{\sqrt{2}}, \frac{1}{\sqrt{2}}\right)$ is the unit normal to the easy plane. For the easy-plane free energy to be minimized, the polarization is therefore constrained in the $[011]_{\text{p}}$ plane.

5.2.5 Domain wall conductivity and built-in in-plane field

Based on previous experimental studies, domain wall (DW) conduction were found in BFO thin films under an applied voltage [191–196]. 71° ferroelastic domain walls of BFO grown on $SrRuO_3$-buffered $SrTiO_3$ were experimentally shown to provide well-defined conducting paths through the films, from the metallic tip acting as the top electrode to the bottom $SrRuO_3$ electrode. At room temperature, conduction was found to be provided by n-type carriers and the mechanisms for conduction are the same both at the domain walls and at the domains. In the low voltage regime, electrons from defects (oxygen vacancies) are thermally activated near the bottom of the conduction band whereas the current is limited by the ferroelectric polarization. In the high voltage regime, the conducting current is regulated by the Schottky emission of electrons from the top electrode (tip) [191, 197].

For 109° DWs at room temperature, polarization structural changes cause (i) the accumulations of carrier density (oxygen vacancies and associated electrons) to compensate in-plane polarization discontinuity and (ii) a decrease in the bandgap within the

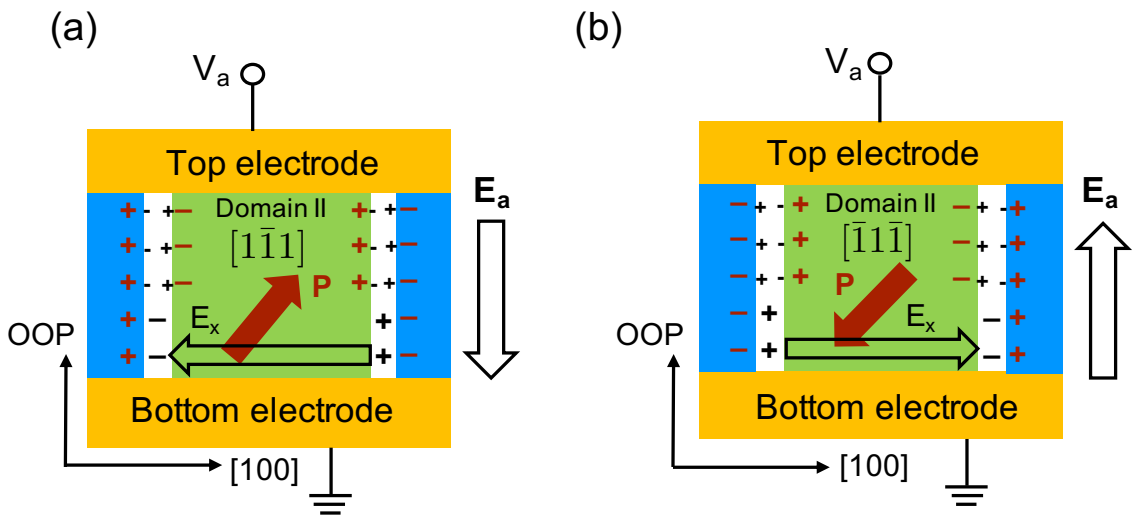

Figure 5.3: The proposed mechanism for the internal in-plane electric field considering the excess screening charged defects or free charge carriers in DWs. Here the domain II stripe is used as an example.

wall [194, 195]. In the low voltage regime, the DW conduction results from the Schottky emission whereas in the high voltage regime, Fowler-Nordheim tunneling dominates the conducting path. When a voltage is applied to the BFO thin films, electrons from the tip (electrode) are injected or tunnel into the DWs. In addition, larger concentrations of oxygen vacancies activated by the applied field lead to an increased current.

In addition, from the atomic-scale experimental characterization and analysis, mobile charged defects that are accumulated in the domain-wall region to screen polarization charges have been proposed as the origin of the electrical conductivity at domain walls in BFO [196]. The defects were identified as Fe^{4+} cations that compensate bismuth vacancies (anions), revealing p-type hopping conduction at domain walls caused by the presence of electron holes associated with Fe^{4+}. Besides, defect accumulation driving force may include electrostatic force and strain-related driving force and DW conductivity can be p-type or n-type depending on the processing conditions. In this work, we assume that the domain wall conduction in BFO thin films is dominated by such defect-mediated mechanisms and that the IP field induced by the charged defects is proportional to the applied field. When a voltage is applied to the BFO, polarization charges are typically

compensated by screening charged defects or free charge carriers inside the DWs. In the meantime, the difference in the polarization near the DW may be screened by the excess charged defects (with an opposite sign) that are diffused or injected toward the DW region, as illustrated in Fig. 5.3. Such defect compensation potentially results in an in-plane electric field that switches the polarization in the IP direction first even if the external voltage is applied in the OOP direction. However, since such a switching mechanism relies on the defects, the deterministic switching may not be robust. Therefore, experiments have found that although most of the domains follow the two-step switching path that can successfully switch the underlying ferromagnet, the devices cannot survive more than three switching cycles due to the motion of ionic species under the large electric field [57].

5.2.6 Magnetization switching dynamics in BFO and CoFe

The dynamics of both BFO and CoFe are solved by the Landau-Lifshitz-Gilbert (LLG) equation:

$$\dot{\mathbf{M}} = -\gamma(\mathbf{M} \times \mathbf{H}_{\text{eff}}) + \frac{\alpha_{\text{G}}}{M_s}\left(\mathbf{M} \times \dot{\mathbf{M}}\right), \tag{5.12}$$

where γ is the electron gyromagnetic ratio, α_{G} is the Gilbert damping factor, M_s is the saturation magnetization of the magnetic material. The total magnetic energy f_{AFM} of BFO includes the exchange energy within BFO, the interface exchange coupling between BFO and CoFe, the bulk anisotropy energy, the anisotropy energy that comes from the epitaxial constraint, and the demagnetization energy. In other words,

$$f_{\text{AFM}} = f_{\text{ex,BFO}} + f_{\text{ex,int}} + f_{\text{ani,bulk}} + f_{\text{ani,epi}} + f_{\text{dem}}, \tag{5.13}$$

and each term in Eq. (5.13) can be expressed as

$$\begin{cases} f_{\text{ex,BFO}} = J_{\text{AFM}}(\nabla \cdot \mathbf{m}_{i,\text{AFM}})^2, \\ f_{\text{ex,int}} = J_{\text{int}} \frac{\mathbf{m}_{i,\text{AFM}} \cdot (\mathbf{m}_{i,\text{AFM}} - \mathbf{m}_{j,\text{FM}})}{\Delta_{ij}^2}, \\ f_{\text{ani,bulk}} = K_{\text{AFM}} \left(\mathbf{m}_{i,\text{AFM}} \cdot \hat{\mathbf{P}} \right)^2, \\ f_{\text{ani,epi}} = K_{\text{epi}} \left(\mathbf{m}_{i,\text{AFM}}^z \right)^2, \\ f_{\text{dem}} = -\frac{1}{2} \mu_0 M_{\text{s,AFM}} (\mathbf{H}_{\text{dem,i}} \cdot \mathbf{m}_{i,\text{AFM}}), \end{cases} \tag{5.14}$$

where J_{AFM} is the exchange stiffness constant of BFO, J_{int} is the interface exchange coupling coefficient between BFO and CoFe, μ_0 is the vacuum permeability, Δ_{ij} is the mesh size in x, y or z direction, and $\mathbf{m}_{i,\text{AFM}} = \mathbf{M}_{i,\text{AFM}}/M_{\text{s,AFM}}$ and $\mathbf{m}_{j,\text{FM}} = \mathbf{M}_{j,\text{FM}}/M_{\text{s,FM}}$ are the unit magnetization vectors of cell i in BFO and cell j in CoFe, respectively. $M_{\text{s,AFM}}$ and $M_{\text{s,FM}}$ are the saturation magnetization of the BFO and CoFe, respectively. K_{AFM} is the bulk anisotropy energy that comes from the DM interaction, K_{epi} is the anisotropy energy along [001], $\hat{\mathbf{P}}$ is the hard axis of the antiferromagnet, and $\mathbf{H}_{\text{dem,i}}$ is the demagnetization field of cell i.

The total magnetic energy f_{FM} of CoFe includes the exchange energy within CoFe, the interface exchange coupling energy at the BFO/CoFe interface, and the demagnetization energy. Similar to Eq. 5.14, the expressions are given as

$$\begin{cases} f_{\text{ex,CoFe}} = J_{\text{FM}}(\nabla \cdot \mathbf{m}_{i,\text{FM}})^2, \\ f_{\text{ex,int}} = J_{\text{int}} \frac{\mathbf{m}_{i,\text{FM}} \cdot (\mathbf{m}_{i,\text{FM}} - \mathbf{m}_{j,\text{AFM}})}{\Delta_{ij}^2}, \\ f_{\text{dem}} = -\frac{1}{2} \mu_0 M_{\text{s,FM}} (\mathbf{H}_{\text{dem,i}} \cdot \mathbf{m}_{i,\text{FM}}), \end{cases} \tag{5.15}$$

where J_{FM} is the exchange stiffness constant of CoFe. Note that the bulk anisotropy energy of CoFe is neglected since CoFe with a thin thickness is amorphous. Moreover, the total free energy on the right hand side of the LK equation includes the FE energy f_{FE} and the

magnetoelectric energy f_{ME}. The magnetoelectric energy f_{ME} of BFO is f_{DMI} defined in Eq. (5.2), where $\mathbf{D}_{ij} = V_0(\mathbf{r}_{ij} \times \mathbf{x}) \approx V_0\hat{\mathbf{P}}$ is the DM vector with the direction parallel to the polarization of the BFO and V_0 is the magnitude of the DMI energy. The total effective magnetic field $\mathbf{H}_{\text{eff}}$ of the magnetic structure in Eq. (5.12) can be calculated from the derivative of the total energy f_{tot} with respect to the magnetization, i.e., $\mathbf{H}_{\text{eff}} = -\frac{1}{\mu_0 M_s}\frac{\partial f_{\text{tot}}}{\partial \mathbf{M}}$.

For the BFO thin film, $\mathbf{H}_{\text{eff}}$ includes the exchange coupling field $\mathbf{H}_{\text{ex}}$, the bulk anisotropy field $\mathbf{H}_{\text{ani}}$ from DMI, the anisotropy field $\mathbf{H}_{\text{epi}}$ from compressive epitaxial constraint, the demagnetization field $\mathbf{H}_{\text{dem}}$, and and the unidirectional DMI field $\mathbf{H}_{\text{DMI}}$, which approximately equals a Zeeman field that creates spin canting in BFO. The direction of $\mathbf{H}_{\text{DMI}}$ is determined by $\mathbf{N} \times \mathbf{D}$ since the Hamiltonian of DMI is expressed as $E_{\text{DMI}} = -\mathbf{D}\cdot\sum \mathbf{M}_i \times \mathbf{M}_j = -\mathbf{D}\cdot\sum \mathbf{N} \times \mathbf{M}_c = \sum \mathbf{H}_{\text{DMI}} \cdot \mathbf{M}_c$, where $\mathbf{H}_{\text{DMI}} = \mathbf{N}\times\mathbf{D}$, $|D| = \beta\mathbf{P}$ and β is the magnetoelectric constant [183]. The Hamiltonian of DMI also shows a right-handed relation between the direction of $\mathbf{P}$, $\mathbf{N}$ and $\mathbf{M}_c$ [185]. The demagnetization field can be expressed as [122]:

$$\mathbf{H}_{\text{dem}} = \frac{-1}{4\pi}\int \frac{\hat{\mathbf{n}}\cdot\mathbf{M}(\mathbf{r}')(\mathbf{r}-\mathbf{r}')}{|\mathbf{r}-\mathbf{r}'|^3}\,\mathrm{d}^2r'\,, \tag{5.16}$$

where $\hat{\mathbf{n}}$ is the surface normal.

Similarly, in the CoFe thin film, the total effective magnetic field includes the exchange coupling field $\mathbf{H}_{\text{ex}}$, the interface exchange coupling field $\mathbf{H}_{\text{int}}$ of the nearest neighbors, and the demagnetization field $\mathbf{H}_{\text{dem}}$. Our unified approach for simulating the ferroelectric and the magnetic dynamics simulation of the BFO/CoFe heterojunction is illustrated in Fig. 5.4.

5.3 Simulation Results

5.3.1 Ferroelectric switching dynamics in BFO

First, we validate the proposed theoretical formalism by simulating the electric polarization switching dynamics with a voltage applied in the OOP direction. Based on the free energy

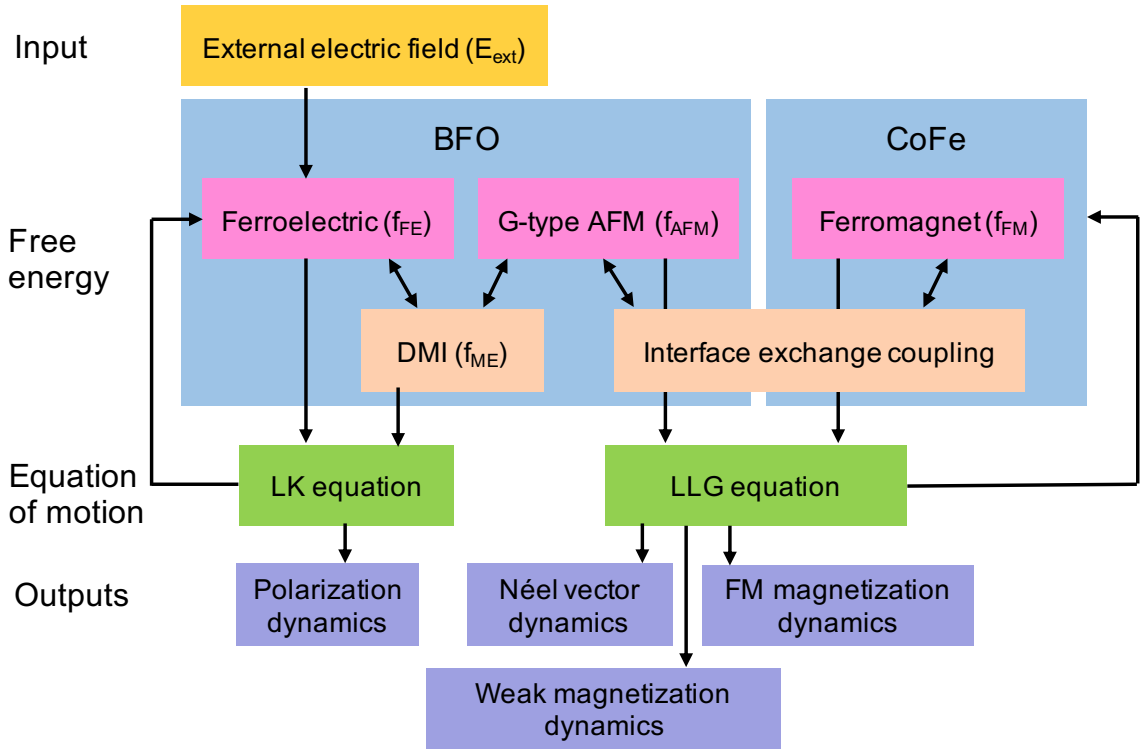

Figure 5.4: Modeling framework for BFO/CoFe heterojunctions. The input voltage applied to the BFO updates the ferroelectric energy in BFO. The antiferromagnetic energy of the two sublattices 1 and 2 in BFO changes according to the polarization order because of the DMI. Next, the ferromagnetic energy of CoFe also changes because of the interface exchange coupling between the antiferromagnetic order in BFO and the magnetic order in CoFe.

description discussed in Sec. 5.2, Eq. (5.3) can be rewritten as

$$\begin{cases} \frac{\partial P_1}{\partial t} = -L\left(\frac{\partial f_{\mathrm{L}}+f_{\mathrm{elas}}+f_{\mathrm{ep}}}{\partial P_1} - \frac{\mathrm{sgn}(V_{\mathrm{a}})}{W_{\mathrm{d}}}\right), \\ \frac{\partial P_2}{\partial t} = -L\left(\frac{\partial f_{\mathrm{L}}+f_{\mathrm{elas}}+f_{\mathrm{ep}}}{\partial P_2}\right), \\ \frac{\partial P_3}{\partial t} = -L\left(\frac{\partial f_{\mathrm{L}}+f_{\mathrm{elas}}+f_{\mathrm{ep}}}{\partial P_3} - \frac{V_{\mathrm{a}}}{d} + 2KP_3\right), \end{cases} \tag{5.17}$$

where $L = 1/\rho$ is the domain kinetic coefficient, W_{d} is the effective domain wall width, and $K = 1/(\epsilon_0 + t_{\mathrm{FE}}/(\lambda_1/\epsilon_1/\epsilon_0 + \lambda_2/\epsilon_2/\epsilon_0))/\kappa$ and $d = t_{\mathrm{FE}} + \lambda_1/\epsilon_1 + \lambda_2/\epsilon_2$ are a constant and effective film thickness, respectively, that account for the finite screening lengths $\lambda_{1,2}$ (and depolarization) in a metal-FE-metal capacitor [45]. With an OOP voltage in Fig. 5.5(a) applied to the BFO thin film, Figs. 5.5(c) and (d) show the simulated polarization dynamics

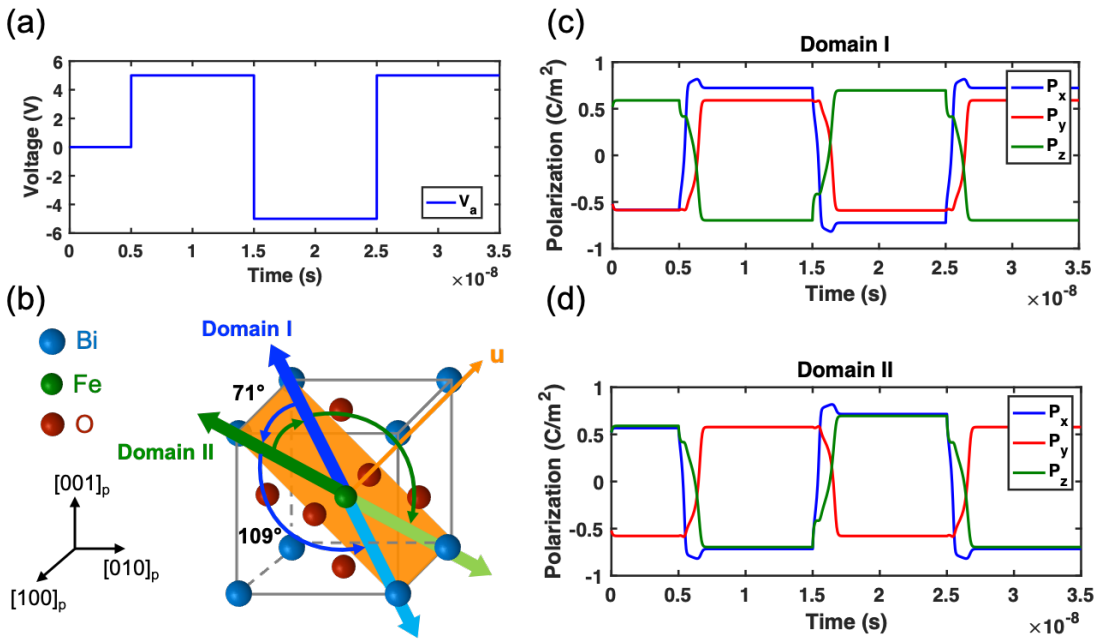

Figure 5.5: (a) The voltage waveform applied to the BFO film in the OOP (z) direction in the simulation. (b) The schematic of the two-step switching path of the two domains under the applied OOP voltage. (c) and (d) The simulated FE polarization switching dynamics with HSPICE, showing both domain I (c) and domain II (d) undergo the two-step switching process: an IP 71° switch followed by an OOP 109° switch.

of BFO. For $[\bar{1}\bar{1}1]$ in domain I, P_x switches first (IP 71° switch) and then P_y and P_z switch simultaneously (OOP 109° switch). Similarly, $[1\bar{1}1]$ in domain II follows the same switching path. Such a two-step 180° switching path for both domain configurations is illustrated in Fig. 5.5(b).

5.3.2 Deterministic switching dynamics of BFO/CoFe heterojunctions

With the unified ferroelectric and magnetic simulation framework, the interface exchange interaction and the magnetic order at the interface between BFO and CoFe thin films are investigated by the micromagnetic simulations. We define the Néel vector and the weak magnetization of BFO as $N \equiv (M_1 - M_2)/(|M_1| + |M_2|)$ and $M_c \equiv (M_1 + M_2)/(|M_1| + |M_2|)$, respectively, where M_1 and M_2 are the magnetization vectors of sublattices 1 and 2 in BFO. The magnetization of CoFe is expressed as M_{FM}. The interface exchange coupling field is calculated by the Heisenberg exchange coupling field

between magnetic cells of BFO and CoFe thin films with coefficient J_{int}. Note that the interface exchange coupling field considered here is a direct coupling field between BFO and CoFe layers, which is inversely proportional to the square of the distance between cells of BFO and CoFe at the interface.

To extract the interface exchange coupling coefficient J_{int} from experimental data, we simulate a stripe-domain 30-nm thick BFO and 2-nm thick CoFe bilayer thin film, as shown in Fig 5.6. Similar to the experiments [57], the lateral dimensions are $5\,\mu\text{m}$ long and $2\,\mu\text{m}$ wide. We sweep the external magnetic field from -300 to $300\,\text{Oe}$ and check the magnetic hysteresis (M-H) loop of the BFO/CoFe heterojunction. Our simulation results using $J_{\text{int}} = 0.32\,\text{pJ/m}$ is in good agreement with the experimental data.

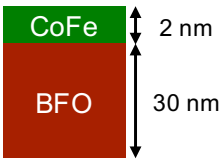

Figure 5.6: BFO/CoFe bilayer structure considered in this work.

Next, we investigate the dynamics of a single-domain 30-nm thick BFO and 2-nm thick CoFe bilayer thin films. To check the magnetization dynamics of CoFe because of the interface exchange coupling from BFO, we set the width and length of the bilayer thin films equal to $20\,\text{nm}$ such that the shape anisotropy energy in CoFe is negligible. We renormalize the magnetic parameters of BFO and J_{int} with smaller mesh size to simulate a scaled device. Theoretically, the dynamics of CoFe is determined by the magnetization rotation in BFO because of the interface exchange coupling between $\mathbf{M_c}$ and $\mathbf{M}_{\text{FM}}$. To simulate the dynamics of both BFO and CoFe, we use the previously developed modeling framework for a single-domain BFO in which the dynamics of $\mathbf{P}$, $\mathbf{N}$, and $\mathbf{M_c}$ are calculated by considering the rotation of the magnetic easy plane along with the polarization [122, 188]. The schematics of vectors $\mathbf{P}$, $\mathbf{N}$, $\mathbf{M_c}$, $\mathbf{M_1}$, $\mathbf{M_2}$ and $\mathbf{M}_{\text{FM}}$ in the BFO/CoFe heterojunction are shown in Fig. 5.7(a). Figure 5.7(b) shows that when the applied electric field is larger than the threshold field of BFO, the polarization of BFO switches $180°$ as calculated by the LK equation (Eq. (5.3)). Similar to the case of the single-domain BFO, we see that $\mathbf{N}$ switches $180°$, whereas Mc does not, as shown in Fig. 5.7(d), (e). This means that

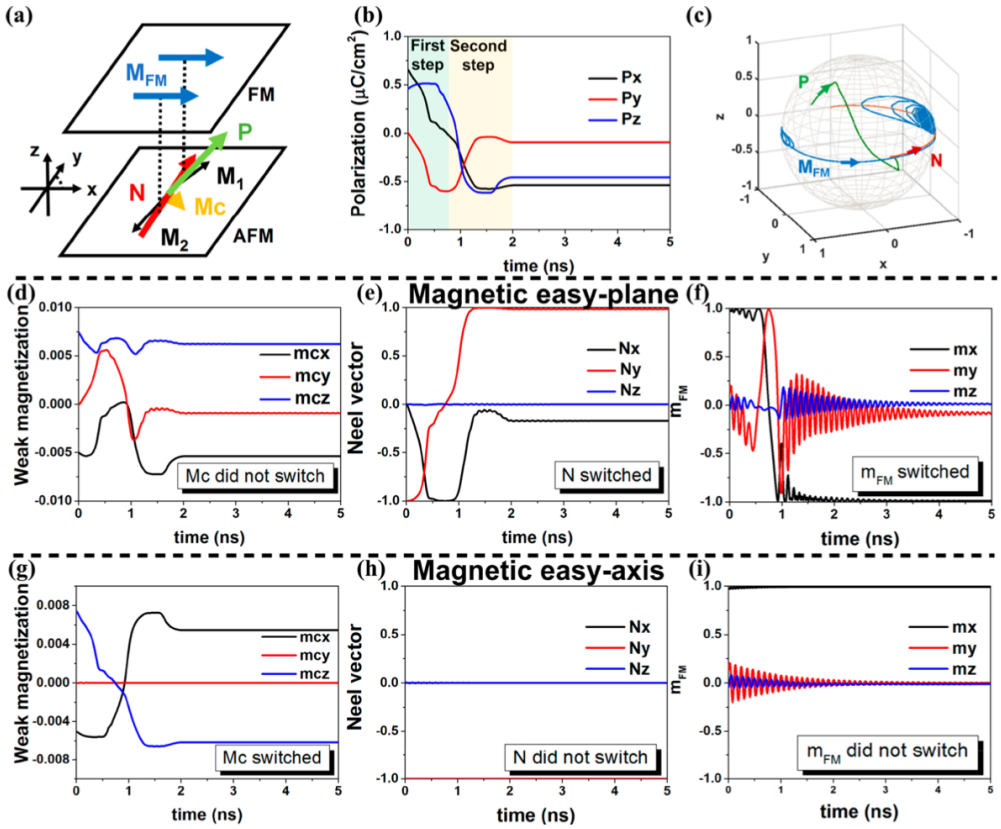

Figure 5.7: (a) Schematics of the polarization ($\mathbf{P}$), the Néel vector ($\mathbf{N}$), the weak magnetization ($\mathbf{M_c}$), the magnetization of the two sublattices in BFO ($\mathbf{M}_1$, $\mathbf{M}_2$), and magnetization of ferromagnet ($\mathbf{M_{FM}}$) in the BFO/CoFe heterojunction. (b) Dynamics of $\mathbf{P}$ after applying a negative electric field across the BFO/CoFe heterojunction. To verify the dominant factor of magnetization switching in CoFe, we consider two scenarios for the magnetic state in BFO: (d-f) magnetic easy plane and (g-i) magnetic easy axis. For the case of the magnetic easy plane, although (d) $\mathbf{M_c}$ does not switch, both (e) $\mathbf{N}$ and (f) $\mathbf{M_{FM}}$ switch $180°$ after $\mathbf{P}$ switches. (c) The switching trajectories of $\mathbf{P}$, $\mathbf{N}$, and $\mathbf{M_{FM}}$ during time evolution for the case of the magnetic easy plane in BFO. For the case of the magnetic easy axis, (g) $\mathbf{M_c}$ switches $180°$; however, both (h) $\mathbf{N}$ and (i) $\mathbf{M_{FM}}$ in the BFO/CoFe heterojunction do not switch. (Adapted from and by courtesy of [58].)

the two sublattices $\mathbf{M}_1$ and $\mathbf{M}_2$ in BFO both switch $180°$ after the polarization switching. Figures 5.7(b), (d), (e) also show that the vectors of $\mathbf{P}$, $\mathbf{N}$, and $\mathbf{M_c}$ form a right-handed system.

In addition, Fig. 5.7(f) shows that $\mathbf{M}_{\mathrm{FM}}$ switches $180°$ after the polarization reversal, and there exists an intermediate stage when $\mathbf{M}_{\mathrm{FM}}$ rotates $90°$. Note that the magnetic vectors $\mathbf{M}_1$, $\mathbf{M}_2$ and the corresponding $\mathbf{N}$ in BFO are almost orthogonal to $\mathbf{M}_{\mathrm{FM}}$ to achieve

the lowest energy state. This result is rather interesting, as it has been argued before that the magnetization reversal in CoFe mainly comes from the exchange bias between $\mathbf{M_c}$ and $\mathbf{M}_{\mathrm{FM}}$. However, our simulation results indicate that the main driving force is the rotation of $\mathbf{N}$ rather than the rotation of $\mathbf{M_c}$, because $|\mathbf{M_c}|$ is much smaller than $|\mathbf{N}|$. To verify the statement that the rotation of $\mathbf{N}$ governs the switching behavior of $\mathbf{M}_{\mathrm{FM}}$, we consider two BFO switching scenarios: (i) the magnetic easy plane rotates with the magnetic hard axis parallel to $\mathbf{P}$, and (ii) the magnetic easy axis of BFO is fixed, but the DM field switches $180°$ in the direction of $\mathbf{P} \times \mathbf{N}$.

In case (i), Figs. 5.7(d)-(f) show that when $\mathbf{N}$ switches $180°$, $\mathbf{M}_{\mathrm{FM}}$ successfully rotates $180°$ after polarization reversal, whereas $\mathbf{M_c}$ remains unswitched. The switching trajectories of $\mathbf{P}$, $\mathbf{N}$, and $\mathbf{M_c}$ in case (i) are shown in Fig. 5.7(c). On the contrary, in case (ii), when $\mathbf{N}$ is fixed during polarization reversal, $\mathbf{M_c}$ switches but neither $\mathbf{M}_{\mathrm{FM}}$ nor $\mathbf{N}$ switch, as shown in Fig. 5.7(g)-(i). Here $\mathbf{M}_1$ and $\mathbf{M}_2$ only slightly change their tilting direction by $180°$, whereas the y component (easy-axis direction) remain fixed. Therefore, we believe that the magnetic switching of $\mathbf{M}_{\mathrm{FM}}$ is initiated by the switching of $\mathbf{P}$, and then driven by the rotation of $\mathbf{N}$ rather than $\mathbf{M_c}$ since only when both $\mathbf{M}_1$ and $\mathbf{M}_2$ rotate $180°$, magnetic cells of FM at the interface can rotate simultaneously through the interface exchange coupling between BFO and FM.

Next, to evaluate the potential application of the BFO/CoFe heterojunction in logic/memory operations, we check the sensitivity of BFO polarization switching time (τ_{FE}) that may affect the magnetization switching success rate and the magnetization switching time of CoFe. Note that varying τ_{FE} of the BFO corresponds to various viscosity coefficients in the LK equation under a fixed electric field. τ_{FE} can be as fast as a few picoseconds as calculated from the theory [198] and projected from the experiment [199].

In our previous study, we have shown that the theoretical limit of the switching time of $\mathbf{N}$ in BFO is $30\,\mathrm{ps}$; therefore, the antiferromagnetic order of BFO can follow the rotation of the polarization. For a BFO/CoFe heterojunction with $L = 40\,\mathrm{nm}$, $W = 20\,\mathrm{nm}$, and

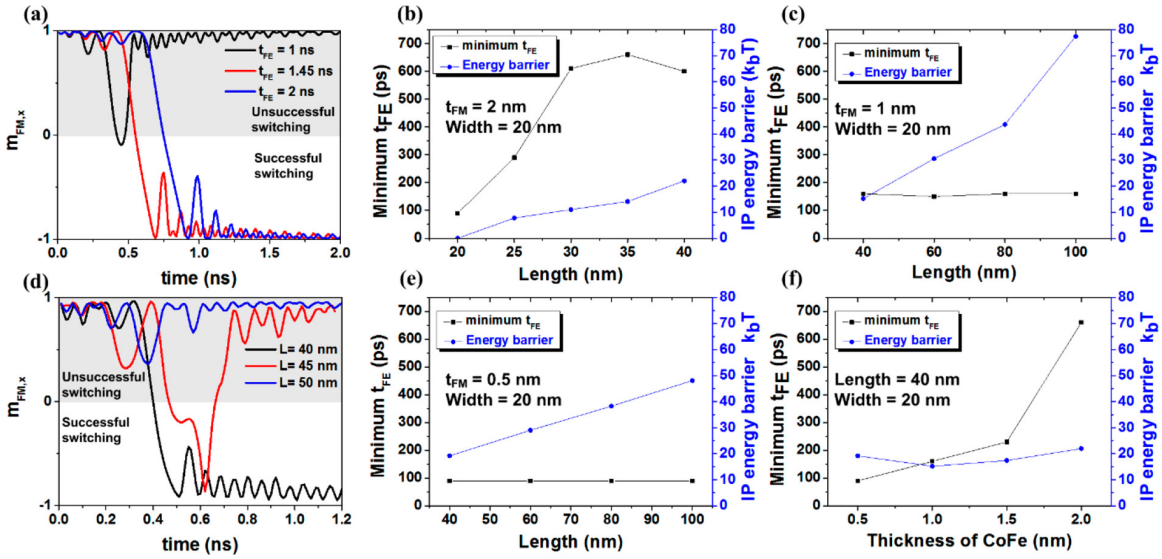

Figure 5.8: (a) Minimum ferroelectric switching time (τ_{FE}) for successful magnet switching in the BFO/CoFe heterojunction is $1.45\,\text{ns}$ when $L = 40\,\text{nm}$, $W = 20\,\text{nm}$, and the thickness of BFO and CoFe are 30 and $2\,\text{nm}$, respectively. The minimum τ_{FE} of CoFe and the in-plane energy barrier of the BFO/CoFe heterojunction with varying lengths of the device when the thickness of CoFe is (b) 2, (c) 1, and (e) $0.5\,\text{nm}$. (f) Minimum τ_{FE} of CoFe and the in-plane energy barrier of the BFO/CoFe heterojunction with varying thicknesses of CoFe when length is $40\,\text{nm}$ and width is $20\,\text{nm}$. (d) Magnetization switching of CoFe in the BFO/CoFe heterojunction fails under a longer length ($L \geq 45\,\text{nm}$) when $W = 20\,\text{nm}$. Adapted from and by courtesy of [58].

$30\,\text{nm}$ thick BFO and $2\,\text{nm}$ thick CoFe, Fig. 5.8(a) demonstrates that when τ_{FE} is shorter than $1.45\,\text{ns}$, the rotation of $\mathbf{N}$ is too fast for $\mathbf{M}_{\text{FM}}$ to follow and thus, the switching of $\mathbf{M}_{\text{FM}}$ failed. This is because the switching time of $\mathbf{M}_{\text{FM}}$ follows the input switching time of $\mathbf{N}$. When τ_{FE} is shorter than the inverse of the precession frequency of FM, the switching of $\mathbf{M}_{\text{FM}}$ fails. Similarly, when τ_{FE} is larger than the minimum τ_{FE} for successful magnet switching ($\tau_{\text{FE,min}}$), increasing τ_{FE} increases the switching time of $\mathbf{N}$, $\mathbf{M}_c$, and thus $\mathbf{M}_{\text{FM}}$. Therefore, Fig. 5.8(a) shows that the theoretical lower bound for MFM switching is $1.45\,\text{ns}$ when $L = 40\,\text{nm}$, $W = 20\,\text{nm}$, and CoFe is $2\,\text{nm}$ thick. However, $\tau_{\text{FE,min}}$ of the BFO/CoFe heterojunction may not be a constant value because $\tau_{\text{FE,min}}$ depends on the strength of the interface exchange coupling between BFO and CoFe and the in-plane energy barrier of the device. Furthermore, if the in-plane energy barrier becomes even larger compared to the interface exchange coupling energy, the switching of CoFe fails. Fig. 5.8(b) shows that

when the length of the $20\,\mathrm{nm}$ wide BFO/CoFe heterojunction increases from 40 to 45 or $50\,\mathrm{nm}$, the switching of CoFe fails because the average interface exchange coupling field remains unchanged, whereas the in-plane energy barrier increases with increasing length of the device.

To examine the $\tau_{\mathrm{FE,min}}$ dependency on different energy barriers in the BFO/CoFe heterojunction or different strength of the interface exchange coupling in CoFe, we consider two scenarios: (A) varying the aspect ratio of the device and (B) varying the thickness of the CoFe layer under a fixed width ($20\,\mathrm{nm}$) of the BFO/CoFe heterojunction and a fixed thickness of BFO ($30\,\mathrm{nm}$). For case A, Figs. 5.8(b), (c), (e) show the relation between $\tau_{\mathrm{FE,min}}$ and the varying aspect ratios of the BFO/CoFe bilayer. The minimum τ_{FE} for successful magnet switching increases as the aspect ratio of the device increases because of the larger energy barrier. In other words, the overdrive field for the CoFe layer decreases if the aspect ratio of the device is increased. However, $\tau_{\mathrm{FE,min}}$ will become less dependent on the aspect ratio when the thickness of the CoFe decreases below $1\,\mathrm{nm}$. This is because the interface exchange coupling field becomes dominant compared to the intrinsic exchange coupling field and the in-plane energy barrier in a thin CoFe layer. Therefore, for case B, when the thickness of the CoFe is varied from 0.5 to $2\,\mathrm{nm}$, $\tau_{\mathrm{FE,min}}$ monotonically increases because of the weaker interface exchange coupling averaged in the CoFe, as shown in Fig. 5.8(f). These time-dependent magnetization switching cases show that $\tau_{\mathrm{FE,min}}$ in the BFO/ CoFe heterojunction is $90\,\mathrm{ps}$ when the CoFe is as thin as $0.5\,\mathrm{nm}$, and the magnitude of the average interface exchange coupling field decreases with increasing CoFe thickness as shown in the Supporting Information for [58]. To be more specific, when the thickness of CoFe increases from 1.5 to $2\,\mathrm{nm}$, $\tau_{\mathrm{FE,min}}$ drastically increases from 230 to $660\,\mathrm{ps}$.

To study the thermal stability of the device, we check the magnetic energy barrier of the $20\,\mathrm{nm}$ wide single-domain BFO/CoFe thin film with varying device lengths and CoFe layer thicknesses. Because our calculations show that the out-of-plane (OOP) energy barrier is much larger than the in-plane (IP) energy barrier because of the strong shape anisotropy

energy, we will only discuss the IP energy barrier in the following section. When the thickness of the CoFe layer is $2\,\mathrm{nm}$, the IP energy barrier increases from 0 to $23\ k_{\mathrm{B}}T$ when the length increases from 20 to $40\,\mathrm{nm}$, as shown in Fig. 5.8(b). These energy barriers are too small for memory applications that usually require energy barriers larger than 60 or $70\ k_{\mathrm{B}}T$ for retention times greater than 10 years. When the thickness of CoFe is $1\,\mathrm{nm}$, the energy barrier of the BFO/CoFe bilayer is as large as $77.4\ k_{\mathrm{B}}T$ in the $100\,\mathrm{nm}$ long BFO/CoFe bilayer, as seen in Fig. 5.8(c). However, when the thickness of CoFe is reduced to $0.5\,\mathrm{nm}$ in the $100\,\mathrm{nm}$ long BFO/CoFe bilayer, the IP energy barrier decreases to $48\ k_{\mathrm{B}}T$ because of the reduced volume of CoFe. Therefore, a $1\,\mathrm{nm}$ thick FM layer and a high length to width aspect ratio is suitable for the BFO/CoFe heterojunction to ensure a high IP energy barrier.

To investigate the thermal stability and switching reliability of the device, we check the probability of successful switching in the BFO/CoFe heterojunction with varying aspect ratios and thicknesses of CoFe. The probability of successful switching (P_{sw}) is obtained by simulating the polarization and the magnetization switching dynamics of the BFO/CoFe heterojunction for 20 tests. The details of the micromagnetic simulation with thermal noise are explained in Supporting Information for [58]. Our results show that P_{sw} is only 50% in the 20 tests when CoFe is $2\,\mathrm{nm}$ thick and $L = 40\,\mathrm{nm}$, However, for the case of $1\,\mathrm{nm}$ thick CoFe with $L = 100\,\mathrm{nm}$, we observe that P_{sw} is 100% in these 20 tests because of the stronger interface exchange coupling effect between BFO and thin CoFe layer. From the above analysis of varying $\tau_{\mathrm{FE,min}}$, IP energy barrier and P_{sw}, our results show that the thermal stability and the magnet switching time of the BFO/CoFe heterojunction depend on the proper design of the aspect ratio and the thickness of the CoFe layer. Generally, both a faster magnetization switching (smaller $\tau_{\mathrm{FE,min}}$) and a high switching success rate are obtained from thinner CoFe films. On the other hand, when the aspect ratio is 5, the energy barrier will greatly decrease as the thickness of CoFe reduces from 1 to $0.5\,\mathrm{nm}$, because the energy barrier depends on the volume of the ferromagnet. Therefore, a BFO/CoFe

Table 5.1: Ferroelectric Parameters Used in This Work

Parameter	Value
t_{FE} (nm)	30
κ	40
L $(\Omega\text{m})^{-1}$	200
$\epsilon_{1,2}$	8.45
$\lambda_{1,2}$ (Å)	0.8
W_{d} (nm)	$1.5t_{\text{FE}}$
α_1 (m/F)	$4.9(T - 1103) \times 10^5$
α_{11} $(\text{m}^5\text{C}^{-2}/\text{F})$	2.29×10^8
α_{12} $(\text{m}^5\text{C}^{-2}/\text{F})$	3.06×10^8
α_{111} $(\text{m}^9\text{C}^{-4}/\text{F})$	5.99×10^7
α_{112} $(\text{m}^9\text{C}^{-4}/\text{F})$	-3.34×10^5
α_{123} $(\text{m}^9\text{C}^{-4}/\text{F})$	-1.78×10^8
c_{11} (N/m^2)	3.02×10^{11}
c_{12} (N/m^2)	1.62×10^{11}
c_{44} (N/m^2)	0.68×10^{11}
Q_{11} (m^4/C^2)	0.032
Q_{12} (m^4/C^2)	-0.016
Q_{44} (m^4/C^2)	0.02
μ_{m}	-0.0035
K_{strain} (N/m^2)	6×10^8

heterojunction with a $1\,\text{nm}$ thick CoFe and a high aspect ratio seems to be the most promising option in terms of thermally stable and error-free operation. The parameters used in the ferroelectric model are shown in Table 5.1 for reference, and other magnetic parameters can be found in the Supporting Information for [58].

5.4 Summary

Based on the experimental observations, we have established a theoretical model to describe the deterministic switching path of the electric polarization in multiferroic

$BiFeO_3$[1]. Due to the rhombohedral crystal structure of perovskite BFO, the elastic free energy and easy-plane free energy play a key role in constraining the polarization in the same crystal plane. Furthermore, even if the external field is applied in the out-of-plane direction, the charged defects in the domain walls may induce an internal in-plane electric field, which initiates an IP 71° switch first during polarization reversal. By incorporating the polarization switching and the ME effect, a unified simulation framework for AFM/FM heterojunctions is developed and used to model the magnetic structure and the dynamics of a single-domain BFO/CoFe heterojunction. To evaluate the interface properties and determine the value of J_{int}, we model the experimentally measured magnetic hysteresis loop and giant magnetoresistance (GMR) curve traces and find that J_{int} is approximately $0.32\,\mathrm{pJ/m}$. Using this experimentally extracted J_{int}, we further simulate the dynamics of BFO/CoFe heterojunction and prove that the driving force of $\mathbf{M_{FM}}$ switching is determined by the rotation of $\mathbf{N}$ rather than the rotation of $\mathbf{M_c}$.

In addition, such a physics-based compact model allows us to analyze sensitivity of the switching success rate of the BFO/CoFe heterojunction with varying polarization switching times. The minimum τ_{FE} of a successful switching depends on the aspect ratio of the device and the thickness of the CoFe layer. It is found that a smaller $\tau_{\text{FE,min}}$ can be obtained by a thinner CoFe thin film. Last, the thermal noise effect of this BFO/CoFe heterojunction is included to evaluate the thermal stability and the probability of successful switching for its further applications at room temperature. Our simulation results show that for a BFO/CoFe heterojunction with a thinner FM thin film ($\sim 1\,\mathrm{nm}$), we can increase the aspect ratio to about 5 to ensure both high thermal stability and switching reliability. The results of this work are important for understanding and designing magnetoelectric devices.

[1]This work was done in collaboration with Yu-Ching Liao and *Intel Corporation*. The ferroelectric switching dynamics of BFO was developed and verified by Chia-Sheng, and the rest of the simulations were performed by Yu-Ching.

CHAPTER 6
CONCLUSION AND FUTURE DIRECTIONS

In the relentless pursuit of Moore's law, device scaling down to the nanometer regime has gradually come to a bottleneck due to the fact that the power dissipation in microchips becomes a more and more challenging concern. Therefore, emerging technologies beyond-CMOS are in urgent need of development. Among a large number of proposed emerging nanoelectronic devices, we primarily focus our research attention on the negative capacitance (NC) phenomenon in ferroelectrics and the magnetoelectric (ME) effect in multiferroics for low power device applications in this thesis.

A stack structure consisting of a ferroelectric (FE) layer and a dielectric (DE) layer was proposed to achieve voltage amplification in the DE layer. The physical concept behind this mechanism is that the metastable NC state arising from the double-well energy profile of the FE can be stabilized by the DE layer in terms of the total free energy of the device. Such a proposal may provide a potential way to significantly improve the subthreshold swing of conventional CMOS transistors at room temperature. To assess the potential application of the NC effect, we first implement a physics-based circuit-compatible model of single domain ferroelectric materials for the study of the performance of negative capacitance field-effect transistors at the device and circuit levels. The single domain FE model is further extended to a multi-domain model by adopting the phase field formalism to capture the polycrystalline nature of FE films. For realistic logic device applications, however, the physical mechanisms behind the experimental observation of hysteresis-free NC behaviors have not yet been clear. Therefore, we have dedicated our research efforts to the study of such a key phenomenon for the realization of ultra-low power NC field effect transistors. Moreover, the deterministic magnetic switching driven by an applied voltage is of great importance to achieve low-power spintronic devices. The unique two-step

switching process found in rhombohedral bismuth ferrite leads to the voltage-driven $180°$ deterministic magnetic switching with the magnetoelectric effect. With proper free energy contributions included to describe the experimentally observed FE polarization switching dynamics, a unified micromagnetic/ferroelectric simulation framework is developed to model the deterministic switching dynamics and thermal stability of the single-domain BFO/CoFe heterojunction. Lastly, the trapped charge dynamics in ferroelectric field effect transistors, which is the major reliability concern for the memory device realization, is under investigation.

Despite all the experimental and theoretical efforts to explore the material characteristics of ferroelectrics and their promising applications in beyond-CMOS devices, both the studies of fundamental physical mechanisms and the realization of proposed novel devices are still underway in order to get a better picture of how FE materials can provide an alternative pathway for the relentless downscaling of semiconductor devices. Therefore, it is of great importance to theoretically investigate physical characteristics of FEs while the attempts to realize commercial FE-based emerging devices are being carried out. The potential applications of FE-based emerging devices in low-power logics and nonvolatile memories are shown in Fig. 6.1 as a guideline for future research. As active participants in technology development (TD), we summarize the key research contribution and provide future directions to the related research communities.

6.1 Research Contribution

In Chapter 1, we give a comprehensive introduction to the CMOS transistor scaling that advances the technologies and changes the daily life in a revolutionary way. After the relentless pursuit of Moore's Law for more than half a century, the transistor size is scaled down to the nanometer regime, however, with more and more challenges showing up. The limitation, which motivates the active development of beyond-CMOS devices, includes the physical dimension, power and process technology. In addition to the efforts to further

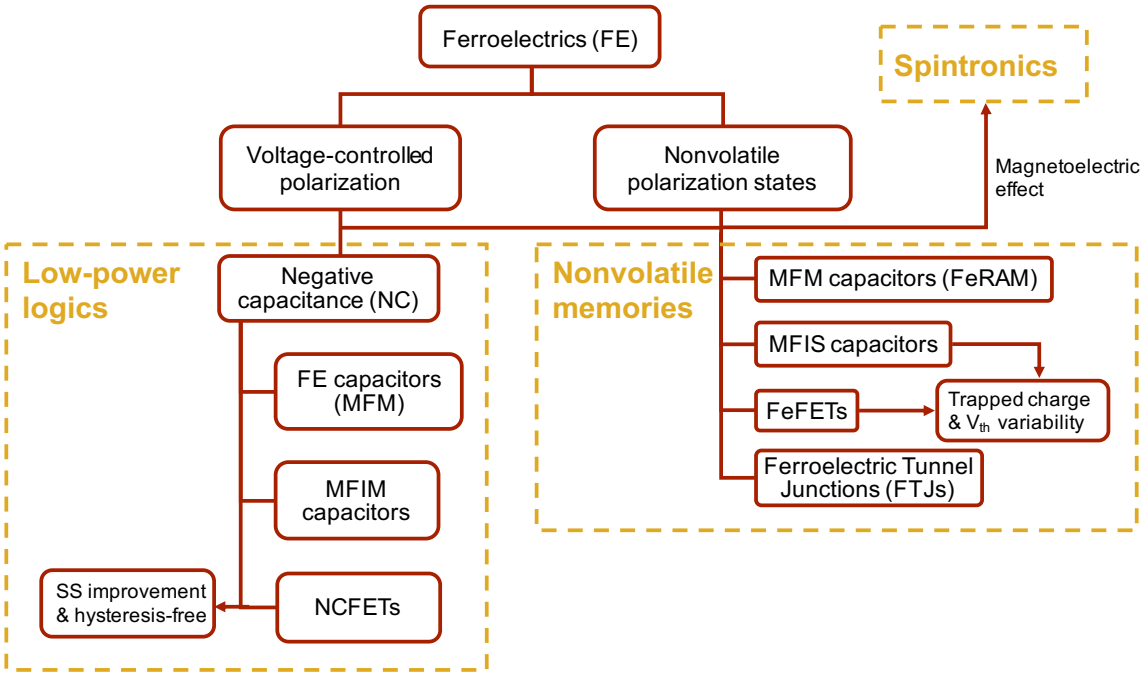

Figure 6.1: Potential applications of FE-based emerging devices in low-power logics and nonvolatile memories.

improve the transistor scaling, a large number of emerging devices have been proposed based on experimental findings and theoretical concepts. In this thesis, we mainly focus on the potential applications of ferroelectric materials and the ferroelectricity associated with mutliferroic materials. Important physical concepts and key emerging devices are presented to provide the readers with a general picture of the current research progress on ferroelectric-based and magnetoelectric devices. Moreover, an overview of this thesis is given to highlight the research contributions in each chapter.

In Chapter 2, for the purpose of larger circuit analyses, we implement a physical model with HSPICE and Verilog-A based on the single-domain phenomenological formalism and experimental measurements for the study of the dynamic NC effect in FE film layers and the device-circuit co-optimization of NC field effect transistors. Using such a circuit-compatible compact model, we study the performance of internally resistive NCFETs at the circuit level, including NANDs and repeaters in long interconnects. We discuss key aspects of NCFET characteristics that are fundamentally important to FE-based

circuit designs and simulations. To properly initialize NCFET-based circuits, the supply voltage needs to be turned on during the simulations. Our analysis shows that the NC effect suppresses the leakage current of NCFETs when they are off. Therefore, lowering the threshold voltage of the transistors is proposed to balance the performances of NCFET-based devices at a wide range of activity factors. We also find that a large viscosity coefficient has a smaller impact on NCFET NANDs with larger fan-ins because the FE layers in various NCFETs switch in parallel. A similar trend is observed for repeaters when the RC delay of the wire is dominant compared to the switching time of FE layers. Moreover, we observe optimal numbers and sizes of repeaters that minimize the EDP compared to the interconnects using conventional CMOS devices. Our analysis provides useful insights into the effects of key NCFET parameters for advanced low-power circuit design. This work was published in *IEEE Electron Device Letters* [118].

In Chapter 3, the single domain approximation used in Chapter 2 is extended to a multi-domain model by introducing the domain wall free energy into the thermodynamic potential to further investigate the multi-domain nature of polycrystalline FE. We develop a physics-based phase field framework that takes into account bulk Landau free energy, gradient free energy, electric free energy and elastic free energy. By including electrostatic boundary conditions from top and bottom metal contacts for the depolarization effect, our simulation results for the as-grown domain configuration show a strong agreement with experimental observations, where depolarization suppresses the average polarization with a stripe domain pattern forming. More importantly, with the comprehensive multi-domain phase field framework, the crucial role phenomenological parameters play in FE domain evolution and switching dynamics can be explored based on experimental measurements. Implementing the phase field model in a circuit-compatible manner, we investigate the effect of domain interaction on the transient responses of HZO capacitors under a voltage pulse in an RFEC circuit. FE domain interaction is found to depend on the applied voltage and plays an important role in the dynamic responses of polarization switching

and the transient NC effect. We show that the effect of domain interaction cannot be viewed as an effective electric field because domain interaction affects the total free energy curvature. As the domain interaction becomes stronger and stronger, the negative curvature of free energy around zero polarization turns positive. Therefore, the voltage-dependent domain interaction indicates that FE-DE capacitance matching can only be achieved at a specific voltage and frequency. Moreover, the dynamic nature of FE domain viscosity at a voltage pulse is explored based on the experimental measurements. This article explores the physical roles that phenomenological parameters play in microscopic switching mechanisms for multi-domain HZO capacitors with a circuit model that shows the potential for the analyses of HfO_2-based FEs at device and circuit levels. In collaboration with *Intel Corporation*, this work was published in *IEEE Transactions on Electron Devices* [166].

In Chapter 4, we present a physical picture for a better understanding of the hysteresis-free charge-boost effect observed experimentally in MFIM capacitors. We first show that by introducing the DE leakage and interfacial trapped charges, the experimentally measured hysteresis loop of MFM capacitors can be well described by the Landau formalism, suggesting the existence of an interfacial oxide layer at the FE-metal interface in MFM capacitors. With the proposed DE leakage and trapped charge mechanisms included, we establish a physical model for MFIM capacitors. Based on the pulse-switching measurements, we find that the charge enhancement and hysteresis behaviors can be directly attributed to the FE intrinsic domain viscosity and DE leakage, respectively. In addition, the phenomenological kinetic coefficients extracted from the charge responses are found to be linked to the well-known Merz's law in the NC region. By analyzing the thermodynamic free energy profile during polarization reversal, our simulation results suggest that the experimentally observed hysteresis-free capacitance enhancement of MFIM may be caused not by the alleged NC stabilization and capacitance matching but by the fact that the FE polarization is not fully switched during the short pulse measurement. With a thinner DE layer, the MFIM capacitor exhibits hysteresis

because the FE polarization can be fully switched to the other state with the help of larger DE leakage and compensating trapped charges. Furthermore, the possible cause of the experimentally observed residual charges may be explained by the transient responses of trapped charges existing at the FE-DE interface. The physical interpretation presented in this work can provide useful insights into the NC effect in MFIM capacitors and future studies of low-power logic transistors. In collaboration with *Intel Corporation*, this work was published in *Physical Review Applied* [200].

In Chapter 5, we develop a physics-based compact model to describe the polarization switching dynamics of a single-domain $BiFeO_3$ under an out-of-plane voltage based on experimental findings. With such a circuit model, the magnetic structure and the dynamics of a single-domain $BiFeO_3$/CoFe heterojunction is studied. The experimentally measured magnetic hysteresis loop and giant magnetoresistance (GMR) curve traces are used to evaluate the interface properties and find that the value of interface exchange coupling coefficient J_{int} is approximately $0.32\,\text{pJ/m}$. Using this experimentally extracted J_{int}, we further simulate the dynamics of BFO/CoFe heterojunction and prove that the driving force of the magnetization switching of CoFe ($\mathbf{M}_{\text{FM}}$) is determined by the rotation of the Néel vector $\mathbf{N}$ rather than the rotation of the weak magnetization of BFO ($\mathbf{M}_c$). We also analyze the sensitivity of the switching success rate of the BFO/CoFe heterojunction with varying polarization switching times. The minimum polarization switching time ($t_{\text{FE,min}}$) of a successful switching depends on the aspect ratio of the device and the thickness of the CoFe layer. It is found that a smaller $t_{\text{FE,min}}$ can be obtained by a thinner CoFe thin film. Our simulation results in this work provide the critical metrics and guidelines for understanding and designing magnetoelectric devices. In collaboration with *Intel Corporation*, this work was published in *Nano Letters* [58].

To further leverage the simulation results and physical implications of these works, the rest of this chapter provides technical guidelines and prospective ideas for future research efforts in this field.

6.2 Future Works

6.2.1 Charge trapping and threshold voltage shift in HfO_2-based FeFETs

As mentioned in Chapter 1, ferroelectric field effect transistors (FeFETs) are considered a potential candidate for future nonvolatile memory applications based on the FE properties: (i) the electric polarization can be reversed by an externally applied voltage and (ii) the remanent polarization remains nonvolatile under zero bias. However, the use of conventional perovskite FE materials in emerging nonvolatile memory applications is limited by the material scalability and the lack of CMOS process compatibility. Recently, the discovery of the ferroelectricity in doped HfO_2 thin films reignited the research interest in FeFETs as such materials may overcome the major limitations of the perovskite FEs. In addition, HfO_2 films doped with silicon (Si:HfO_2) were shown to exhibit ferroelectric properties in a wide temperature range between -100°C and 200°C [201]. A potential of 10-year data retention at 150°C was also demonstrated for the Si:HfO_2-based ferroelectric transistors [202]. In addition, endurance capability of 10^5 program/erase cycles was achieved with a delay of $100\,\mathrm{ms}$ [49]. Therefore, FE nonvolatile memories based on doped HfO_2 have been under intensive research investigation.

In theory, when the gate voltage $V_\mathrm{G} > 0$, the FE polarization will point downwards, and minority carriers (electrons) are induced near the semiconductor surface, driving the FeFET into the low threshold voltage state [49]. On the other hand, when the gate voltage $V_\mathrm{G} < 0$, the FE polarization will point upwards, and majority carriers (holes) are induced near the semiconductor surface, driving the FeFET into the high threshold voltage state [49]. Because of the nonvolatility of the FE polarization, the two different threshold voltage states and the memory window (MW) still remain under zero gate bias until the polarization state is reversed again by a write gate voltage. Such threshold voltage shift mechanisms due to the FE polarization are illustrated in Figs. 6.2(a) and (b).

However, for the possible realization of FeFETs, there are still various reliability

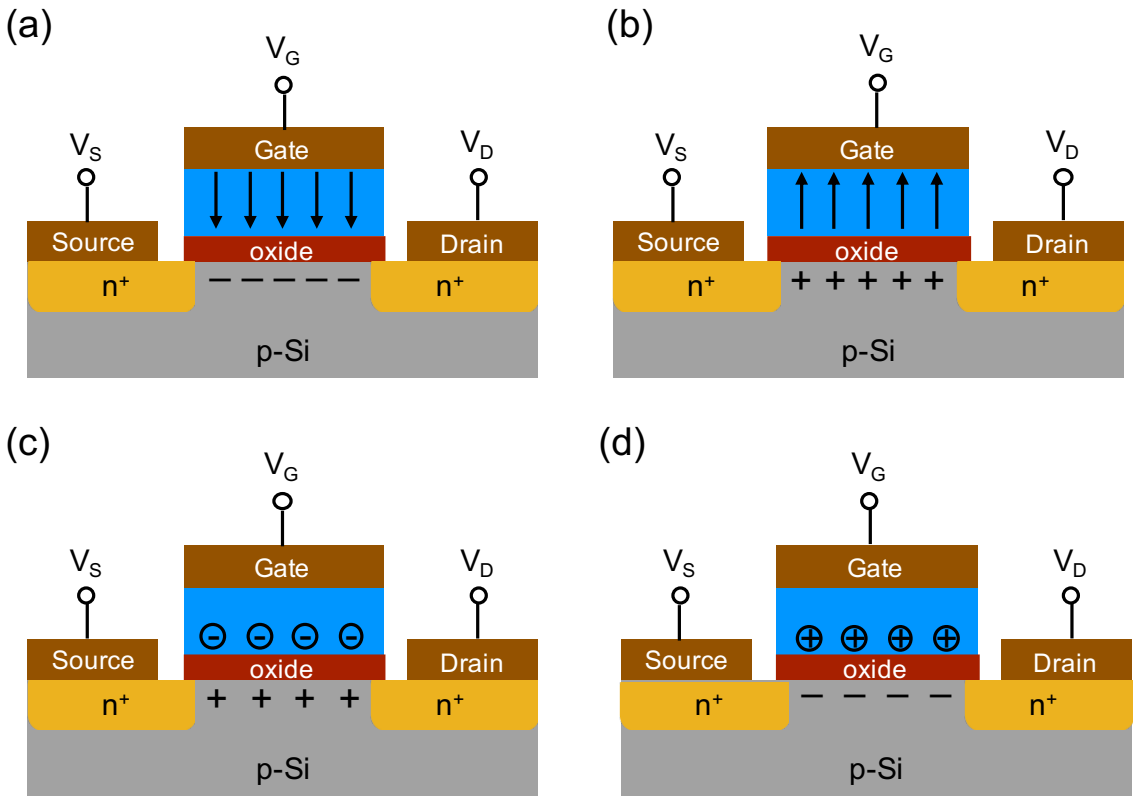

Figure 6.2: (a) Low V_{th} state of an FeFET at $V_G > 0$. (b) High V_{th} state of an FeFET at $V_G < 0$. (c) At $V_G > 0$, electrons trapped in the FE layer induce more holes in the channel, which shifts V_{th} toward the right. (d) At $V_G > 0$, holes trapped in the FE layer induce more electrons in the channel, which shifts V_{th} toward the left.

concerns. In particular, the mobility degradation, threshold voltage (V_{th}) instability and other reliability issues such as negative and positive bias temperature instability and enhanced stress-induced leakage current are attributed to the high density of intrinsic HfO_2 defects (as large as $10^{12} \sim 10^{14}$ cm^{-2}). The main origin of traps in HfO_2 dielectrics are believed to be oxygen vacancies and oxygen interstitial atoms. These intrinsic defects can serve as electron and/or hole traps, and thus have a strong impact on the behavior of the high-κ CMOS logic transistors.

In the literature, the impact of charge trapping on the performance of HfO_2-based FeFETs have been experimentally demonstrated to induce a V_{th} shift in the opposite direction to that caused by the ferroelectric switching for the same polarity of the gate voltage [49]. For example, the positive (downward) FE polarization induced by a positive

gate voltage leads to a negative I_D-V_G shift. On the other hand, electrons trapped within the gate oxides at positive gate voltage result in a positive shift of the drain current-gate voltage (I_D-V_G) characteristic. Such threshold voltage shift mechanisms due to the trap charges are illustrated in Figs. 6.2(c) and (d). Therefore, a superposition of the mechanisms from the FE polarization and trapped charges in the FE layer will result in the undesirable reduction of the memory window for FeFET devices. In addition, parasitic charge trapping effects were also believed to cause the endurance and retention degradation of HfO_2-based FeFETs [173, 203, 204]. As a result, the trapping dynamics and its interplay with the ferroelectric switching has to be studied both experimentally and theoretically for the purpose of nonvolatile FeFET realization.

Aiming to provide physical insights into the V_{th} shift of FeFETs during the voltage stress and relaxation, this work includes two parts as follows. First, we establish the trapped charge dynamics based on the Shockley-Read-Hall recombination theory and the multi-phonon trap-assisted tunneling. The model will be verified with experimental measurements of the V_{th} shift in HfO_2/SiO_x high-κ gate stacks when under voltage stress and relaxation. Second, the trapped charge dynamics will be applied to further study the V_{th} shift in MFIS capacitors and FeFETs. The goal of this work is to better understand the interplay between the FE polarization switching and the charged defect trapping, which plays an important role in the performance degradation of FeFETs as a potential emerging nonvolatile memory device.

Physics-based Simulations

Before we dive into the study of the impact of trap charge dynamics on FeFET performance, we would like to establish and validate a physics-based model based on the previous experiments on charge trapping in high-κ gate stacks [205]. The high-κ gate stack considered is composed of metal-HfO_2-SiO_x-(p-Si), as shown in Fig. 6.3, where V_G is the applied gate voltage, ψ is the semiconductor surface potential, V_{FB} is the flat band

voltage, and V_{M}, V_{DE} and V_{ox} denote the voltage across the metal contact, HfO_2 and SiO_x, respectively. The voltages across each layer can be obtained using the screening charge density σ in the stack, as listed below.

$$\begin{cases} \sigma = -Q_{\mathrm{net}}\,[\mathrm{C/cm^2}] = -q\int_0^{\infty}\left(-N_a^- - n(x) + p(x)\right)\mathrm{d}x \\ V_{\mathrm{M}} = \sigma\lambda/(\epsilon_0\epsilon_{\mathrm{M}}) \\ V_{\mathrm{DE}} = \sigma t_{\mathrm{HfO2}}/(\epsilon_0\epsilon_{\mathrm{HfO2}}) \\ V_{\mathrm{ox}} = \sigma t_{\mathrm{SiOx}}/(\epsilon_0\epsilon_{\mathrm{SiOx}}) \\ V_{\mathrm{G}} = V_{\mathrm{M}} + V_{\mathrm{DE}} + V_{\mathrm{ox}} + (\psi + V_{\mathrm{FB}}), \end{cases} \tag{6.1}$$

where λ is the screening length of the metal contact, ϵ_{M} is the dielectric constant of the metal contact, t_{HfO2} is the HfO_2 thickness, ϵ_{HfO2} is the dielectric constant of HfO_2, t_{SiOx} is the SiO_x thickness, and ϵ_{SiOx} is the dielectric constant of SiO_x. Note that the initial V_{FB} without the trap charge contribution is given as

$$V_{\mathrm{FB}}(t=0) = \phi_1 - \phi_2 - \mu_{\mathrm{M}} - \delta, \tag{6.2}$$

where ϕ_1 and ϕ_2 are the conduction band discontinuities at the metal-HfO_2 and SiO_x-semiconductor interfaces, respectively, μ_{M} is the Fermi level in the metal, and $\delta = E_c - \mu_{\mathrm{Si}}$ is the energy difference between the conduction band (E_c) and the Fermi level in the semiconductor (μ_{Si}). Note that δ is obtained by using the Joyce-Dixon approximation given as

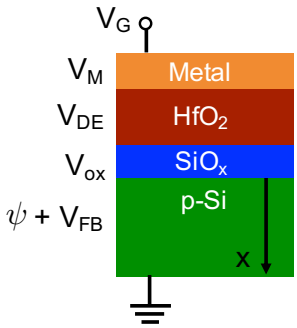

Figure 6.3: Metal-dielectric-insulator-semiconductor gate stack considered in this work.

$$\delta = k_{\mathrm{B}}T\left[\ln\left(\frac{N_c}{n}\right) - \frac{n}{\sqrt{8}N_c} + \left(\frac{3}{16} - \frac{\sqrt{3}}{9}\right)\left(\frac{n}{N_c}\right)^2\right], \tag{6.3}$$

where N_c is the effective density of states (DOS) in the semiconductor conduction band [139]. Due to the trap charge contribution, the V_{FB} shift over time can be calculated

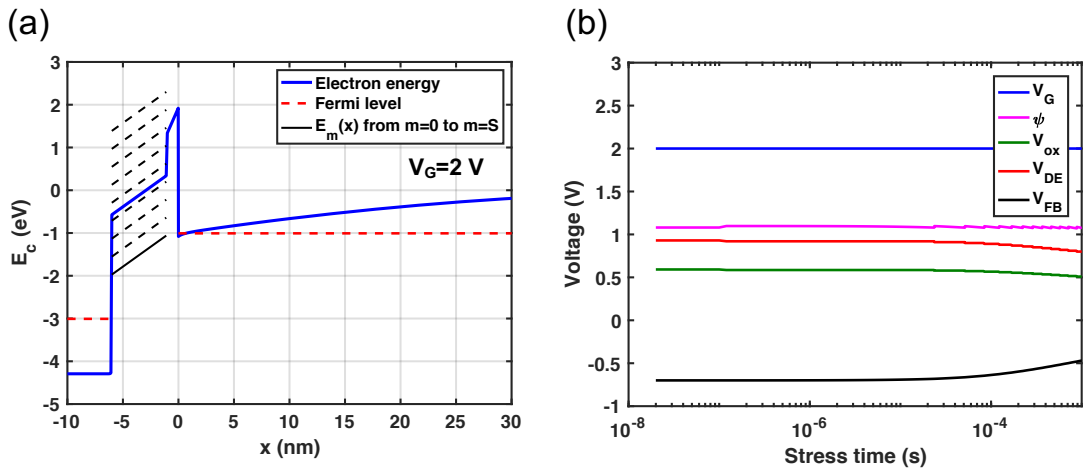

Figure 6.4: (a) Energy band diagram of a metal-dielectric-insulator-semiconductor gate stack with the device width $W = 100\,\mathrm{nm}$ at an applied gate voltage $V_\mathrm{G} = 2\,\mathrm{V}$. (b) The corresponding shifts of the surface potential ψ, HfO_2 voltage V_DE and SiO_x voltage V_ox due to the flat-band voltage V_FB shift caused by the electrons trapped in HfO_2 at an applied gate voltage V_G.

as

$$\Delta V_\mathrm{FB}(t) = -\frac{q}{C_\mathrm{HfO2} t_\mathrm{HfO2}} \int_0^{t_\mathrm{HfO2}} x' n_t(t)\,\mathrm{d}x' \,, \tag{6.4}$$

if only the defects in HfO_2 are considered for simplicity.

Figure 6.4(a) shows the energy band diagram of the high-κ gate stack based on the detailed formalism in Appendix B, and the voltage shifts in each layer due to the trapped electrons in HfO_2 under a voltage stress are shown in Fig. 6.4(b). The number of defects in dielectrics is expected to be high due to the devices with large lateral dimensions in experiments. Because of the computation limitation, one may first study the effect of the device size on the threshold voltage shift for the simulations with a scaled device size. By simulating the V_th shift up to $1\,\mathrm{ms}$, we find that the device width (and thus the number of traps) only affects the slope in the threshold voltage shift dynamics, as shown in Fig. 6.5. Other parameters used in the simulations are listed in Table B.1. So far, with the model limited by the computational efficiency, the simulations results do not match the experimental measurements well possibly because the defects in SiO_x and the transition rates between the HfO_2 and SiO_x layers are not considered as in [205]. It

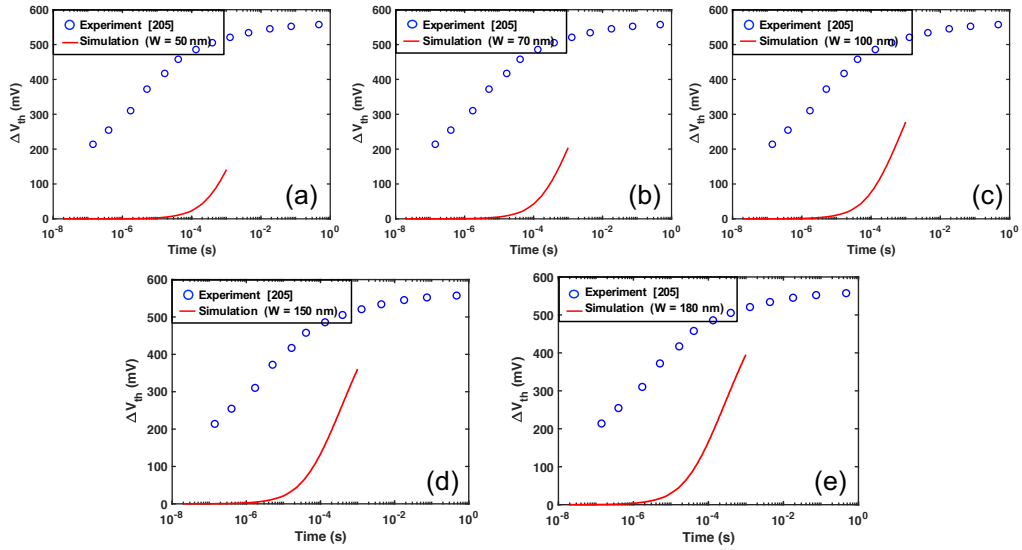

Figure 6.5: The effect of the device width W on the threshold voltage shift dynamics with $\rho_{\mathrm{HfO2}} = 1 \times 10^{20}\,\mathrm{cm}^{-3}$ compared to the experimental measurement at $V_{\mathrm{G}} = 2\,\mathrm{V}$ from [205]. The corresponding numbers of HfO_2 traps ($N_{\mathrm{t,HfO2}}$) are 1250, 2450, 5000, 11250 and 16200 for (a), (b), (c), (d) and (e), respectively.

may require an optimized non-linear ordinary differential equation solver to improve the model convergence and computation time. It is also noteworthy that a circuit-compatible FeFET model that incorporates the trap charge dynamics is needed for further performance analyses at the circuit and array levels.

6.2.2 Ultra-low power magnetoelectric random-access memory with an antiferromagnet/ferromagnet bilayer

Spintronic devices that have characteristics of non-volatility, scalability, and fast switching speed are promising for the embedded memory application [206]. Among them, voltage-controlled spintronic devices are especially attractive for low-power applications due to the elimination of the Joule heating energy [207]. Recently, experiments [57, 124, 208] have demonstrated the voltage-controlled magnetization switching in the BFO/CoFe heterojunction. In contrast to other voltage-controlled devices, deterministic $180°$ magnetization switching at room temperature in BFO/CoFe heterojunction is possible. Furthermore, recent experiments [209] have demonstrated that the coercive voltage of

the La-doped BFO layers can be as low as $0.1\,\mathrm{V}$ by tuning the doping concentration of La and reducing the thickness of the BFO layer. Besides, a previous study also shows that the switching speed of the polarization can be as fast as $100\,\mathrm{ps}$ [198]. Therefore, the magnetoelectric magnetic random-access memory (ME-MRAM) may potentially show ultra-low write energy and fast write speed compared to other spintronic memory devices [210]. However, modeling, design, and benchmarking for ME-MRAM is lacking. To conduct rigorous array level modeling, a fast and accurate compact model for BFO/CoFe heterojunction dynamics is needed.

To further evaluate the potential of the BFO/CoFe device in the application of ME-MRAM, we first build a compact model of the BFO/CoFe heterojunction based on an experimentally calibrated physical model we have developed recently [58]. To the best of our knowledge, this is the first compact model developed for an antiferromagnet/ferromagnet heterojunction. In addition, our compact model incorporates the magnetoelectric effect by combining the ferroelectric and the magnetic models for the BFO and CoFe layers. Compared to the previous studies which utilize the single-domain or macro-spin approximation for the free layer magnet of the magnetic tunnel junction, our compact model features two sublattices for both the antiferromagnetic and ferromagnetic layers. Therefore, our compact model can capture the exchange coupling field within the antiferromagnetic or ferromagnetic layers, and the interface exchange coupling field between these two layers. More importantly, using the BFO compact model developed in Chapter 5, the circuit level simulation and benchmarking of the magnetoelectric magnetic random-access memory (ME-MRAM) performances can be conducted. Based on our recent work [211], while ME-MRAM seems promising compared to other spintronic device candidates, the current challenges of ME-MRAM include the incompatibility to the fabrication process and the reliability issues. In addition, it was also shown that if the leakage current through the ferroelectric layer (BFO) is high, the voltage drop across the BFO will be degraded, and thus a larger write voltage is needed, which will increase the

write energy. Therefore, the circuit-compatible model with material parameters that can be calibrated enables further studies to provide technical guidelines for the application of such a low-power device in advanced memory arrays.

6.2.3 Domain partial switching and minor loops in ferroelectrics

As only part of the applied gate voltage is across the ferroelectric oxide in FET devices, it is likely that the ferroelectric layer undergoes partial domain switching during the operations. Such partial domain switching is manifested as history-dependent minor loops shown in electrical characterization of a ferroelectric capacitor [73]. So far, the Preisach hysteresis model implemented in a circuit-compatible manner has successfully captured partial switching of ferroelectric domains and the corresponding minor loops [73]. However, more experimental and theoretical efforts are still required to further investigate how ferroelectric domain switching is controlled by the applied voltage and what the hysteresis trajectories look like in actual ferroelectric-gated FETs.

6.2.4 Ferroelectric fatigue and trapped charges

Despite the promising properties of process compatibility and scalability, ferroelectric FETs based on $Hf_{1-x}Zr_xO_2$ suffer the reliability issues such as low endurance (ferroelectric fatigue) and threshold voltage shifts according to the recent experimental characterization [119, 163, 173]. Such reliability issues may be attributed to the charged defects and the associated trapping inside $Hf_{1-x}Zr_xO_2$ oxides. Therefore, it is critical to better understand the trapped charge dynamics during FET operations and possibly provide guidelines to alleviate charge trapping both experimentally and theoretically.

6.2.5 Anti-ferroelectricity

Besides ferroelectric properties, Zr-doped HfO_2 oxides also exhibit anti-ferroelectric characteristics, where double hysteresis loops are found near the two polarization states.

It was experimentally shown that the orthorhombic ferroelectric phase and tetragonal anti-ferroelectric phase of $Hf_{1-x}Zr_xO_2$ thin film can be controlled by the composition of $Hf_{1-x}Zr_xO_2$ (or Hf:Zr ratio) [84, 170].

As for the anti-ferroelectric properties of $Hf_{1-x}Zr_xO_2$, the dielectric constant was found to be further improved with optimal Zr doping concentration near the transition of the ferroelectric and anti-ferroelectric phases [84]. In addition, recent experimental characterization of $Hf_{1-x}Zr_xO_2$ capacitors for embedded dynamic random-access memory has demonstrated fast polarization switching for read/write operations, small operating voltage, long enough retention, and good endurance at elevated temperature [212]. For the theoretical study of fundamental material properties of the anti-ferroelectric phase, the simulations demonstrated that the anti-ferroelectric phase of perovskite $BaTiO_3$ may be described by the Landau phenomenological theory [79]. Moreover, first-principles calculations were applied to explain the phase transformations between the ferroelectric and anti-ferroelectric behaviors under strain in $Hf_{1-x}Zr_xO_2$ as well [213].

Appendices

APPENDIX A

THE FOURIER-SPECTRAL METHOD

A.1 MATLAB® Code of the Fourier-spectral Method

The source code for the functions of the 3D TDGL solver and 3D Poisson solver implemented in MATLAB® R2020a is listed below for reference. Note that the 2nd order semi-implicit scheme is used in the implementation [151].

Listing A.1: 3D TDGL solver using the Fourier-spectral method

```
function [Px,Py,Pz] = TDGL_fft_L(Px_hat,gx_hat,Py_hat,gy_hat,Pz_hat,gz_hat,...
                                 KX,KY,KZ,g11,g44,dt)
% Solve for time-dependent Ginzburg-Landau equation
% 2nd order semi-implcit Fourier spectral scheme
%   Notations:
%   P_0 = Pz(n-1); P_1 = Pz(n); P_2 = Pz(n+1);
%   P_hat_0 = P_hat_(n-1); P_hat_1 = P_hat_(n); P_hat_2 = P_hat_(n+1);

dtx = dt(1); dty = dt(2); dtz = dt(3);
% Extract parameters
Px_hat_1 = Px_hat.t1; Px_hat_0 = Px_hat.t0;
Py_hat_1 = Py_hat.t1; Py_hat_0 = Py_hat.t0;
Pz_hat_1 = Pz_hat.t1; Pz_hat_0 = Pz_hat.t0;

gx_hat_1 = gx_hat.t1; gx_hat_0 = gx_hat.t0;
gy_hat_1 = gy_hat.t1; gy_hat_0 = gy_hat.t0;
gz_hat_1 = gz_hat.t1; gz_hat_0 = gz_hat.t0;



    Px_hat_2 = ( 4*Px_hat_1 - Px_hat_0 + 2*dtx*(2*gx_hat_1 - gx_hat_0) )...
                ./( 3 + 2*dtx*(g11*KX.^2 + 2*g44*(KY.^2+KZ.^2)) );
    Px_hat_0 = Px_hat_1; Px_0 = real(ifftn(Px_hat_0));
    Px_hat_1 = Px_hat_2; Px_1 = real(ifftn(Px_hat_1));



    Py_hat_2 = ( 4*Py_hat_1 - Py_hat_0 + 2*dty*(2*gy_hat_1 - gy_hat_0) )...
```

```
                ./( 3 + 2*dty*(g11*KY.^2 + 2*g44*(KX.^2+KZ.^2)) );
    Py_hat_0 = Py_hat_1; Py_0 = real(ifftn(Py_hat_0));
    Py_hat_1 = Py_hat_2; Py_1 = real(ifftn(Py_hat_1));


    Pz_hat_2 = ( 4*Pz_hat_1 - Pz_hat_0 + 2*dtz*(2*gz_hat_1 - gz_hat_0) )...
                ./( 3 + 2*dtz*(2*g44*(KX.^2+KY.^2) + g11*KZ.^2) );
    Pz_hat_0 = Pz_hat_1; Pz_0 = real(ifftn(Pz_hat_0));
    Pz_hat_1 = Pz_hat_2; Pz_1 = real(ifftn(Pz_hat_1));



Px.t0 = Px_0; Px.t1 = Px_1;
Py.t0 = Py_0; Py.t1 = Py_1;
Pz.t0 = Pz_0; Pz.t1 = Pz_1;

end
```

Listing A.2: 3D Poisson solver using the Fourier-spectral method

```
function [ phi, E ]  = poisson3_fft_pbc( P, kappa, BC, N, h)
%%%%%%%%%%%%%%%%%%%%%%%%%%%%%%%%%%%%%%%%%%%%%%%%%%%%%%%%%%%%%%%%%%%%%%%%%%%%%%%
%
% A matlab function to solve 3D Poisson's equation for electrical potential
% profile inside FE films using spectral iterative perturbation method
%
% System: FE sandwiched between two electrodes
% P = [Px(x,y,z), Py(x,y,z), Pz(x,y,z)]
% 3D Poisson's equation inside the FE film:
% kappa*(phi,11 + phi,22 + phi,33) = -rho_b/ep0 = (P_1,1+P_2,2+P_3,3)/ep0
% E = -grad(phi)
%
% Boundary conditions:
% x,y: periodic BC; z: Dirichlet BC
%
% Inputs:
% P = P(x,y,z): 3D polarization distribution structure {P.x,.P.y,P.z}
% kappa = constant: relative dielectric constant of the material (assuming uniform)
% potential boundary conditions at the FE film interfaces
% BC = [phi_1, phi_2]: Potential boundary conditions in z direction
% N = [ny,nx,nz]:
```

```
%   nz: the # of interior points in z direction
%   ny and nx: the # of points in the in-plane direction
%
%   ***IMPORTANT: for fft efficiency***
%   nx = ny = 2^m;
%   nz = Nz/2-1 for including Dirichlet BCs of phi, where Nz = 2^n
% h: grid spacing in real space, where dz = 2*(domain size)/Nz
%
% Outputs:
% phi(x,y,z): potential distribution, size = (ny) x (nx) x (nz+2)
% E: electric field, cell structure {x,y,z}, size = (ny) x (nx) x (nz+2)
%
% author: Chia-Sheng Hsu
% Last modified: 2018.08.24
%%%%%%%%%%%%%%%%%%%%%%%%%%%%%%%%%%%%%%%%%%%%%%%%%%%%%%%%%%%%%%%%%%%%%%%%%%%%%%%%


%%% Universal constants
global ep0

% # of grid points
ny = N(1); nx = N(2); nz = N(3);
% # of grid points in the extended domain
Ny = ny; Nx = nx; Nz = 2*(nz+1);
% grid spacing
dy = h(1); dx = h(2); dz = h(3);

Px = P.x; Py = P.y; Pz = P.z;
% % RHS of Poisson's equation
phi_1 = BC(:,:,1); phi_2 = BC(:,:,2); % Dirichlet potential BCs in z direction

% RHS of the equation: f = force terms
[fx,~,~] = gradient(Px,dx); % Px,x
[~,fy,~] = gradient(Py,dy); % Py,y
[~,~,fz] = gradient(Pz,dz);  % Pz,z
f = (fx + fy + fz)/ep0/kappa; % (Px,x + Py,y + Pz,z)/epsilon

% correction of RHS for Dirichlet BCs in z
f(:,:,1) = f(:,:,1) - phi_1/dz^2; f(:,:,end) = f(:,:,end) - phi_2/dz^2;

% odd extension in z direction due to Dirichlet BCs
```

```
63 f = cat(3, zeros(ny,nx,1), f, zeros(ny,nx,1), -f(:,:,end:-1:1));
64
65 % wave vectors in (extended) Fourier space
66 kx = 2/dx*sin((0:Nx-1)*pi/Nx); ky = 2/dy*sin((0:Ny-1)*pi/Ny);
67 kz = 2/dz*sin((0:Nz-1)*pi/Nz);
68 [KX,KY,KZ] = meshgrid(kx,ky,kz);
69 delta = zeros(size(KX)); delta(1) = 1; % avoid zero division
70
71 %keyboard
72 f_hat = fftn(f);
73 % F{phi}
74 phi_hat = -(f_hat)./(KX.^2 + KY.^2 + KZ.^2 + delta);
75
76 % electric potential profile
77 phi = real(ifftn(phi_hat));
78
79 % extaction of real phi
80 phi = phi(1:ny,1:nx,1:nz+2);
81
82 % includes BCs
83 phi(:,:,1) = phi_1;
84 phi(:,:,end) = phi_2;
85
86 % electric field structure
87 [Ex,Ey,Ez] = gradient(phi,dx,dy,dz);
88 E.x = -Ex(:,:,2:end-1); E.y = -Ey(:,:,2:end-1); E.z = -Ez(:,:,2:end-1);
89
90 phi = phi(:,:,2:end-1);
```

APPENDIX B

THEORETICAL FORMALISM FOR TRAP CHARGE DYNAMICS IN HIGH-κ GATE STACKS AND FeFETS

It is well known that in semiconductor, $n_0 p_0 = n_i^2$ at thermal equilibrium, where n_0 is the electron concentration, p_0 is the hole concentration, and n_i is the intrinsic carrier concentration. In the doped Si substrate with an acceptor concentration N_{a} and a donor concentration N_{d}, general charge neutrality condition at thermal equilibrium implies

$$\begin{aligned} & n_0 + N_{\text{a}}^- = p_0 + N_{\text{d}}^+ \\ & \Rightarrow n_0 + (N_{\text{a}} - p_{\text{a}}) = p_0 + (N_{\text{d}} - n_{\text{d}}), \end{aligned} \tag{B.1}$$

where N_{a}^- is the concentration of ionized acceptors and N_{d}^+ is the concentration of ionized donors. With $n_0 p_0 = n_i^2$ and the assumption of complete ionization, i.e., the concentrations of hole ions p_{a} and electron ions n_{d} are equal to zero, one can obtain the hole concentration in doped Si as

$$p_0 = \frac{1}{2}\left[(N_{\text{a}} - N_{\text{d}}) + \sqrt{(N_{\text{a}} - N_{\text{d}})^2 + 4n_i^2}\right]. \tag{B.2}$$

For p-type Si, $N_{\text{a}} - N_{\text{d}} \gg n_i$ and therefore from Eq. (B.2), $p_0 \approx N_{\text{a}} - N_{\text{d}}$ and $n_0 \approx n_i^2/(N_{\text{a}} - N_{\text{d}})$.

Without the donor N_{d}, the 1D Poisson's equation along the gate direction (x) can be

derived as

$$\begin{aligned}\frac{\mathrm{d}^2\psi}{\mathrm{d}x^2} &= \frac{-q}{\epsilon_0\epsilon_{\mathrm{Si}}}\left[\left(p(x)+N_{\mathrm{d}}^{+}\right)-\left(n(x)+N_{\mathrm{a}}^{-}\right)\right] \\ &= \frac{-q}{\epsilon_0\epsilon_{\mathrm{Si}}}\left[p(x)-n(x)+\left(N_{\mathrm{d}}^{+}-N_{\mathrm{a}}^{-}\right)\right] \\ &= \frac{-q}{\epsilon_0\epsilon_{\mathrm{Si}}}\left[p(x)-n(x)+n_0-p_0\right] \\ &= \frac{-q}{\epsilon_0\epsilon_{\mathrm{Si}}}\left[p(x)-n(x)+n_i^2/N_{\mathrm{a}}-N_{\mathrm{a}}\right],\end{aligned} \tag{B.3}$$

where q is the elementary charge, ϵ_0 is the vacuum dielectric constant, ϵ_{Si} is the Si dielectric constant, and ψ is the potential as a function of x in the p-Si substrate. Based on the Boltzmann distribution, the carrier concentrations along x can be written as

$$\begin{cases} p(x) = n_i \exp\left[\frac{E_{ib}-E_F}{k_{\mathrm{B}}T}\right]\exp\left[\frac{-q\psi(x)}{k_{\mathrm{B}}T}\right] = n_i \exp\left(\frac{q\phi_{\mathrm{B}}}{k_{\mathrm{B}}T}\right)\exp\left[\frac{-q\psi(x)}{k_{\mathrm{B}}T}\right] = N_{\mathrm{a}}\exp\left[\frac{-q\psi(x)}{k_{\mathrm{B}}T}\right] \\ n(x) = n_i^2/p(x) = \frac{n_i^2}{N_{\mathrm{a}}}\exp\left[\frac{+q\psi(x)}{k_{\mathrm{B}}T}\right], \end{cases} \tag{B.4}$$

where E_{ib} is the intrinsic Fermi level in the bulk region of Si, E_F is the Fermi level, and k_{B} and T are the Boltzmann constant and temperature, respectively. By plugging the above expressions into Eq. (B.3), one arrives at the Poisson-Boltzmann equation [214]:

$$\frac{\mathrm{d}^2\psi}{\mathrm{d}x^2} = \frac{-q}{\epsilon_0\epsilon_{\mathrm{Si}}}\left[N_{\mathrm{a}}\left(e^{\frac{-q\psi}{k_{\mathrm{B}}T}}-1\right)-\frac{n_i^2}{N_{\mathrm{a}}}\left(e^{\frac{q\psi}{k_{\mathrm{B}}T}}-1\right)\right]. \tag{B.5}$$

To numerically solve 1D Poisson's equation, we adopt the Newton-Raphson iteration method, which is a numerical way to find solutions x to $f(x)=0$. The recurrence relation

can be derived as follows:

$$
\begin{aligned}
0 = f(x) = f(x_0 + h) &= f(x_0) + hf'(x_0) + O(h^2) \\
\Rightarrow x - x_0 = h &\approx -\frac{f(x_0)}{f'(x_0)} \\
\Rightarrow x &= x_0 - \frac{f(x_0)}{f'(x_0)} \\
\Rightarrow \boxed{x_{n+1} &= x_n - \frac{f(x_n)}{f'(x_n)}},
\end{aligned}
\tag{B.6}
$$

where the solutions are obtained when $x_{n+1} \approx x_n$ if convergent. Fig. B.1 shows the geometrical interpretation of this numerical method, where x_{n+1} is closer to the root solution r after each iteration.

Recall the governing Poisson's equation (Eq. (B.3)) is an equation set with the from of $\mathbf{A}\phi = b(\phi)$, where the operator $\mathbf{A} = \frac{\mathrm{d}^2}{\mathrm{d}x^2}$ and $b(\phi) =$ RHS. Let $F(\phi) = \mathbf{A}\phi - b(\phi)$ be the target function and the Jacobian $\mathbf{J} = \frac{\mathrm{d}F}{\mathrm{d}\phi} = \mathbf{A} - \frac{\mathrm{d}b(\phi)}{\mathrm{d}\phi}$. The ratio of the target function and its derivative ($\Delta\phi$) is then the solution to $\mathbf{J}\Delta\phi = F(\phi)$, from which one can obtain the solution in the iteration from the recurrence relation $\phi_{n+1} = \phi_n - \Delta\phi$.

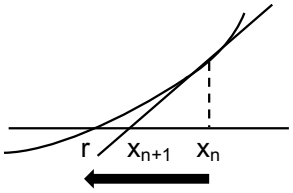

Figure B.1: Newton-Raphson iteration method

To describe the trap charge dynamics in FeFETs, we adopt the Shockley-Read-Hall recombination theory and the multi-phonon trap-assisted tunneling [205, 215, 216]. For the electron capture process, the rate of electron capture can be expressed as $f_{pt}N_t c_n(E)f(E)N(E)\,\mathrm{d}E$, where N_t is the number of trapping centers per unit volume, $c_n(E)$ is the average probability per unit time that an electron in the range dE is captured by an empty trap, $N(E)\,\mathrm{d}E$ is the total number of quantum states in the energy range $\mathrm{d}E$, and $f(E) = 1/[1 + \exp\{(E - \mu)\beta\}]$ is the Fermi-Dirac distribution function with μ being the Fermi level and $\beta = 1/(k_{\mathrm{B}}T)$. The probability that a trap is empty f_{pt} (and thus capable of capturing an electron) follows Fermi-Dirac statistics, i.e., $f_{pt}(E_t) = 1 - f_t(E_t)$, and the

probability that a trap is occupied $f_t(E_t) = 1/[1 + \exp\{(E_t - \mu)\beta\}]$, where E_t is the trap energy level. Similarly, for the electron emission process, the rate of electron emission can be expressed as $f_t N_t e_n(E) f_p(E) N(E)\,\mathrm{d}E$, where $e_n(E)$ is the average probability per unit time that an electron in the range $\mathrm{d}E$ is emitted from a filled trap, and $f_p(E) = 1 - f(E)$.

With the above expressions, the net rate of electron capture in $\mathrm{d}E$ is then

$$\mathrm{d}R_{cn} = [f_{pt} f(E) - (e_n/c_n) f_t f_p(E)] N_t c_n(E) N(E)\,\mathrm{d}E\,. \tag{B.7}$$

At thermal equilibrium, the rate of capture and the rate of emission of electrons must be equal and one obtains the relation between e_n and c_n:

$$\frac{e_n}{c_n} = \frac{f_{pt} f}{f_t f_p} = \frac{(1 - f_t) f}{f_t (1 - f)} = \exp\left[(E_t - E)\beta\right]. \tag{B.8}$$

Before reaching the steady state, the rate equation for electron capture and emission out of equilibrium can be derived as

$$\begin{aligned}
\frac{\mathrm{d}n_t}{\mathrm{d}t} = N_t \frac{\mathrm{d}f_t}{\mathrm{d}t} &= \int \mathrm{d}R_{cn} = \int_{E_c}^{\infty} [c_n(E)(1 - f_t) f(E) - e_n(E) f_t (1 - f(E))] N_t g_c(E)\,\mathrm{d}E \\
&= \int_{E_c}^{\infty} \left[(1 - f_t) f(E) - \frac{e_n(E)}{c_n(E)} f_t (1 - f(E))\right] N_t c_n(E) g_c(E)\,\mathrm{d}E \\
&= N_t \int_{E_c}^{\infty} [(1 - f_t) - \exp\{(E_t - \mu_n)\beta\} f_t] f(E) c_n(E) g_c(E)\,\mathrm{d}E \\
&= N_t \big[(1 - f_t) - e^{(E_t - \mu_n)\beta} f_t\big] \int_{E_c}^{\infty} f(E) c_n(E) g_c(E)\,\mathrm{d}E \\
&= N_t \big[(1 - f_t) - e^{(E_t - \mu_n)\beta} f_t\big] \sigma_n v_n^{th} n \\
&= N_t \left[\frac{(1 - f_t)}{\tau_{cn}} - \frac{f_t}{\tau_{en}}\right] = \frac{N_t - n_t}{\tau_{cn}} - \frac{n_t}{\tau_{en}},
\end{aligned} \tag{B.9}$$

where $n_t = N_t f_t$ is the trapped electron density, σ is the tunneling cross section, v_n^{th} is the thermal velocity of trapped electrons, n is the electron density in the substrate, $g_c(E)$ is the 3D density of state, τ_{cn} is the electron capture time constant, and τ_{en} is the electron

emission time constant that follows Eq. (B.8), i.e., $\tau_{en} = \tau_{cn} \exp\{(\mu_n - E_t)\beta\}$. Note that the derived trap rate equation is consistent with the one used in [119].

Next, we adopt the multi-phonon trap-assisted tunneling mechanism to determine the capture and emission time constants in Eq. (B.9). The capture and emission rates can be expressed as

$$\begin{cases} c_n(E,x) = c_0 \sum_{m=0}^{\infty} L_m(z)\delta[E - E_m(x)], \\ e_n(E,x) = c_0 \exp\left(-\frac{E-E_t(x)}{kT}\right) \sum_{m=0}^{\infty} L_m(z)\delta[E - E_m(x)], \end{cases} \tag{B.10}$$

where c_0 is a constant, the trap energy levels E_t are broadened with discrete phonon coupling m with frequency ω_0, i.e., $E_m(x) = E_t(x) + m\hbar\omega_0$ and $E_t(x) = E_c(x) - \Phi_t(x)$ with thermal binding energy $\Phi_t(x)$ [217, 218]. Multi-phonon transition probability is given by

$$L_m(z) = \left(\frac{f_B + 1}{f_B}\right)^{m/2} \exp\left[-S(2f_B + 1)\right] I_m(z), \tag{B.11}$$

where $f_B = \frac{1}{\exp(\hbar\omega_0/k_{\mathrm{B}}T)-1}$ is the Bose-Einstein function, $S = \frac{E_{\mathrm{rel}}}{\hbar\omega_0}$ is the Huang-Rhys factor with E_{rel} being the trap relaxation energy, I_m is the modified Bessel function of first kind with order m, and the variable z is defined as $z = 2S\sqrt{f_B(f_B + 1)}$.

With the summation over all the discrete energy levels $E_m(x)$, the capture and emission trapping time constants can be written as

$$\begin{cases} \tau_c^{-1}(x) = \sum_{m=0}^{\infty} g_c(E_m) f_c(E_m) T_c(E_m, x) c_0 L_m(z) \\ \tau_e^{-1}(x) = \sum_{m=0}^{\infty} g_e(E_m)[1 - f_e(E_m)] T_e(E_m, x) c_0 L_m(z) \exp\left(-\frac{m\hbar\omega_0}{kT}\right), \end{cases} \tag{B.12}$$

where $T(E_m, x)$ is the tunneling probability, and the subscripts c and e denote capture and emission events, respectively. The 3D density of state is given by

$$g(E) = \frac{\sqrt{k_{\mathrm{B}}T}}{2\pi^2} \left(\frac{2m_0}{\hbar^2}\right)^{3/2} \left(\frac{m^*}{m_0}\right)^{3/2} \left(\frac{E - E_c}{k_{\mathrm{B}}T}\right)^{1/2} H(E - E_c), \tag{B.13}$$

where m^* is the effective electron mass, m_0 is the electron rest mass and H is the Heaviside step function.

One possible way to calculate the tunneling probability is using the WKB approximation, where analytical expressions are given by [217]

$$\begin{cases} T(E,x) = \exp\left[-\frac{4}{3}\left(\frac{E_c(0)-E}{\hbar\theta_0}\right)^{3/2} + \frac{4}{3}\left(\frac{E_c(x)-E}{\hbar\theta_0}\right)^{3/2}\right], \text{ for trapezoidal barriers,} \\ T(E,x) = \exp\left[-\frac{4}{3}\left(\frac{E_c(x)-E}{\hbar\theta_0}\right)^{3/2} + \frac{4}{3}\left(\frac{E_c(d)-E}{\hbar\theta_0}\right)^{3/2} H(E_c(d)-E)\right], \text{ for triangular barriers,} \end{cases} \tag{B.14}$$

where $\hbar\theta_0 = \left(\frac{q^2\hbar^2 E_{\text{ox}}^2}{2m^*}\right)^{1/3}$ denotes the electro-optical energy in the oxide under the field E_{ox}. A schematic diagram is shown in Fig. B.2 and the detailed derivation can be found in Appendix C. Note that here, the potential well $V(x)$ is induced by the point charged traps due to the coulomb potential of a point charge at a positive trap site, i.e., $V(x) = E_c(x) - V_0\delta(x - x_t)$, where $E_c(x)$ is the conduction band edge, x_t is the trap position and V_0 is a constant [217].

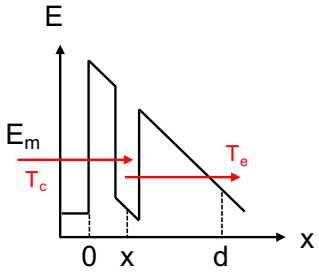

Figure B.2: Tunneling probability through energy barriers using WKB approximation. Adapted from [217]

Last, the threshold voltage V_{th} shift can be calculated with the trap density obtained from the rate equation (Eq. (B.9))

$$\Delta V_{\text{th}}(t) = \sum_{j=1}^{N_t} \Delta V_{\text{th}}^j \left(f_t^j(t) - f_t^j(0)\right), \tag{B.15}$$

where ΔV_{th}^j is the contribution from one trap charge j. With the trapped charges having larger contributions near the HfO_2/SiO_x interface, ΔV_{th}^j is expressed as

$$\begin{aligned} \Delta V_{\text{th}}^j(x) &= \frac{1}{C_{\text{DE}}}\left(\frac{1}{x}\int_0^x x'\rho(x')\,\mathrm{d}x'\right) \\ &= \frac{1}{C_{\text{HfO2}}}\left(\frac{1}{x}\int_0^x x'\rho_{\text{HfO2}}\,\mathrm{d}x'\right) = \frac{\rho_{\text{HfO2}}}{C_{\text{HfO2}}}\frac{x}{2}, \end{aligned} \tag{B.16}$$

Table B.1: Physical Parameters Used in This Preliminary Work

Parameter	Value
t_{HfO2} (nm)	5
t_{SiOx} (nm)	1
ϵ_{HfO2}	21
ϵ_{SiOx}	6.6
ϵ_{M}	2
ϵ_{Si}	11.7
λ (cm)	0.5×10^{-8}
E_{g} (eV)	1.12
N_{a} (cm^{-3})	5×10^{17}
N_{C} (cm^{-3})	2.82×10^{19}
N_{V} (cm^{-3})	1.83×10^{19}
ϕ_1 (eV)	3
ϕ_2 (eV)	2
ϕ_{FD}[1](eV)	1
μ_{M} (eV)	0.7
Φ_{t} (eV)	1.4
E_{rel} (eV)	1.19

[1] the conduction band discontinuity at the HfO_2 and SiO_x interface

where x is the distance from the metal/HfO_2 interface, ρ is the constant volume trap density in HfO_2 [205] and C_{HfO_2} is the capacitance density of HfO_2 per unit area. Table B.1 lists all the physical parameters used for the simulations in Sec. 6.2.1.

APPENDIX C

SOLVING QUANTUM TUNNELING COEFFICIENTS WITH WKB APPROXIMATION

C.1 Derivation of the Transmission Coefficient

In this note, we consider the following potential barrier with the width equal to $b - a$:

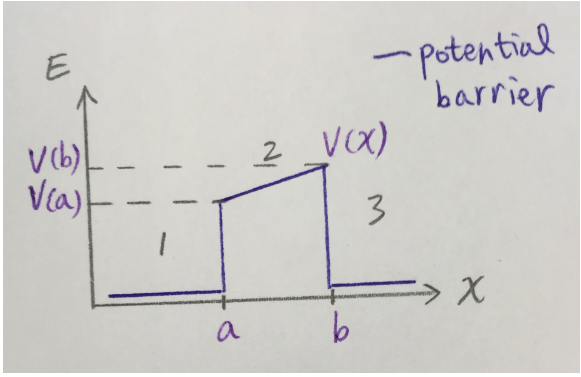

Figure C.1: potential energy barrier under consideration

In region 3, we can write down the WKB approximation solution to the one dimensional time-independent Schrödinger equation $-\frac{\hbar^2}{2m}\frac{d^2\psi}{dx^2} + V(x) = E\psi$ as (assuming the amplitude = 1)

$$\begin{aligned}\psi_3(x) &= \frac{1}{\sqrt{k}} e^{i\int_b^x k(x')dx'} \\ &= \frac{1}{\sqrt{k}} \cos\left(\int_b^x k(x')dx' - \frac{\pi}{4}\right) + i\frac{1}{\sqrt{k}} \sin\left(\int_b^x k(x')dx' - \frac{\pi}{4}\right).\end{aligned}$$

According to the connection formula, the wave function in region 2 is

$$\psi_2(x) = \frac{1}{2\sqrt{\kappa}} e^{-\int_x^b \kappa(x')dx'} - i\frac{1}{\sqrt{\kappa}} e^{\int_x^b \kappa(x')dx'}.$$

Note that

$$\begin{cases} k(x) = \dfrac{\sqrt{2m(E-V(x))}}{\hbar}, & \text{if } E > V(x) \\ \kappa(x) = \dfrac{\sqrt{2m(V(x)-E)}}{\hbar}, & \text{if } E < V(x) \end{cases}$$

Now we rewrite $\int_x^b \kappa(x')dx'$ as

$$-\int_a^x \kappa(x')dx' + \underbrace{\int_a^b \kappa(x')dx'}_{\alpha}$$

$$\Rightarrow \psi_2(x) = \frac{1}{2\sqrt{\kappa}} e^{-\alpha} e^{+\int_a^x \kappa dx'} - i\frac{1}{\sqrt{\kappa}} e^{\alpha} e^{-\int_a^x \kappa dx'}$$

The WKB connection formula can be used again to connect the region 2 and region 1 and let $\int_x^a k(x')dx' - \frac{\pi}{4} = u$:

$$\begin{aligned} \psi_1(x) &= \frac{1}{2\sqrt{k}} e^{-\alpha} \sin\left(\int_x^a k(x')dx' - \frac{\pi}{4}\right) - 2i\frac{1}{\sqrt{k}} e^{\alpha} \cos\left(\int_x^a k(x')dx' - \frac{\pi}{4}\right) \\ &= \frac{1}{2\sqrt{k}} e^{-\alpha} \sin u - i\frac{1}{\sqrt{k}} e^{\alpha} \cos u \\ &= \frac{1}{2\sqrt{k}} e^{-\alpha}(e^{iu} - e^{-iu}) \cdot \frac{1}{2i} - i\frac{1}{\sqrt{k}} e^{\alpha}(e^{iu} + e^{-iu}) \\ &= \frac{1}{\sqrt{k}}(-ie^{\alpha} - \frac{i}{4}e^{-\alpha})e^{iu} + \frac{1}{\sqrt{k}}(-ie^{\alpha} + \frac{i}{4}e^{-\alpha})e^{-iu} \end{aligned}$$

The e^{iu} term corresponds to the incident wave while the e^{-iu} corresponds to the reflected wave. Therefore, we arrive at the transmission coefficient

$$T \approx \frac{k}{k}\left|\frac{\psi_3(x)}{\psi_1^{inc}(x)}\right|^2 = \left|\frac{1}{e^{\alpha} + \frac{1}{4}e^{-\alpha}}\right|^2 \tag{C.1}$$

Recall that $\alpha = \int_a^b \kappa(x')dx'$. In our case, $V(x) = V(a) + s(x-a)$, where $s = \frac{V(b)-V(a)}{b-a}$, so

$$\alpha = \frac{\sqrt{2m}}{\hbar}\int_a^b dx\sqrt{V(a) + s(x-a) - E} \;\; = \frac{\sqrt{2m}}{\hbar}\frac{2}{3s}[(V(b)-E)^{\frac{3}{2}} - (V(a)-E)^{\frac{3}{2}}].$$

If the barrier is high and wide, then α would be large, which allows to further simplify the transmission coefficient:

$$T \approx \frac{1}{e^{2\alpha}} = \exp\left(-\frac{4\sqrt{2m}}{3s\hbar}\left[(V(b)-E)^{\frac{3}{2}} - (V(a)-E)^{\frac{3}{2}}\right]\right) \tag{C.2}$$

With the formula above, we can compute the transmission coefficient as a function of any energies smaller than the potential barrier. In order to construct $T(E)$, we still need to consider the case where the particle energy is larger than the the barrier. Assume

$$\begin{aligned}
\psi_1(x) &= \frac{A}{\sqrt{k}}e^{i\int_x^a k(x')dx'} + \frac{B}{\sqrt{k}}e^{-i\int_x^a k(x')dx'} \\
\psi_2(x) &= \frac{C}{\sqrt{l}}e^{i\int_a^x l(x')dx'} + \frac{D}{\sqrt{l}}e^{-i\int_a^x l(x')dx'} \\
\psi_3(x) &= \frac{F}{\sqrt{k}}e^{i\int_b^x k(x')dx'}
\end{aligned}$$

For convenience, we let $k(x) = \sqrt{E}$, $l(x) = \sqrt{E - V(x)}$, $\phi_a = l^2(a)$, $\phi_b = l^2(b)$, and other notations are the same as in the previous section. Since at the boundary, the wave function and its first derivative must be continuous, we have at $x = a$,

$$\frac{A}{\sqrt{k}} + \frac{B}{\sqrt{k}} = \frac{C}{\sqrt{l(a)}} + \frac{D}{\sqrt{l(a)}} \tag{C.3}$$

$$i\sqrt{k}A - i\sqrt{k}B = \left[i\sqrt{l(a)} - \frac{1}{2}(l(a))^{-3/2}\right]C + \left[-i\sqrt{l(a)} - \frac{1}{2}(l(a))^{-3/2}\right]D. \tag{C.4}$$

At $x = b$,

$$\frac{C}{\sqrt{l(b)}}e^{-i\frac{2}{3s}(\phi_b^{3/2}-\phi_a^{3/2})} + \frac{D}{\sqrt{l(b)}}e^{i\frac{2}{3s}(\phi_b^{3/2}-\phi_a^{3/2})} = \frac{F}{\sqrt{k}} \tag{C.5}$$

$$\left[i\sqrt{l(b)} - \frac{1}{2}(l(b))^{-3/2}\right]e^{-i\frac{2}{3s}(\phi_b^{3/2}-\phi_a^{3/2})}C + \left[-i\sqrt{l(b)} - \frac{1}{2}(l(b))^{-3/2}\right]e^{i\frac{2}{3s}(\phi_b^{3/2}-\phi_a^{3/2})}D = i\sqrt{k}F. \tag{C.6}$$

After some tedious calculation, we get from Eq. (C.3) and Eq. (C.4)

$$2i\sqrt{k}A = \left(i\frac{k}{\sqrt{l(a)}} + i\sqrt{l(a)} - \frac{1}{2}(l(a))^{-3/2}\right)C + \left(i\frac{k}{\sqrt{l(a)}} - i\sqrt{l(a)} - \frac{1}{2}(l(a))^{-3/2}\right)D, \tag{*}$$

and from Eq. (C.5) and Eq. (C.6)

$$C = \frac{1}{2i\sqrt{l(b)}}\left[i\sqrt{k} + \sqrt{\frac{l(b)}{k}}\left(i\sqrt{l(b)} + \frac{1}{2}(l(b))^{-3/2}\right)\right]e^{i\frac{2}{3s}(\phi_b^{3/2} - \phi_a^{3/2})}F$$

$$D = \frac{1}{2i\sqrt{l(b)}}\left[-i\sqrt{k} + \sqrt{\frac{l(b)}{k}}\left(i\sqrt{l(b)} - \frac{1}{2}(l(b))^{-3/2}\right)\right]e^{-i\frac{2}{3s}(\phi_b^{3/2} - \phi_a^{3/2})}F.$$

Thus, the transmission coefficient T can be found by plugging C and D into Eq (*) and calculating $|F/A|^2$. Figure C.2 shows the the transmission coefficient T as a function of the particle energy E with the linear slope equal to 0.1:

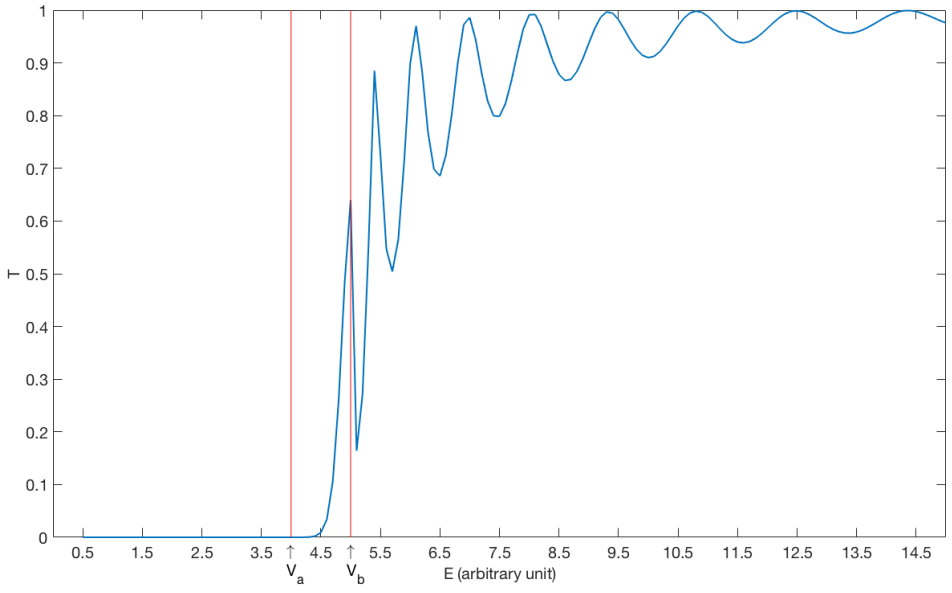

Figure C.2: Transmission coefficient as a function of the particle energy $T(E)$

C.2 Calculation of the Tunneling Current Density with the Transmission Coefficient

The tunneling current density is given by the Landauer formula:

$$J = -\sum_{k_y,\,k_z} \frac{2e}{Ah} \int (f_1(E) - f_2(E)) t(E_x) dE \tag{C.7}$$
$$= \frac{-e}{2\pi^2 h} \int_{-\infty}^{\infty} \int_{-\infty}^{\infty} \int_{U_0}^{\infty} (f_1 - f_2) t(E_x) dE dk_y dk_z,$$

where k_y and k_z are the wave vectors in the transverse plane, e is the elementary charge, A is the cross sectional area, h is the Planck constant and

$$f = \frac{1}{1 + \exp\left(\frac{E-\mu}{k_B T}\right)}$$

is the Fermi-Dirac distribution, describing the average number of fermions occupying a single-particle energy state.

Now we can further simplify the current density expression by calculating the integral in spherical coordinates as shown in Fig C.3. The total energy $E = \frac{\hbar^2}{2m}k^2 + U = \frac{\hbar^2}{2m}(k_x^2 + k_y^2 + k_z^2) + U$, where U is the potential energy in the region. The surface element $dk_y dk_z$ in spherical coordinates is equal to $k^2 \sin\theta d\phi d\theta$. Therefore,

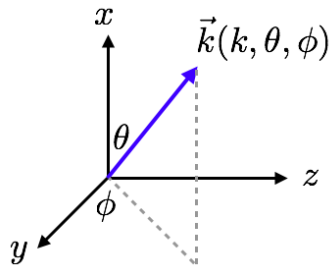

Figure C.3: Spherical coordinates

$$J = \frac{-e}{2\pi^2 h} \int_0^{2\pi} \int_0^{\frac{\pi}{2}} \int_{U_0}^{\infty} (f_1 - f_2) t(E_x) k^2 \sin\theta dE d\theta d\phi$$
$$= \frac{-em}{\pi^2 \hbar^3} \int_{U_0}^{\infty} (E - U)(f_1 - f_2) \int_0^{\frac{\pi}{2}} t(E_x) \sin\theta d\theta dE. \tag{C.8}$$

In order to calculate $t(E_x)$, we need to know how E_x changes with the incident angle θ,

which can be derived as follows. Note that U_0 is the zero potential reference of the system.

$$E_y + E_z = E_\perp = \frac{\hbar^2}{2m}(k_y^2 + k_z^2) = \frac{\hbar^2}{2m}(k^2 \sin^2\theta) = (E - U)\sin^2\theta$$

$$E_x = E - U_0 - (E_y + E_z) = (E - U_0) - (E - U)\sin^2\theta$$

REFERENCES

[1] G. E. Moore, "Cramming more components onto integrated circuits," *Electronics*, pp. 114–117, Apr. 1965.

[2] Gordon E. Moore, "Progress in digital integrated electronics [technical literaiture, copyright 1975 IEEE. reprinted, with permission. technical digest. international electron devices meeting, IEEE, 1975, pp. 11-13.]," *IEEE Solid-State Circuits Society Newsletter*, vol. 11, no. 3, pp. 36–37, 2006.

[3] W. M. Holt, "1.1 moore's law: A path going forward," in *2016 IEEE International Solid-State Circuits Conference (ISSCC)*, IEEE, 2016.

[4] *https://github.com/karlrupp/microprocessor-trend-data*.

[5] *https://en.wikichip.org/wiki/5_nm_lithography_process*.

[6] R. Dennard, F. Gaensslen, L. Kuhn, and H. Yu, "Design of micron MOS switching devices," in *1972 International Electron Devices Meeting*, IRE, 1972.

[7] S. G. Narendra, "Challenges and design choices in nanoscale CMOS," *ACM Journal on Emerging Technologies in Computing Systems*, vol. 1, no. 1, pp. 7–49, 2005.

[8] *https://www.karlrupp.net/2018/02/42-years-of-microprocessor-trend-data/*.

[9] *https://en.wikichip.org/wiki/technology_node*.

[10] P. Gupta and A. Kahng, "Manufacturing-aware physical design," in *ICCAD-2003. International Conference on Computer Aided Design (IEEE Cat. No.03CH37486)*, IEEE, 2003.

[11] Y. Nara, F. Ootsuka, S. Inumiya, and Y. Ohji, "High-k/metal gate stack technology for advanced CMOS," in *2006 8th International Conference on Solid-State and Integrated Circuit Technology Proceedings*, IEEE, 2006.

[12] Y. Nara, N. Mise, M. Kadoshima, T. Morooka, S. Kamiyama, T. Matsuki, M. Sato, T. Ono, T. Aoyama, T. Eimori, and Y. Ohji, "Gate-first high-k/metal gate stack for advanced CMOS technology," in *2008 9th International Conference on Solid-State and Integrated-Circuit Technology*, IEEE, 2008.

[13] D. Hisamoto, W.-C. Lee, J. Kedzierski, E. Anderson, H. Takeuchi, K. Asano, T.-J. King, J. Bokor, and C. Hu, "A folded-channel MOSFET for deep-sub-tenth micron era," in *International Electron Devices Meeting 1998. Technical Digest (Cat. No.98CH36217)*, IEEE, 1998.

[14] F.-L. Yang, H.-Y. Chen, F.-C. Chen, C.-C. Huang, C.-Y. Chang, H.-K. Chiu, C.-C. Lee, C.-C. Chen, H.-T. Huang, C.-J. Chen, H.-J. Tao, Y.-C. Yeo, M.-S. Liang, and C. Hu, "25 nm CMOS omega FETs," in *Digest. International Electron Devices Meeting,*, IEEE, 2002.

[15] F.-L. Yang, D.-H. Lee, H.-Y. Chen, C.-Y. Chang, S.-D. Liu, C.-C. Huang, T.-X. Chung, H.-W. Chen, C.-C. Huang, Y.-H. Liu, C.-C. Wu, C.-C. Chen, S.-C. Chen, Y.-T. Chen, Y.-H. Chen, C.-J. Chen, B.-W. Chan, P.-F. Hsu, J.-H. Shieh, H.-J. Tao, Y.-C. Yeo, Y. Li, J.-W. Lee, P. Chen, M.-S. Liang, and C. Hu, "5nm-gate nanowire FinFET," in *Digest of Technical Papers. 2004 Symposium on VLSI Technology, 2004.*, IEEE, 2004.

[16] P Razavi, G Fagas, I Ferain, N. D. Akhavan, R Yu, and J. P. Colinge, "Performance investigation of short-channel junctionless multigate transistors," in *Ulis 2011 Ultimate Integration on Silicon*, IEEE, 2011.

[17] D. J. Frank, "Power-constrained CMOS scaling limits," *IBM Journal of Research and Development*, vol. 46, no. 2.3, pp. 235–244, 2002.

[18] E. J. Nowak, "Maintaining the benefits of CMOS scaling when scaling bogs down," *IBM Journal of Research and Development*, vol. 46, no. 2.3, pp. 169–180, 2002.

[19] M. Horowitz, "1.1 computing's energy problem (and what we can do about it)," in *2014 IEEE International Solid-State Circuits Conference Digest of Technical Papers (ISSCC)*, IEEE, 2014.

[20] S. Salahuddin and S. Datta, "Use of negative capacitance to provide voltage amplification for low power nanoscale devices," *Nano Letters*, vol. 8, no. 2, pp. 405–410, 2008, doi: 10.1021/nl071804g. eprint: http://dx.doi.org/10.1021/nl071804g.

[21] *https://www.asml.com/en/technology/lithography-principles/rayleigh-criterion*.

[22] A. Tritchkov, S. Jeong, and C. Kenyon, "Lithography enabling for the 65 nm node gate layer patterning with alternating PSM," in *Optical Microlithography XVIII*, SPIE, 2005.

[23] S. Perlitz, U. Buttgereit, T. Scherbl, D. Seidel, K. M. Lee, and M. Tavassoli, "Novel solution for in-die phase control under scanner equivalent optical settings

for 45nm node and below," in *Photomask and Next-Generation Lithography Mask Technology XIV*, H. Watanabe, Ed., SPIE, 2007.

[24] A. B. Kahng, C.-H. Park, X. Xu, and H. Yao, "Layout decomposition for double patterning lithography," in *2008 IEEE/ACM International Conference on Computer-Aided Design*, IEEE, 2008.

[25] B. Yu, K. Yuan, D. Ding, and D. Z. Pan, "Layout decomposition for triple patterning lithography," *IEEE Transactions on Computer-Aided Design of Integrated Circuits and Systems*, vol. 34, no. 3, pp. 433–446, 2015.

[26] U. E. Avci, D. H. Morris, and I. A. Young, "Tunnel field-effect transistors: Prospects and challenges," *IEEE Journal of the Electron Devices Society*, vol. 3, no. 3, pp. 88–95, 2015.

[27] M. Dawber, K. M. Rabe, and J. F. Scott, "Physics of thin-film ferroelectric oxides," *Reviews of Modern Physics*, vol. 77, no. 4, pp. 1083–1130, 2005.

[28] B. H. Park, B. S. Kang, S. D. Bu, T. W. Noh, J. Lee, and W. Jo, "Lanthanum-substituted bismuth titanate for use in non-volatile memories," *Nature*, vol. 401, no. 6754, pp. 682–684, 1999.

[29] J. F. Scott, *Ferroelectric Memories*. Springer Berlin Heidelberg, 2000.

[30] H. Ishiwara and H. Ishiwara, "Recent progress in ferroelectric random access memory technology," *MRS Proceedings*, vol. 997, 2007.

[31] S. Das and J. Appenzeller, "FETRAM. an organic ferroelectric material based novel random access memory cell," *Nano Letters*, vol. 11, no. 9, pp. 4003–4007, 2011.

[32] *https://www.fujitsu.com/us/Images/MB85R4001A-DS501-00005-3v0-E.pdf*.

[33] D. D. Fong, "Ferroelectricity in ultrathin perovskite films," *Science*, vol. 304, no. 5677, pp. 1650–1653, Jun. 2004.

[34] C. Lichtensteiger, J.-M. Triscone, J. Junquera, and P. Ghosez, "Ferroelectricity and tetragonality in ultrathin $PbTiO_3$ films," *Physical Review Letters*, vol. 94, no. 4, p. 047 603, 2005.

[35] N. Sai, A. M. Kolpak, and A. M. Rappe, "Ferroelectricity in ultrathin perovskite films," *Physical Review B*, vol. 72, no. 2, p. 020 101, 2005.

[36] G. Gerra, A. K. Tagantsev, N. Setter, and K. Parlinski, "Ionic polarizability of conductive metal oxides and critical thickness for ferroelectricity inBaTiO3," *Physical Review Letters*, vol. 96, no. 10, p. 107 603, 2006.

[37] D. A. Tenne, A. Bruchhausen, N. D. Lanzillotti-Kimura, A. Fainstein, R. S. Katiyar, A. Cantarero, A. Soukiassian, V. Vaithyanathan, J. H. Haeni, W. Tian, D. G. Schlom, K. J. Choi, D. M. Kim, C. B. Eom, H. P. Sun, X. Q. Pan, Y. L. Li, L. Q. Chen, Q. X. Jia, S. M. Nakhmanson, K. M. Rabe, and X. X. Xi, "Probing nanoscale ferroelectricity by ultraviolet raman spectroscopy," *Science*, vol. 313, no. 5793, pp. 1614–1616, 2006.

[38] A. Chanthbouala, A. Crassous, V. Garcia, K. Bouzehouane, S. Fusil, X. Moya, J. Allibe, B. Dlubak, J. Grollier, S. Xavier, C. Deranlot, A. Moshar, R. Proksch, N. D. Mathur, M. Bibes, and A. Barthélémy, "Solid-state memories based on ferroelectric tunnel junctions," *Nature Nanotechnology*, vol. 7, no. 2, pp. 101–104, Dec. 2011.

[39] B. B. Tian, J. L. Wang, S. Fusil, Y. Liu, X. L. Zhao, S. Sun, H. Shen, T. Lin, J. L. Sun, C. G. Duan, M. Bibes, A. Barthélémy, B. Dkhil, V. Garcia, X. J. Meng, and J. H. Chu, "Tunnel electroresistance through organic ferroelectrics," *Nature Communications*, vol. 7, no. 1, May 2016.

[40] M. Y. Zhuravlev, R. F. Sabirianov, S. S. Jaswal, and E. Y. Tsymbal, "Giant electroresistance in ferroelectric tunnel junctions," *Physical Review Letters*, vol. 94, no. 24, p. 246 802, 2005.

[41] E. Y. Tsymbal, "APPLIED PHYSICS: Tunneling across a ferroelectric," *Science*, vol. 313, no. 5784, pp. 181–183, 2006.

[42] H. Yamada, V. Garcia, S. Fusil, S. Boyn, M. Marinova, A. Gloter, S. Xavier, J. Grollier, E. Jacquet, C. Carrétéro, C. Deranlot, M. Bibes, and A. Barthélémy, "Giant electroresistance of super-tetragonal $BiFeO_3$-based ferroelectric tunnel junctions," *ACS Nano*, vol. 7, no. 6, pp. 5385–5390, May 2013.

[43] V. Garcia and M. Bibes, "Ferroelectric tunnel junctions for information storage and processing," *Nature Communications*, 2014.

[44] Z. Xi, J. Ruan, C. Li, C. Zheng, Z. Wen, J. Dai, A. Li, and D. Wu, "Giant tunnelling electroresistance in metal/ferroelectric/semiconductor tunnel junctions by engineering the schottky barrier," *Nature Communications*, vol. 8, no. 1, 2017.

[45] S.-C. Chang, A. Naeemi, D. E. Nikonov, and A. Gruverman, "Theoretical approach to electroresistance in ferroelectric tunnel junctions," *Physical Review Applied*, vol. 7, no. 2, Feb. 2017.

[46] T. S. Böscke, J. Müller, D. Bräuhaus, U. Schröder, and U. Böttger, "Ferroelectricity in hafnium oxide thin films," *Applied Physics Letters*, vol. 99, no. 10, p. 102 903, Sep. 2011.

[47] J. Müller, T. S. Böscke, U. Schröder, S. Müller, D. Bräuhaus, U. Böttger, L. Frey, and T. Mikolajick, "Ferroelectricity in simple binary ZrO_2 and HfO_2," *Nano Letters*, vol. 12, no. 8, pp. 4318–4323, 2012.

[48] P. Sharma, K. Tapily, A. K. Saha, J. Zhang, A. Shaughnessy, A. Aziz, G. L. Snider, S. Gupta, R. D. Clark, and S. Datta, "Impact of total and partial dipole switching on the switching slope of gate-last negative capacitance FETs with ferroelectric hafnium zirconium oxide gate stack," in *2017 Symposium on VLSI Technology*, IEEE, 2017.

[49] E. Yurchuk, J. Muller, S. Muller, J. Paul, M. Pesic, R. van Bentum, U. Schroeder, and T. Mikolajick, "Charge-trapping phenomena in HfO_2-based FeFET-type nonvolatile memories," *IEEE Transactions on Electron Devices*, vol. 63, no. 9, pp. 3501–3507, 2016.

[50] S. A. Wolf, "Spintronics: A spin-based electronics vision for the future," *Science*, vol. 294, no. 5546, pp. 1488–1495, 2001.

[51] D. Ralph and M. Stiles, "Spin transfer torques," *Journal of Magnetism and Magnetic Materials*, vol. 320, no. 7, pp. 1190–1216, 2008.

[52] J. E. Hirsch, "Spin hall effect," *Physical Review Letters*, vol. 83, no. 9, pp. 1834–1837, 1999.

[53] K. Garello, I. M. Miron, C. O. Avci, F. Freimuth, Y. Mokrousov, S. Blgel, S. Auffret, O. Boulle, G. Gaudin, and P. Gambardella, "Symmetry and magnitude of spin–orbit torques in ferromagnetic heterostructures," *Nature Nanotechnology*, vol. 8, no. 8, pp. 587–593, 2013.

[54] M. Fiebig, "Revival of the magnetoelectric effect," *Journal of Physics D: Applied Physics*, vol. 38, no. 8, R123–R152, 2005.

[55] S. S. P. Parkin, C. Kaiser, A. Panchula, P. M. Rice, B. Hughes, M. Samant, and S.-H. Yang, "Giant tunnelling magnetoresistance at room temperature with MgO (100) tunnel barriers," *Nature Materials*, vol. 3, no. 12, pp. 862–867, 2004.

[56] B. Behin-Aein, D. Datta, S. Salahuddin, and S. Datta, "Proposal for an all-spin logic device with built-in memory," *Nature Nanotechnology*, vol. 5, no. 4, pp. 266–270, 2010.

[57] J. T. Heron, J. L. Bosse, Q. He, Y. Gao, M. Trassin, L. Ye, J. D. Clarkson, C. Wang, J. Liu, S. Salahuddin, D. C. Ralph, D. G. Schlom, J. Íñiguez, B. D. Huey, and R. Ramesh, "Deterministic switching of ferromagnetism at room temperature using an electric field," *Nature*, vol. 516, no. 7531, pp. 370–373, Dec. 2014.

[58] Y.-C. Liao, D. E. Nikonov, S. Dutta, S.-C. Chang, C.-S. Hsu, I. A. Young, and A. Naeemi, "Understanding the switching mechanisms of the antiferromagnet/ferromagnet heterojunction," *Nano Letters*, vol. 20, no. 11, pp. 7919–7926, 2020.

[59] K. Bernstein, R. K. Cavin, W. Porod, A. Seabaugh, and J. Welser, "Device and architecture outlook for beyond CMOS switches," *Proceedings of the IEEE*, vol. 98, no. 12, pp. 2169–2184, 2010.

[60] D. E. Nikonov and I. A. Young, "Overview of beyond-CMOS devices and a uniform methodology for their benchmarking," *Proceedings of the IEEE*, vol. 101, no. 12, pp. 2498–2533, 2013.

[61] A. Chen, "Emerging research device roadmap and perspectives," in *2014 IEEE International Conference on IC Design & Technology*, IEEE, 2014.

[62] D. E. Nikonov and I. A. Young, "Benchmarking of beyond-CMOS exploratory devices for logic integrated circuits," *IEEE Journal on Exploratory Solid-State Computational Devices and Circuits*, vol. 1, pp. 3–11, 2015.

[63] J. Valasek, "Piezo-electric and allied phenomena in rochelle salt.," *MSc thesis, Univ. Minnesota*, 1920.

[64] L. D. Landau, "On the theory of phase transitions.," *Zh. Eksp. Teor. Fiz*, vol. 7, pp. 19–32, 1937.

[65] V. L. Ginzburg, "On the dielectric properties of ferroelectric (segnette-electric) crystals and barium titanate.," *Zh. Eksp. Teor. Fiz*, vol. 15, pp. 739–749, 1945.

[66] A. Devonshire, "XCVI. Theory of barium titanate: Part I," *The London, Edinburgh, and Dublin Philosophical Magazine and Journal of Science*, vol. 40, no. 309, pp. 1040–1063, Jul. 1949, doi: 10.1080/14786444908561372.

[67] N. A. Pertsev, A. G. Zembilgotov, and A. K. Tagantsev, "Effect of mechanical boundary conditions on phase diagrams of epitaxial ferroelectric thin films," *Physical Review Letters*, vol. 80, no. 9, pp. 1988–1991, Mar. 1998.

[68] M. J. Haun, E. Furman, S. J. Jang, H. A. McKinstry, and L. E. Cross, "Thermodynamic theory of $PbTiO_3$," *Journal of Applied Physics*, vol. 62, no. 8, pp. 3331–3338, Oct. 1987.

[69] L. D. Landau and I. M. Khalatnikov, *Dok. Akad. Nauk SSSR.*, vol. 46, pp. 469–472, 1954.

[70] A. K. Tagantsev, "Landau expansion for ferroelectrics: Which variable to use?" *Ferroelectrics*, vol. 375, no. 1, pp. 19–27, Dec. 2008.

[71] L.-Q. Chen, "APPENDIX a – landau free-energy coefficients," in *Topics in Applied Physics*, Springer Berlin Heidelberg, 2007, pp. 363–372.

[72] J. Hiltunen, J. Lappalainen, J. Puustinen, V. Lantto, and H. Tuller, "Size-dependent optical properties of $BaTiO_3$ - $SrTiO_3$ superlattices," *Optics Express*, vol. 16, no. 11, p. 8219, 2008.

[73] K. Ni, M. Jerry, J. A. Smith, and S. Datta, "A circuit compatible accurate compact model for ferroelectric-FETs," in *2018 IEEE Symposium on VLSI Technology*, IEEE, 2018.

[74] D. Delmonte, *Combined magnetic, electric, ferroelectric and magnetoelectric characterization of novel multiferroic perovskites obtained by high pressure/temperature synthesis*, 2015.

[75] J. Wang, "Epitaxial $BiFeO_3$ multiferroic thin film heterostructures," *Science*, vol. 299, no. 5613, pp. 1719–1722, Mar. 2003.

[76] J. F. Scott, "Room-temperature multiferroic magnetoelectrics," *NPG Asia Materials*, vol. 5, no. 11, e72–e72, Nov. 2013.

[77] A. V. Bune, V. M. Fridkin, S. Ducharme, L. M. Blinov, S. P. Palto, A. V. Sorokin, S. G. Yudin, and A. Zlatkin, "Two-dimensional ferroelectric films," *Nature*, vol. 391, no. 6670, pp. 874–877, Feb. 1998.

[78] J. Choi, G. Khara, Y. Song, and Y. Zhao, "Nonlinear electrical dipolar switching at single molecular scale," *Chemical Physics Letters*, vol. 410, no. 4-6, pp. 339–342, Jul. 2005.

[79] K. Majumdar, S. Datta, and S. P. Rao, "Revisiting the theory of ferroelectric negative capacitance," *IEEE Transactions on Electron Devices*, vol. 63, no. 5, pp. 2043–2049, May 2016.

[80] L.-Q. Chen, "Phase-field method of phase transitions/domain structures in ferroelectric thin films: A review," *Journal of the American Ceramic Society*, vol. 91, no. 6, pp. 1835–1844, Jun. 2008.

[81] S. J. Kim, J. Mohan, S. R. Summerfelt, and J. Kim, "Ferroelectric $Hf_{0.5}Zr_{0.5}O_2$ thin films: A review of recent advances," *JOM*, vol. 71, no. 1, pp. 246–255, Sep. 2018.

[82] H. Mulaosmanovic, S. Slesazeck, J. Ocker, M. Pesic, S. Muller, S. Flachowsky, J. Muller, P. Polakowski, J. Paul, S. Jansen, S. Kolodinski, C. Richter, S. Piontek, T. Schenk, A. Kersch, C. Kunneth, R. van Bentum, U. Schroder, and T. Mikolajick, "Evidence of single domain switching in hafnium oxide based FeFETs: Enabler for multi-level FeFET memory cells," in *2015 IEEE International Electron Devices Meeting (IEDM)*, IEEE, 2015.

[83] H. Mulaosmanovic, J. Ocker, S. Mller, U. Schroeder, J. Mller, P. Polakowski, S. Flachowsky, R. van Bentum, T. Mikolajick, and S. Slesazeck, "Switching kinetics in nanoscale hafnium oxide based ferroelectric field-effect transistors," *ACS Applied Materials & Interfaces*, vol. 9, no. 4, pp. 3792–3798, 2017.

[84] K. Ni, A. Saha, W. Chakraborty, H. Ye, B. Grisafe, J. Smith, G. B. Rayner, S. Gupta, and S. Datta, "Equivalent oxide thickness (EOT) scaling with hafnium zirconium oxide high-κ dielectric near morphotropic phase boundary," in *2019 IEEE International Electron Devices Meeting (IEDM)*, IEEE, 2019.

[85] A. Kolmogorov, "On the Statistical Theory of Metal Crystallization," *Izv. Akad. Nauk SSSR, Ser. Math*, vol. 1, pp. 335–360, 1937, Computes density of fairly general Johnson-Mehl crystals and the probability that a point is not in a crystal yet.

[86] M. Avrami, "Kinetics of phase change. II transformation-time relations for random distribution of nuclei," *The Journal of Chemical Physics*, vol. 8, no. 2, pp. 212–224, 1940.

[87] ——, "Granulation, phase change, and microstructure kinetics of phase change. III," *The Journal of Chemical Physics*, vol. 9, no. 2, pp. 177–184, 1941.

[88] Y. Ishibashi and Y. Takagi, "Note on ferroelectric domain switching," *Journal of the Physical Society of Japan*, vol. 31, no. 2, pp. 506–510, Aug. 1971.

[89] B. J. Rodriguez, S. Jesse, A. P. Baddorf, S. H. Kim, and S. V. Kalinin, "Controlling polarization dynamics in a liquid environment: From localized to macroscopic switching in ferroelectrics," *Physical Review Letters*, vol. 98, no. 24, Jun. 2007.

[90] G. Catalan, H. Béa, S. Fusil, M. Bibes, P. Paruch, A. Barthélémy, and J. F. Scott, "Fractal dimension and size scaling of domains in thin films of multiferroic $BiFeO_3$," *Physical Review Letters*, vol. 100, no. 2, Jan. 2008.

[91] J. Y. Jo, S. M. Yang, T. H. Kim, H. N. Lee, J.-G. Yoon, S. Park, Y. Jo, M. H. Jung, and T. W. Noh, "Nonlinear dynamics of domain-wall propagation in epitaxial ferroelectric thin films," *Physical Review Letters*, vol. 102, no. 4, Jan. 2009.

[92] O. Lohse, M. Grossmann, U. Boettger, D. Bolten, and R. Waser, "Relaxation mechanism of ferroelectric switching in $Pb(Zr,Ti)O_3$ thin films," *Journal of Applied Physics*, vol. 89, no. 4, pp. 2332–2336, 2001.

[93] A. K. Tagantsev, I. Stolichnov, N. Setter, J. S. Cross, and M. Tsukada, "Non-kolmogorov-avrami switching kinetics in ferroelectric thin films," *Physical Review B*, vol. 66, no. 21, p. 214 109, 2002.

[94] J. Y. Jo, H. S. Han, J.-G. Yoon, T. K. Song, S.-H. Kim, and T. W. Noh, "Domain switching kinetics in disordered ferroelectric thin films," *Physical Review Letters*, vol. 99, no. 26, p. 267 602, 2007.

[95] D. S. Jeong, R. Thomas, R. S. Katiyar, J. F. Scott, H Kohlstedt, A Petraru, and C. S. Hwang, "Emerging memories: Resistive switching mechanisms and current status," *Reports on Progress in Physics*, vol. 75, no. 7, p. 076 502, Jun. 2012.

[96] Z. Wen and D. Wu, "Ferroelectric tunnel junctions: Modulations on the potential barrier," *Advanced Materials*, p. 1 904 123, 2019.

[97] Z. Wen, C. Li, D. Wu, A. Li, and N. Ming, "Ferroelectric-field-effect-enhanced electroresistance in metal/ferroelectric/semiconductor tunnel junctions," *Nature Materials*, vol. 12, no. 7, pp. 617–621, May 2013.

[98] G. Pahwa, T. Dutta, A. Agarwal, and Y. S. Chauhan, "Compact model for ferroelectric negative capacitance transistor with MFIS structure," *IEEE Transactions on Electron Devices*, vol. 64, no. 3, pp. 1366–1374, Mar. 2017.

[99] M. A. Alam, M. Si, and P. D. Ye, "A critical review of recent progress on negative capacitance field-effect transistors," *Applied Physics Letters*, vol. 114, no. 9, p. 090 401, Mar. 2019.

[100] A. I. Khan, D. Bhowmik, P. Yu, S. J. Kim, X. Pan, R. Ramesh, and S. Salahuddin, "Experimental evidence of ferroelectric negative capacitance in nanoscale heterostructures," *Applied Physics Letters*, vol. 99, no. 11, p. 113 501, Sep. 2011.

[101] D. J. R. Appleby, N. K. Ponon, K. S. K. Kwa, B. Zou, P. K. Petrov, T. Wang, N. M. Alford, and A. O'Neill, "Experimental observation of negative capacitance in ferroelectrics at room temperature," *Nano Letters*, vol. 14, no. 7, pp. 3864–3868, Jun. 2014.

[102] W. Gao, A. Khan, X. Marti, C. Nelson, C. Serrao, J. Ravichandran, R. Ramesh, and S. Salahuddin, "Room-temperature negative capacitance in a ferroelectric–dielectric superlattice heterostructure," *Nano Letters*, vol. 14, no. 10, pp. 5814–5819, Sep. 2014.

[103] P. Zubko, J. C. Wojdeł, M. Hadjimichael, S. Fernandez-Pena, A. Sené, I. Luk'yanchuk, J.-M. Triscone, and J. Íñiguez, "Negative capacitance in multidomain ferroelectric superlattices," *Nature*, vol. 534, no. 7608, pp. 524–528, Jun. 2016.

[104] Z. Liu, M. A. Bhuiyan, and T. P. Ma, "A critical examination of 'quasi-static negative capacitance' (QSNC) theory," in *2018 IEEE International Electron Devices Meeting (IEDM)*, IEEE, Dec. 2018.

[105] A. I. Khan, K. Chatterjee, B. Wang, S. Drapcho, L. You, C. Serrao, S. R. Bakaul, R. Ramesh, and S. Salahuddin, "Negative capacitance in a ferroelectric capacitor," *Nature Materials*, vol. 14, no. 2, pp. 182–186, Dec. 2014.

[106] M. Hoffmann, F. P. G. Fengler, M. Herzig, T. Mittmann, B. Max, U. Schroeder, R. Negrea, P. Lucian, S. Slesazeck, and T. Mikolajick, "Unveiling the double-well energy landscape in a ferroelectric layer," *Nature*, vol. 565, no. 7740, pp. 464–467, Jan. 2019.

[107] S.-C. Chang, U. E. Avci, D. E. Nikonov, S. Manipatruni, and I. A. Young, "Physical origin of transient negative capacitance in a ferroelectric capacitor," *Physical Review Applied*, vol. 9, no. 1, Jan. 2018.

[108] A. I. Khan, M. Hoffmann, K. Chatterjee, Z. Lu, R. Xu, C. Serrao, S. Smith, L. W. Martin, C. Hu, R. Ramesh, and S. Salahuddin, "Differential voltage amplification from ferroelectric negative capacitance," *Applied Physics Letters*, vol. 111, no. 25, p. 253 501, Dec. 2017.

[109] Z. Krivokapic, U. Rana, R. Galatage, A. Razavieh, A. Aziz, J. Liu, J. Shi, H. J. Kim, R. Sporer, C. Serrao, A. Busquet, P. Polakowski, J. Muller, W. Kleemeier, A. Jacob, D. Brown, A. Knorr, R. Carter, and S. Banna, "14nm ferroelectric FinFET technology with steep subthreshold slope for ultra low power applications," in *2017 IEEE International Electron Devices Meeting (IEDM)*, IEEE, Dec. 2017.

[110] G. A. Salvatore, D. Bouvet, and A. M. Ionescu, "Demonstration of subthrehold swing smaller than 60mv/decade in Fe-FET with P(VDF-TrFE)/SiO_2 gate stack," in *2008 IEEE International Electron Devices Meeting*, IEEE, 2008.

[111] A. Rusu, G. A. Salvatore, D. Jimenez, and A. M. Ionescu, "Metal-ferroelectric-meta-oxide-semiconductor field effect transistor with sub-60mv/decade subthreshold swing and internal voltage amplification," in *2010 International Electron Devices Meeting*, IEEE, Dec. 2010.

[112] A. I. Khan, K. Chatterjee, J. P. Duarte, Z. Lu, A. Sachid, S. Khandelwal, R. Ramesh, C. Hu, and S. Salahuddin, "Negative capacitance in short-channel FinFETs

externally connected to an epitaxial ferroelectric capacitor," *IEEE Electron Device Letters*, vol. 37, no. 1, pp. 111–114, Jan. 2016.

[113] J. Jo and C. Shin, "Negative capacitance field effect transistor with hysteresis-free sub-60-mV/decade switching," *IEEE Electron Device Letters*, vol. 37, no. 3, pp. 245–248, Mar. 2016.

[114] Z. C. Yuan, S. Rizwan, M. Wong, K. Holland, S. Anderson, T. B. Hook, D. Kienle, S. Gadelrab, P. S. Gudem, and M. Vaidyanathan, "Switching-speed limitations of ferroelectric negative-capacitance FETs," *IEEE Transactions on Electron Devices*, vol. 63, no. 10, pp. 4046–4052, Oct. 2016.

[115] M. H. Lee, S.-T. Fan, C.-H. Tang, P.-G. Chen, Y.-C. Chou, H.-H. Chen, J.-Y. Kuo, M.-J. Xie, S.-N. Liu, M.-H. Liao, C.-A. Jong, K.-S. Li, M.-C. Chen, and C. W. Liu, "Physical thickness 1.x nm ferroelectric HfZrOx negative capacitance FETs," in *2016 IEEE International Electron Devices Meeting (IEDM)*, IEEE, Dec. 2016.

[116] M. Hoffmann, B. Max, T. Mittmann, U. Schroeder, S. Slesazeck, and T. Mikolajick, "Demonstration of high-speed hysteresis-free negative capacitance in ferroelectric $Hf_{0.5}Zr_{0.5}O_2$," in *2018 IEEE International Electron Devices Meeting (IEDM)*, IEEE, Dec. 2018.

[117] A. Aziz, S. Ghosh, S. Datta, and S. Gupta, "Physics-based circuit-compatible SPICE model for ferroelectric transistors," *IEEE Electron Device Letters*, pp. 1–1, Jun. 2016.

[118] C.-S. Hsu, C. Pan, and A. Naeemi, "Performance analysis and enhancement of negative capacitance logic devices based on internally resistive ferroelectrics," *IEEE Electron Device Letters*, vol. 39, no. 5, pp. 765–768, May 2018.

[119] S. Deng, Z. Jiang, S. Dutta, H. Ye, W. Chakraborty, S. Kurinec, S. Datta, and K. Ni, "Examination of the interplay between polarization switching and charge trapping in ferroelectric FET," in *2020 IEEE International Electron Devices Meeting (IEDM)*, IEEE, 2020.

[120] D Sando, A Barthélémy, and M Bibes, "$BiFeO_3$ epitaxial thin films and devices: Past, present and future," *Journal of Physics: Condensed Matter*, vol. 26, no. 47, p. 473 201, 2014.

[121] Y. Yang, I. C. Infante, B. Dkhil, and L. Bellaiche, "Strain effects on multiferroic $BiFeO_3$ films," *Comptes Rendus Physique*, vol. 16, no. 2, pp. 193–203, 2015.

[122] Y.-C. Liao, D. E. Nikonov, S. Dutta, S.-C. Chang, S. Manipatruni, I. A. Young, and A. Naeemi, "Simulation of the magnetization dynamics of a single-domain $BiFeO_3$ nanoisland," *IEEE Transactions on Magnetics*, vol. 56, no. 10, pp. 1–9, 2020.

[123] F. Bai, J. Wang, M. Wuttig, J. Li, N. Wang, A. P. Pyatakov, A. K. Zvezdin, L. E. Cross, and D. Viehland, "Destruction of spin cycloid in (111)c-oriented $BiFeO_3$ thin films by epitiaxial constraint: Enhanced polarization and release of latent magnetization," *Applied Physics Letters*, vol. 86, no. 3, p. 032 511, 2005.

[124] J. T. Heron, M. Trassin, K. Ashraf, M. Gajek, Q. He, S. Y. Yang, D. E. Nikonov, Y.-H. Chu, S. Salahuddin, and R. Ramesh, "Electric-field-induced magnetization reversal in a ferromagnet-multiferroic heterostructure," *Physical Review Letters*, vol. 107, no. 21, p. 217 202, 2011.

[125] J. T. Heron, D. G. Schlom, and R. Ramesh, "Electric field control of magnetism using $BiFeO_3$-based heterostructures," *Applied Physics Reviews*, vol. 1, no. 2, p. 021 303, 2014.

[126] Y. Li, Y. Lian, K. Yao, and G. S. Samudra, "Evaluation and optimization of short channel ferroelectric mosfet for low power circuit application with bsim4 and landau theory," *Solid-State Electronics*, vol. 114, pp. 17 –22, 2015, doi: 10.1016/j.sse.2015.07.001.

[127] J. Seo, J. Lee, and M. Shin, "Analysis of drain-induced barrier rising in short-channel negative-capacitance fets and its applications," *IEEE Transactions on Electron Devices*, vol. 64, no. 4, pp. 1793–1798, Apr. 2017, doi: 10.1109/TED.2017.2658673.

[128] G. Pahwa, T. Dutta, A. Agarwal, S. Khandelwal, S. Salahuddin, C. Hu, and Y. S. Chauhan, "Analysis and compact modeling of negative capacitance transistor with high on-current and negative output differential resistance—Part I: Model description," *IEEE Transactions on Electron Devices*, vol. 63, no. 12, pp. 4981–4985, Dec. 2016, doi: 10.1109/TED.2016.2614432.

[129] S. Khandelwal, A. Khan, J. Duarte, A. Sachid, S. Salahuddin, and C. Hu, "Circuit performance analysis of negative capacitance finfets," in *2016 Symposium on VLSI Technology*. United States: Institute of Electrical and Electronics Engineers (IEEE), Sep. 2016, pp. 1–2.

[130] G. Pahwa, T. Dutta, A. Agarwal, and Y. S. Chauhan, "Designing energy efficient and hysteresis free negative capacitance finfet with negative dibl and 3.5x ion using compact modeling approach," in *ESSCIRC Conference 2016: 42nd European Solid-State Circuits Conference*, doi: 10.1109/ESSCIRC.2016.7598240, Sep. 2016, pp. 49–54.

[131] S. Gupta, M. Steiner, A. Aziz, V. Narayanan, S. Datta, and S. K. Gupta, "Device-circuit analysis of ferroelectric fets for low-power logic," *IEEE Transactions on Electron Devices*, vol. 64, no. 8, pp. 3092–3100, Aug. 2017, doi: 10.1109/TED.2017.2717929.

[132] G. Pahwa, T. Dutta, A. Agarwal, and Y. S. Chauhan, "Energy-delay tradeoffs in negative capacitance finfet based cmos circuits," in *2016 3rd International Conference on Emerging Electronics (ICEE)*, doi: 10.1109/ICEmElec.2016.8074416, Dec. 2016, pp. 1–4.

[133] M. Kobayashi, N. Ueyama, K. Jang, and T. Hiramoto, "Experimental study on polarization-limited operation speed of negative capacitance FET with ferroelectric HfO_2," in *2016 IEEE International Electron Devices Meeting (IEDM)*, IEEE, Dec. 2016.

[134] W. Zhao and Y. Cao, "Predictive technology model for nano-cmos design exploration," *J. Emerg. Technol. Comput. Syst.*, vol. 3, no. 1, Apr. 2007, doi: 10.1145/1229175.1229176.

[135] A. I. Khan, U. Radhakrishna, K. Chatterjee, S. Salahuddin, and D. A. Antoniadis, "Negative capacitance behavior in a leaky ferroelectric," *IEEE Transactions on Electron Devices*, vol. 63, no. 11, pp. 4416–4422, Nov. 2016, doi: 10.1109/TED.2016.2612656.

[136] C. Pan and A. Naeemi, "Interconnect design and benchmarking for charge-based beyond-cmos device proposals," *IEEE Electron Device Letters*, vol. 37, no. 4, pp. 508–511, 2016, doi: 10.1109/LED.2016.2532350.

[137] G. Moore, "Cramming more components onto integrated circuits," *Proceedings of the IEEE*, vol. 86, no. 1, pp. 82–85, Jan. 1998, doi: 10.1109/jproc.1998.658762.

[138] M. Hoffmann, M. Pešić, K. Chatterjee, A. I. Khan, S. Salahuddin, S. Slesazeck, U. Schroeder, and T. Mikolajick, "Direct observation of negative capacitance in polycrystalline ferroelectric HfO_2," *Adv. Funct. Mater.*, vol. 26, no. 47, pp. 8643–8649, Oct. 2016, doi: 10.1002/adfm.201602869.

[139] S.-C. Chang, U. E. Avci, D. E. Nikonov, and I. A. Young, "A thermodynamic perspective of negative-capacitance field-effect transistors," *IEEE Journal on Exploratory Solid-State Computational Devices and Circuits*, vol. 3, pp. 56–64, Dec. 2017, doi: 10.1109/jxcdc.2017.2750108.

[140] A. K. Saha, K. Ni, S. Dutta, S. Datta, and S. Gupta, "Phase field modeling of domain dynamics and polarization accumulation in ferroelectric HZO," *Appl. Phys. Lett.*, vol. 114, no. 20, p. 202 903, May 2019, doi: 10.1063/1.5092707.

[141] B. Obradovic, T. Rakshit, R. Hatcher, J. A. Kittl, and M. S. Rodder, "Modeling transient negative capacitance in steep-slope FeFETs," *IEEE Transactions on Electron Devices*, vol. 65, no. 11, pp. 5157–5164, Nov. 2018, doi: 10.1109/TED.2018.2868479.

[142] Y. J. Kim, H. W. Park, S. D. Hyun, H. J. Kim, K. D. Kim, Y. H. Lee, T. Moon, Y. B. Lee, M. H. Park, and C. S. Hwang, "Voltage drop in a ferroelectric single layer capacitor by retarded domain nucleation," *Nano Lett.*, vol. 17, no. 12, pp. 7796–7802, Nov. 2017, doi: 10.1021/acs.nanolett.7b04008.

[143] H. Asai, K. Fukuda, J. Hattori, H. Koike, N. Miyata, M. Takahashi, and S. Sakai, "Compact model of ferroelectric-gate field-effect transistor for circuit simulation based on multidomain landau–kalathnikov theory," *Japanese Journal of Applied Physics*, vol. 56, no. 4S, 04CE07, Mar. 2017, doi: 10.7567/jjap.56.04ce07.

[144] S. Nambu and D. A. Sagala, "Domain formation and elastic long-range interaction in ferroelectric perovskites," *Physical Review B*, vol. 50, no. 9, pp. 5838–5847, Sep. 1994.

[145] H.-L. Hu and L.-Q. Chen, "Three-dimensional computer simulation of ferroelectric domain formation," *Journal of the American Ceramic Society*, vol. 81, no. 3, pp. 492–500, Jan. 2005.

[146] Y. Li, S. Hu, Z. Liu, and L. Chen, "Effect of substrate constraint on the stability and evolution of ferroelectric domain structures in thin films," *Acta Materialia*, vol. 50, no. 2, pp. 395–411, Jan. 2002.

[147] Y. L. Li, S. Y. Hu, Z. K. Liu, and L. Q. Chen, "Phase-field model of domain structures in ferroelectric thin films," *Applied Physics Letters*, vol. 78, no. 24, pp. 3878–3880, Jun. 2001.

[148] L. Hong, A. Soh, Y. Song, and L. Lim, "Interface and surface effects on ferroelectric nano-thin films," *Acta Materialia*, vol. 56, no. 13, pp. 2966–2974, Aug. 2008.

[149] Y. L. Li, S. Y. Hu, Z. K. Liu, and L. Q. Chen, "Effect of electrical boundary conditions on ferroelectric domain structures in thin films," *Applied Physics Letters*, vol. 81, no. 3, pp. 427–429, Jul. 2002.

[150] H. Agarwal, P. Kushwaha, Y.-K. Lin, M.-Y. Kao, Y.-H. Liao, A. Dasgupta, S. Salahuddin, and C. Hu, "Proposal for capacitance matching in negative capacitance field-effect transistors," *IEEE Electron Device Letters*, vol. 40, no. 3, pp. 463–466, Mar. 2019.

[151] L. Chen and J. Shen, "Applications of semi-implicit fourier-spectral method to phase field equations," *Computer Physics Communications*, vol. 108, no. 2-3, pp. 147–158, Feb. 1998.

[152] S. Dutta, D. E. Nikonov, S. Manipatruni, I. A. Young, and A. Naeemi, "SPICE circuit modeling of PMA spin wave bus excited using magnetoelectric effect,"

IEEE Transactions on Magnetics, vol. 50, no. 9, pp. 1–11, Sep. 2014, doi: 10.1109/tmag.2014.2320942.

[153] S. K. Streiffer, J. A. Eastman, D. D. Fong, C. Thompson, A. Munkholm, M. V. R. Murty, O. Auciello, G. R. Bai, and G. B. Stephenson, "Observation of nanoscale180°stripe domains in ferroelectric $PbTiO_3$ thin films," *Physical Review Letters*, vol. 89, no. 6, Jul. 2002.

[154] G. B. Stephenson and K. R. Elder, "Theory for equilibrium 180° stripe domains in $PbTiO_3$ films," *Journal of Applied Physics*, vol. 100, no. 5, p. 051 601, Sep. 2006.

[155] P. Gao, C. T. Nelson, J. R. Jokisaari, S.-H. Baek, C. W. Bark, Y. Zhang, E. Wang, D. G. Schlom, C.-B. Eom, and X. Pan, "Revealing the role of defects in ferroelectric switching with atomic resolution," *Nature Communications*, vol. 2, no. 1, Sep. 2011, doi: 10.1038/ncomms1600.

[156] G. Li, X. Huang, J. Hu, and W. Zhang, "Shear-strain gradient induced polarization reversal in ferroelectric $BaTiO_3$ thin films: A first-principles total-energy study," *Phys. Rev. B*, vol. 95, no. 14, Apr. 2017, doi: 10.1103/physrevb.95.144111.

[157] W. J. Merz, "Domain formation and domain wall motions in ferroelectric $BaTiO_3$ single crystals," *Physical Review*, vol. 95, no. 3, pp. 690–698, Aug. 1954, doi: 10.1103/PhysRev.95.690.

[158] M. Pešić, C. Künneth, M. Hoffmann, H. Mulaosmanovic, S. Müller, E. T. Breyer, U. Schroeder, A. Kersch, T. Mikolajick, and S. Slesazeck, "A computational study of hafnia-based ferroelectric memories: From ab initio via physical modeling to circuit models of ferroelectric device," *Journal of Computational Electronics*, vol. 16, no. 4, pp. 1236–1256, Aug. 2017, doi: 10.1007/s10825-017-1053-0.

[159] A. T. Bartic, D. J. Wouters, H. E. Maes, J. T. Rickes, and R. M. Waser, "Preisach model for the simulation of ferroelectric capacitors," *Journal of Applied Physics*, vol. 89, no. 6, pp. 3420–3425, Mar. 2001, doi: 10.1063/1.1335639.

[160] M. H. Park, Y. H. Lee, H. J. Kim, T. Schenk, W. Lee, K. D. Kim, F. P. G. Fengler, T. Mikolajick, U. Schroeder, and C. S. Hwang, "Surface and grain boundary energy as the key enabler of ferroelectricity in nanoscale hafnia-zirconia: A comparison of model and experiment," *Nanoscale*, vol. 9, no. 28, pp. 9973–9986, 2017, doi: 10.1039/C7NR02121F.

[161] P. Fedeli, M. Kamlah, and A. Frangi, "Phase-field modeling of domain evolution in ferroelectric materials in the presence of defects," *Smart Materials and Structures*, vol. 28, no. 3, p. 035 021, Feb. 2019, doi: 10.1088/1361-665X/aafff8.

[162] N. S. Kim, T. Austin, D. Blaauw, T. Mudge, K. Flautner, J. S. Hu, M. Irwin, M. Kandemir, and V. Narayanan, "Leakage current: Moore's law meets static power," *Computer*, vol. 36, no. 12, pp. 68–75, 2003.

[163] K. Ni, P. Sharma, J. Zhang, M. Jerry, J. A. Smith, K. Tapily, R. Clark, S. Mahapatra, and S. Datta, "Critical role of interlayer in $Hf_{0.5}Zr_{0.5}O_2$ ferroelectric FET nonvolatile memory performance," *IEEE Transactions on Electron Devices*, vol. 65, no. 6, pp. 2461–2469, 2018.

[164] Y. J. Kim, H. Yamada, T. Moon, Y. J. Kwon, C. H. An, H. J. Kim, K. D. Kim, Y. H. Lee, S. D. Hyun, M. H. Park, and C. S. Hwang, "Time-dependent negative capacitance effects in $Al_2O_3/BaTiO_3$ bilayers," *Nano Letters*, vol. 16, no. 7, pp. 4375–4381, 2016.

[165] K. D. Kim, Y. J. Kim, M. H. Park, H. W. Park, Y. J. Kwon, Y. B. Lee, H. J. Kim, T. Moon, Y. H. Lee, S. D. Hyun, B. S. Kim, and C. S. Hwang, "Transient negative capacitance effect in atomic-layer-deposited $Al_2O_3/Hf_{0.3}Zr_{0.7}O_2$ bilayer thin film," *Advanced Functional Materials*, vol. 29, no. 17, p. 1 808 228, 2019.

[166] C.-S. Hsu, S.-C. Chang, D. E. Nikonov, I. A. Young, and A. Naeemi, "A theoretical study of multidomain ferroelectric switching dynamics with a physics-based SPICE circuit model for phase-field simulations," *IEEE Transactions on Electron Devices*, vol. 67, no. 7, pp. 2952–2959, 2020.

[167] Z. Liu, H. Jiang, B. Ordway, and T. P. Ma, "Unveiling the apparent "negative capacitance" effects resulting from pulse measurements of ferroelectric-dielectric bilayer capacitors," *IEEE Electron Device Letters*, vol. 41, no. 10, pp. 1492–1495, 2020.

[168] W. J. Merz, "Switching time in ferroelectric $BaTiO_3$ and its dependence on crystal thickness," *Journal of Applied Physics*, vol. 27, no. 8, pp. 938–943, 1956.

[169] M. D. Glinchuk, A. N. Morozovska, A. Lukowiak, W. Strek, M. V. Silibin, D. V. Karpinsky, Y. Kim, and S. V. Kalinin, "Possible electrochemical origin of ferroelectricity in HfO_2 thin films," *Journal of Alloys and Compounds*, vol. 830, p. 153 628, 2020.

[170] X. Lyu, M. Si, X. Sun, M. A. Capano, H. Wang, and P. Ye, "Ferroelectric and anti-ferroelectric hafnium zirconium oxide: Scaling limit, switching speed and record high polarization density," in *2019 Symposium on VLSI Technology*, IEEE, 2019.

[171] M. Si, X. Lyu, and P. D. Ye, "Ferroelectric polarization switching of hafnium zirconium oxide in a ferroelectric/dielectric stack," *ACS Applied Electronic Materials*, vol. 1, no. 5, pp. 745–751, 2019.

[172] H. C. Lin, P. D. Ye, and G. D. Wilk, "Leakage current and breakdown electric-field studies on ultrathin atomic-layer-deposited Al_2O_3 on GaAs," *Applied Physics Letters*, vol. 87, no. 18, p. 182 904, 2005.

[173] M. Pešić, F. P. G. Fengler, L. Larcher, A. Padovani, T. Schenk, E. D. Grimley, X. Sang, J. M. LeBeau, S. Slesazeck, U. Schroeder, and T. Mikolajick, "Physical mechanisms behind the field-cycling behavior of HfO_2-based ferroelectric capacitors," *Advanced Functional Materials*, vol. 26, no. 25, pp. 4601–4612, 2016.

[174] H. J. Kim, M. H. Park, Y. J. Kim, Y. H. Lee, T. Moon, K. D. Kim, S. D. Hyun, and C. S. Hwang, "A study on the wake-up effect of ferroelectric $Hf_{0.5}Zr_{0.5}O_2$ films by pulse-switching measurement," *Nanoscale*, vol. 8, no. 3, pp. 1383–1389, 2016.

[175] A. Chouprik, M. Spiridonov, S. Zarubin, R. Kirtaev, V. Mikheev, Y. Lebedinskii, S. Zakharchenko, and D. Negrov, "Wake-up in a $Hf_{0.5}Zr_{0.5}O_2$ film: A cycle-by-cycle emergence of the remnant polarization via the domain depinning and the vanishing of the anomalous polarization switching," *ACS Applied Electronic Materials*, vol. 1, no. 3, pp. 275–287, 2019.

[176] Y. Goh, S. H. Cho, S.-H. K. Park, and S. Jeon, "Oxygen vacancy control as a strategy to achieve highly reliable hafnia ferroelectrics using oxide electrode," *Nanoscale*, vol. 12, no. 16, pp. 9024–9031, 2020.

[177] P. D. Lomenzo, C. Richter, T. Mikolajick, and U. Schroeder, "Depolarization as driving force in antiferroelectric hafnia and ferroelectric wake-up," *ACS Applied Electronic Materials*, vol. 2, no. 6, pp. 1583–1595, 2020.

[178] J. Zhou, G. Han, N. Xu, J. Li, Y. Peng, Y. Liu, J. Zhang, Q.-Q. Sun, D. W. Zhang, and Y. Hao, "Incomplete dipoles flipping produced near hysteresis-free negative capacitance transistors," *IEEE Electron Device Letters*, vol. 40, no. 2, pp. 329–332, 2019.

[179] J. Li, Y. Qu, M. Si, X. Lyu, and P. D. Ye, "Multi-probe characterization of ferroelectric/dielectric interface by C-V, P-V and conductance methods," in *2020 IEEE Symposium on VLSI Technology*, IEEE, 2020.

[180] K. Toprasertpong, M. Takenaka, and S. Takagi, "Direct observation of interface charge behaviors in FeFET by quasi-static split c-v and hall techniques: Revealing FeFET operation," in *2019 IEEE International Electron Devices Meeting (IEDM)*, IEEE, 2019.

[181] T. Moriya, "Anisotropic superexchange interaction and weak ferromagnetism," *Physical Review*, vol. 120, no. 1, pp. 91–98, 1960.

[182] I. Dzyaloshinsky, "A thermodynamic theory of "weak" ferromagnetism of antiferromagnetics," *Journal of Physics and Chemistry of Solids*, vol. 4, no. 4, pp. 241–255, 1958.

[183] B. Ruette, S. Zvyagin, A. P. Pyatakov, A. Bush, J. F. Li, V. I. Belotelov, A. K. Zvezdin, and D. Viehland, "Magnetic-field-induced phase transition in $BiFeO_3$ observed by high-field electron spin resonance: Cycloidal to homogeneous spin order," *Physical Review B*, vol. 69, no. 6, p. 064 114, 2004.

[184] A. K. Zvezdin and A. P. Pyatakov, "On the problem of coexistence of the weak ferromagnetism and the spin flexoelectricity in multiferroic bismuth ferrite," *EPL (Europhysics Letters)*, vol. 99, no. 5, p. 57 003, 2012.

[185] C. Ederer and N. A. Spaldin, "Weak ferromagnetism and magnetoelectric coupling in bismuth ferrite," *Physical Review B*, vol. 71, no. 6, p. 060 401, 2005.

[186] M. Trassin, J. D. Clarkson, S. R. Bowden, J. Liu, J. T. Heron, R. J. Paull, E. Arenholz, D. T. Pierce, and J. Unguris, "Interfacial coupling in multiferroic/ferromagnet heterostructures," *Physical Review B*, vol. 87, no. 13, p. 134 426, 2013.

[187] Z. Zhou, M. Trassin, Y. Gao, Y. Gao, D. Qiu, K. Ashraf, T. Nan, X. Yang, S. R. Bowden, D. T. Pierce, M. D. Stiles, J. Unguris, M. Liu, B. M. Howe, G. J. Brown, S. Salahuddin, R. Ramesh, and N. X. Sun, "Probing electric field control of magnetism using ferromagnetic resonance," *Nature Communications*, vol. 6, no. 1, 2015.

[188] T. Zhao, A. Scholl, F. Zavaliche, K. Lee, M. Barry, A. Doran, M. P. Cruz, Y. H. Chu, C. Ederer, N. A. Spaldin, R. R. Das, D. M. Kim, S. H. Baek, C. B. Eom, and R. Ramesh, "Electrical control of antiferromagnetic domains in multiferroic $BiFeO_3$ films at room temperature," *Nature Materials*, vol. 5, no. 10, pp. 823–829, 2006.

[189] J. X. Zhang, Y. L. Li, S. Choudhury, L. Q. Chen, Y. H. Chu, F. Zavaliche, M. P. Cruz, R. Ramesh, and Q. X. Jia, "Computer simulation of ferroelectric domain structures in epitaxial $BiFeO_3$ thin films," *Journal of Applied Physics*, vol. 103, no. 9, p. 094 111, 2008.

[190] Y. L. Li, S. Choudhury, Z. K. Liu, and L. Q. Chen, "Effect of external mechanical constraints on the phase diagram of epitaxial $PbZr_{1-x}Ti_xO_3$ thin films — thermodynamic calculations and phase-field simulations," *Applied Physics Letters*, vol. 83, no. 8, pp. 1608–1610, 2003.

[191] S. Farokhipoor and B. Noheda, "Conduction through 71° domain walls in $BiFeO_3$ thin films," *Physical Review Letters*, vol. 107, no. 12, p. 127 601, 2011.

[192] Y. Xiao, V. B. Shenoy, and K. Bhattacharya, "Depletion layers and domain walls in semiconducting ferroelectric thin films," *Physical Review Letters*, vol. 95, no. 24, p. 247 603, 2005.

[193] L. Hong, A. K. Soh, Q. G. Du, and J. Y. Li, "Interaction of o vacancies and domain structures in single crystal $BaTiO_3$: Two-dimensional ferroelectric model," *Physical Review B*, vol. 77, no. 9, p. 094 104, 2008.

[194] J. Seidel, L. W. Martin, Q. He, Q. Zhan, Y.-H. Chu, A. Rother, M. E. Hawkridge, P. Maksymovych, P. Yu, M. Gajek, N. Balke, S. V. Kalinin, S. Gemming, F. Wang, G. Catalan, J. F. Scott, N. A. Spaldin, J. Orenstein, and R. Ramesh, "Conduction at domain walls in oxide multiferroics," *Nature Materials*, vol. 8, no. 3, pp. 229–234, 2009.

[195] J. Seidel, P. Maksymovych, Y. Batra, A. Katan, S.-Y. Yang, Q. He, A. P. Baddorf, S. V. Kalinin, C.-H. Yang, J.-C. Yang, Y.-H. Chu, E. K. H. Salje, H. Wormeester, M. Salmeron, and R. Ramesh, "Domain wall conductivity in la-doped $BiFeO_3$," *Physical Review Letters*, vol. 105, no. 19, p. 197 603, 2010.

[196] T. Rojac, A. Bencan, G. Drazic, N. Sakamoto, H. Ursic, B. Jancar, G. Tavcar, M. Makarovic, J. Walker, B. Malic, and D. Damjanovic, "Domain-wall conduction in ferroelectric $BiFeO_3$ controlled by accumulation of charged defects," *Nature Materials*, vol. 16, no. 3, pp. 322–327, 2016.

[197] S. Farokhipoor and B. Noheda, "Local conductivity and the role of vacancies around twin walls of (001)-$BiFeO_3$ thin films," *Journal of Applied Physics*, vol. 112, no. 5, p. 052 003, 2012.

[198] S. Bhattacharjee, D. Rahmedov, D. Wang, J. Íñiguez, and L. Bellaiche, "Ultrafast switching of the electric polarization and magnetic chirality in $BiFeO_3$ by an electric field," *Physical Review Letters*, vol. 112, no. 14, p. 147 601, 2014.

[199] E. Parsonnet, Y.-L. Huang, T. Gosavi, A. Qualls, D. Nikonov, C.-C. Lin, I. Young, J. Bokor, L. W. Martin, and R. Ramesh, "Toward intrinsic ferroelectric switching in multiferroic $BiFeO_3$," *Physical Review Letters*, vol. 125, no. 6, p. 067 601, 2020.

[200] C.-S. Hsu, S.-C. Chang, D. E. Nikonov, I. A. Young, and A. Naeemi, "Hysteresis-free negative capacitance effect in metal-ferroelectric-insulator-metal capacitors with dielectric leakage and interfacial trapped charges," *Physical Review Applied*, vol. 15, no. 3, p. 034 048, 2021.

[201] J. Müller, T. S. Böscke, S. Müller, E. Yurchuk, P. Polakowski, J. Paul, D. Martin, T. Schenk, K. Khullar, A. Kersch, W. Weinreich, S. Riedel, K. Seidel, A. Kumar, T. M. Arruda, S. V. Kalinin, T. Schlosser, R. Boschke, R. van Bentum, U. Schröder, and T. Mikolajick, "Ferroelectric hafnium oxide: A CMOS-compatible and highly

scalable approach to future ferroelectric memories," in *2013 IEEE International Electron Devices Meeting*, IEEE, 2013.

[202] E. Yurchuk, J. Muller, R. Hoffmann, J. Paul, D. Martin, R. Boschke, T. Schlosser, S. Muller, S. Slesazeck, R. van Bentum, M. Trentzsch, U. Schroder, and T. Mikolajick, "HfO_2-based ferroelectric field-effect transistors with 260 nm channel length and long data retention," in *2012 4th IEEE International Memory Workshop*, IEEE, 2012.

[203] N. Gong and T.-P. Ma, "A study of endurance issues in HfO_2-based ferroelectric field effect transistors: Charge trapping and trap generation," *IEEE Electron Device Letters*, vol. 39, no. 1, pp. 15–18, 2018.

[204] F. Mehmood, T. Mikolajick, and U. Schroeder, "Wake-up mechanisms in ferroelectric lanthanum-doped $Hf_{0.5Z}r_{0.5}O_2$ thin films," *physica status solidi (a)*, vol. 217, no. 22, p. 2 000 281, 2020.

[205] L. Vandelli, L. Larcher, D. Veksler, A. Padovani, G. Bersuker, and K. Matthews, "A charge-trapping model for the fast component of positive bias temperature instability (PBTI) in high-κ gate-stacks," *IEEE Transactions on Electron Devices*, vol. 61, no. 7, pp. 2287–2293, 2014.

[206] Y.-C. Liao, C. Pan, and A. Naeemi, "Benchmarking and optimization of spintronic memory arrays," *IEEE Journal on Exploratory Solid-State Computational Devices and Circuits*, vol. 6, no. 1, pp. 9–17, 2020.

[207] D. E. Nikonov and I. A. Young, "Benchmarking spintronic logic devices based on magnetoelectric oxides," *Journal of Materials Research*, vol. 29, no. 18, pp. 2109–2115, 2014.

[208] S. Manipatruni, D. E. Nikonov, C.-C. Lin, T. A. Gosavi, H. Liu, B. Prasad, Y.-L. Huang, E. Bonturim, R. Ramesh, and I. A. Young, "Scalable energy-efficient magnetoelectric spin–orbit logic," *Nature*, vol. 565, no. 7737, pp. 35–42, 2018.

[209] B. Prasad, Y.-L. Huang, R. V. Chopdekar, Z. Chen, J. Steffes, S. Das, Q. Li, M. Yang, C.-C. Lin, T. Gosavi, D. E. Nikonov, Z. Q. Qiu, L. W. Martin, B. D. Huey, I. Young, J. Íñiguez, S. Manipatruni, and R. Ramesh, "Ultralow voltage manipulation of ferromagnetism," *Advanced Materials*, vol. 32, no. 28, p. 2 001 943, 2020.

[210] M. Bibes and A. Barthélémy, "Towards a magnetoelectric memory," *Nature Materials*, vol. 7, no. 6, pp. 425–426, 2008.

[211] Y.-C. Liao, C.-S. Hsu, D. E. Nikonov, H. Li, S.-C. Chang, I. A. Young, and A. Naeemi, "Evaluating the performance of the ultra-low power

magnetoelectric random-access memory with a physics-based compact model of the antiferromagnet/ferromagnet bilayer," *in preparation for publication*, 2021.

[212] S.-C. Chang, N. Haratipour, S. Shivaraman, T. L. Brown-Heft, J. Peck, C.-C. Lin, I.-C. Tung, D. R. Merrill, H. Liu, C.-Y. Lin, F. Hamzaoglu, M. V. Metz, I. A. Young, J. Kavalieros, and U. E. Avci, "Anti-ferroelectric $Hf_xZr_{1-x}O_2$ capacitors for high-density 3-d embedded-DRAM," in *2020 IEEE International Electron Devices Meeting (IEDM)*, IEEE, 2020.

[213] S. Clima, S. McMitchell, K. Florent, L. Nyns, M. Popovici, N. Ronchi, L. D. Piazza, J. V. Houdt, and G. Pourtois, "First-principles perspective on poling mechanisms and ferroelectric/antiferroelectric behavior of $Hf_{1-x}Zr_xO_2$ for FEFET applications," in *2018 IEEE International Electron Devices Meeting (IEDM)*, IEEE, 2018.

[214] M. Lundstrom and X. Sun, "Notes on the solution of the poisson-boltzmann equation for mos capacitors and mosfets, 2nd edition," `https://nanohub.org/resources/5338`, 2012.

[215] W. Shockley and W. T. Read, "Statistics of the recombinations of holes and electrons," *Physical Review*, vol. 87, no. 5, pp. 835–842, 1952.

[216] P. Hehenberger, "Dissertation: Advanced characterization of the bias temperature instability," 2011.

[217] M. Herrmann and A. Schenk, "Field and high-temperature dependence of the long term charge loss in erasable programmable read only memories: Measurements and modeling," *Journal of Applied Physics*, vol. 77, no. 9, pp. 4522–4540, 1995.

[218] L. Vandelli, A. Padovani, L. Larcher, R. G. Southwick, W. B. Knowlton, and G. Bersuker, "A physical model of the temperature dependence of the current through SiO_2/HfO_2 stacks," *IEEE Transactions on Electron Devices*, vol. 58, no. 9, pp. 2878–2887, 2011.

VITA

Chia-Sheng Hsu is currently pursuing his PhD degree in electrical and computer engineering at Professor Azad Naeemi's lab at the Georgia Institute of Technology, Georgia, USA. He obtained an undergraduate degree in electrical engineering from National Tsing Hua University, Hsinchu, Taiwan. Then he completed his compulsory military service in a national forest park. After that, he joined a lab at the Institute of Physics in *Academia Sinica*, Taipei, Taiwan, and helped the principal investigator set up a home-built scanning tunneling microscope (STM), an ultra-high vacuum ultra-low temperature experimental system. This tool was able to study the surface properties of materials at a nanoscale.

In 2014, he started his PhD program at Georgia Tech with the technical interest in nanodevice physical mechanisms and design simulation. His current research focuses on the potential applications of ferroelectric (FE) materials in electronic devices in the nanoscale regime. For example, one of the most attracting characteristics of FE is the appearance of *negative capacitance effects* during FE switching. In his work highlighted on the cover of *IEEE Electron Device Letters*, he implemented a SPICE model of ferroelectric capacitors, which could be used to analyze the performances of *negative capacitance field-effect transistors* (NCFETs) at the device and circuit levels. The major contribution of this work lies in exploring the possibility of using NCFETs to achieve ultra-low power devices as the pursuit of Moore's law comes to a bottleneck. He currently works on the understanding of the fundamental switching mechanisms of FEs with multi-domain phase-field modeling. This multi-domain approach is believed to capture the inhomogeneous nature of FE thin films.